

# **Empirical Modeling of Fuel Cell Durability: Cathode Catalyst Layer Degradation**

**by**  
**Marvin Messing**

B.Eng., University of Victoria, 2015

Thesis Submitted in Partial Fulfillment of the  
Requirements for the Degree of  
Master of Applied Science

in the  
School of Mechatronic Systems Engineering  
Faculty of Applied Sciences

© Marvin Messing 2017  
SIMON FRASER UNIVERSITY  
Fall 2017

Copyright in this work rests with the author. Please ensure that any reproduction or re-use is done in accordance with the relevant national copyright legislation.

# Approval

**Name:** **Marvin Messing**

**Degree:** **Master of Applied Science**

**Title:** **Empirical Modeling of Fuel Cell Durability:  
Cathode Catalyst Layer Degradation**

**Examining Committee:** **Chair: Mohammad Narimani**  
Lecturer

**Erik Kjeang**  
Senior Supervisor  
Associate Professor

**Jiacheng (Jason) Wang**  
Supervisor  
Assistant Professor

**Gary Wang**  
Internal Examiner  
Professor

**Date Defended/Approved:** December 6<sup>th</sup>, 2017

## **Abstract**

Fuel cells for automotive applications do not yet match the durability and cost of conventional engines. Durability can be improved by better understanding degradation mechanisms of fuel cell components. A critical component is the cathode electrode, which facilitates the slow oxygen reduction reaction. In this work, fuel cells with state of the art electrodes are manufactured and subjected to degradation tests simulating two drive cycle conditions: load cycling, and start-up/shutdown cycling. The degradation data is used to empirically model the voltage loss due to cathode electrode degradation, to predict voltage loss throughout fuel cell lifetime, and compare to findings in literature. The model may be used as a starting point to better understand electrode degradation, and to develop fundamental models. Based on degradation results it is recommended to investigate coupling effects between the different drive cycle conditions, impact of mitigation factors, and effect of different catalyst loadings on the electrode durability.

**Keywords:** fuel cell; PEM, cathode electrode; degradation; drive cycles; empirical model

*To my parents, and my lifelong pursuit to make  
the most of the privileges they have given me.*

## **Acknowledgements**

First, I would like to thank my supervisor Dr. Erik Kjeang for giving me this opportunity, for all his advice, and for his support during my work.

My thanks also to Dr. Jason Wang, and Dr. Gary Wang for agreeing to be my committee members.

I would also like to thank my FCREL colleagues and friends Paran Serma, Dr. Alireza Alavijeh, Omar Ibrahim, Frank Orfino, Dr. Sebastian Eberhardt, Dr. Michael Whitwick and Dr. Mohamed El Hannach for all their help with my work. In addition, I would like to thank Ben Britton for sharing his expertise, and Dr. Caue Martins for many insightful conversations.

I would like to thank coop students Kevin Dahl, Alex Boswell, and Vivian Pan for helping me at all stages of my experimental work.

Thanks also to my friends and family for all their support, and Erin for always keeping me sane.

Funding for this research was provided by the Community Trust Endowment Fund (CTEF) at Simon Fraser University, the Canada Foundation for Innovation (CFI), the British Columbia Knowledge Development Fund, the Natural Sciences and Engineering Research Council of Canada (NSERC), and Western Economic Diversification (WD). I would also like to thank 4D LABS at Simon Fraser University, Burnaby, BC Canada for providing expertise with sonic spray coating.

# Table of Contents

Approval.....	ii
Abstract.....	iii
Dedication.....	iv
Acknowledgements.....	v
Table of Contents.....	vi
List of Tables.....	viii
List of Figures.....	ix
List of Acronyms.....	xi
<b>Chapter 1. Introduction.....</b>	<b>1</b>
1.1. History of Fuel Cells.....	1
1.1.1. Commercialization Challenges.....	2
1.2. Proton Exchange Membrane Fuel Cells.....	4
1.2.1. Electrochemical Theory.....	5
1.2.2. Components and Materials.....	5
Membrane.....	6
Catalyst Layer.....	6
Gas Diffusion Media.....	7
Flow Field Plates.....	8
1.3. Fuel Cell Durability.....	8
1.3.1. Cathode Electrode Degradation.....	9
Cause of Degradation and Mitigation.....	11
Degradation Testing.....	13
1.3.2. Fuel Cell Lifetime Modeling.....	14
1.4. Objectives.....	15
<b>Chapter 2. Fuel Cell Fabrication.....</b>	<b>17</b>
2.1. Catalyst Layer Fabrication.....	18
2.1.1. Catalyst Ink.....	20
2.2. Membrane Electrode Assembly.....	21
<b>Chapter 3. Experimental Methods.....</b>	<b>23</b>
3.1. Test Stand and Fuel Cell Hardware.....	23
3.2. In-Situ Diagnostics.....	25
3.2.1. Polarization Curves.....	25
3.2.2. Cyclic Voltammetry.....	26
3.2.3. Electrochemical Impedance Spectroscopy.....	30
3.3. Degradation Testing.....	32
3.3.1. Load Cycling.....	32
3.3.2. Start-up/Shut-down Cycling.....	33
3.4. Conditioning and Recovery.....	35
3.4.1. Conditioning.....	35

3.4.2. Recovery .....	36
3.5. Automation .....	37
3.5.1. System Controller Software .....	40
<b>Chapter 4. Empirical Modeling Methods.....</b>	<b>42</b>
4.1. Polynomial Models .....	42
4.2. Fuel Cell Vehicle Model .....	43
4.3. Drive Cycles .....	46
<b>Chapter 5. Results and Discussion.....</b>	<b>52</b>
5.1. Baseline .....	52
5.2. Degradation.....	55
5.2.1. Load Cycles.....	56
5.2.2. Start-Up Shutdown Cycles.....	62
5.3. Empirical Degradation Model.....	65
5.4. Lifetime Prediction .....	68
<b>Chapter 6. Conclusion .....</b>	<b>71</b>
6.1. Future Work.....	73
6.1.1. Model Improvements .....	73
6.1.2. Model Use Case .....	74
<b>References.....</b>	<b>75</b>
<b>Appendix A. Datasets .....</b>	<b>80</b>
<b>Appendix B. Automation.....</b>	<b>81</b>
<b>Appendix C. Non-parametric Model &amp; Scale Factor .....</b>	<b>83</b>
Non-parametric Model.....	83
Scale Factor .....	84
Model Comparison .....	85

## List of Tables

Table 1: Details of materials used in fuel cell fabrication .....	18
Table 2: Details of fuel cell hardware components .....	18
Table 3: Sono-Tek Exactacoat Setting for Pt/C ink CCM .....	19
Table 4: General fuel cell operating conditions .....	24
Table 5: Diagnostic fuel cell operating conditions .....	25
Table 6: Recovery Protocol .....	36
Table 7: Vehicle Model Parameters [36], [29] .....	48
Table 8: Fuel Cell Stack Configuration [36], [6] .....	48
Table 9: Drive cycle details with high, medium, and low cycle variations .....	50
Table 10: Fuel Cell Specimens Summary .....	52
Table 11: Electrochemical Measurements .....	55
Table 12: DOE Degradation Targets .....	56
Table 13: Modeled Cathode Electrode Specification .....	65
Table 14: Description of symbols used in degradation model .....	84
Table 15: Model accuracy .....	85

## List of Figures

Figure 1: Hydrogen delivery 2020 targets vs. 2015 status [7] .....	3
Figure 2: Fuel cell 2020 targets vs. 2015 status [6] .....	3
Figure 3: Schematic of a PEMFC .....	4
Figure 4: Nafion™ chemical structure .....	6
Figure 5: Catalyst Layer Schematic.....	7
Figure 6: Cathode electrode degradation mechanisms.....	10
Figure 7: US Highway Dynamometer Driving Schedule.....	11
Figure 8: US Urban Dynamometer Driving Schedule.....	11
Figure 9: Start-up/shut-down degradation .....	12
Figure 10: Membrane Electrode Assembly .....	17
Figure 11: MEA Components and Compression.....	21
Figure 12: Membrane Electrode Assembly .....	22
Figure 13: Fuel Cell Hardware.....	23
Figure 14: Polarization Curve .....	26
Figure 15: Cyclic Voltammogram.....	27
Figure 16: ECSA integration boundaries .....	28
Figure 17: Double layer capacitance current and crossover current approximation .....	29
Figure 18: Nyquist Plot .....	30
Figure 19: Voltage data from load cycle protocol implementation .....	32
Figure 20: Start-up/shut-down test setup schematic.....	33
Figure 21: Voltage data from start/stop protocol implementation .....	34
Figure 22: Test System Diagram.....	38
Figure 23: Custom control software GUI.....	39
Figure 24: Custom valve control circuit.....	40
Figure 25: Empirical Fuel Cell Model Voltage and Power Data.....	46
Figure 26: Conversion Methodology.....	47
Figure 27: US Urban Drive Cycle Converted to Power and Voltage .....	48
Figure 28: Counting Load Cycles in US Highway Drive Cycle .....	49
Figure 29: Counting Load Cycles in US Urban Drive Cycle .....	49
Figure 30: Sensitivity of different model configurations .....	51
Figure 31: Baseline BOL Polarizations with Variance .....	53
Figure 32: Baseline BOL Cyclic Voltammograms .....	54
Figure 33: Baseline BOL Nyquist Plots.....	55
Figure 34: Performance at 0.8 A/cm <sup>2</sup> loss for different LPLs.....	57
Figure 35: Performance at 0.6 A/cm <sup>2</sup> loss for different LPLs (Adjusted) .....	57
Figure 36: ECSA loss for different LPLs .....	58
Figure 37: Cell performance degradation .....	59

Figure 38: ECSA Loss.....	60
Figure 39: Double Layer Capacitance and Cross-Over Current Change .....	61
Figure 40: Cell Resistance Change .....	61
Figure 41: Performance degradation during SU/SD cycling.....	63
Figure 42: ECSA loss during SU/SD cycling.....	63
Figure 43: Crossover-current and double layer capacitance change .....	64
Figure 44: Resistance change.....	65
Figure 45: Model predictions compared to literature predictions.....	68
Figure 46: Preliminary data for combined degradation .....	70
Figure 47: Model fit comparison .....	86
Figure 48: Model prediction comparison.....	87

## List of Acronyms

AST	Accelerated Stress Test
BOL	Beginning of Life
CCM	Catalyst Coated Membrane
CL	Catalyst Layer
CV	Cyclic Voltammetry
DOE	See US DOE
ECSA	Electrochemically Active Surface Area
EIS	Electrochemical Impedance Spectroscopy
EOL	End of Life
FCReL	Fuel Cell Research Lab
GDE	Gas Diffusion Electrode
GDL	Gas Diffusion Layer
GDM	Gas Diffusion Medium
GHG	Greenhouse Gas
HOR	Hydrogen Oxidation Reaction
LCA	Life Cycle Assessment
LPL	Lower Potential Limit
MEA	Membrane Electrode Assembly
MPL	Micro Porous Layer
NREL	See US NREL
OCV	Open Circuit Voltage
ORR	Oxygen Reduction Reaction
PEMFC	Proton Exchange Membrane Fuel Cell
Pt/C	Platinum on Carbon
SHE	Standard Hydrogen Electrode
US DOE	United States Department of Energy
US NREL	United States National Renewable Energy Laboratory
UPL	Upper Potential Limit
WHO	World Health Organization

# Chapter 1. Introduction

*We must recognize, in our day-to-day lives and in our governing institutions, that Earth with all its life is our only home.*

*(Ripple WJ et al. & 16000 Scientists)*

This year 2017 we have been warned, for the second time, now by more than 16000 scientists around the world, who evaluated humanities progress in saving planet earth since the first warning in 1992 [1]. With few exceptions, the threats to our biosphere have not improved, and even increased in some cases after 25 years. Among issues like overpopulation, and the loss of bio-diversity, the destructive impact of greenhouse gas (GHG) emissions are highlighted. One source of GHG mentioned is the burning of fossil fuels. Similarly, a 2017 global study on pollution and health [2] found that pollution is responsible for more deaths than any other cause. Among pollution from soils, water, and air, air pollution makes up the largest percentage of the total deaths in countries of all levels of income. As other organizations, including the World Health Organization (WHO), have done before, this study again recommends government action to eliminate tax breaks for industries which cause pollution, and to force them to carry some of the healthcare costs. One such industry is most of the automotive industry, with its dependence on diesel and gasoline fuels still strong. Alternative technologies, such as batteries and fuel cells, exist, but more work is needed on several fronts to convince the automotive industry to abandon fossil fuels. The work presented in this thesis is a contribution to improving the fuel cell technology front, by providing at starting point for the modeling of a fuel cell component, the cathode electrode, in the form of an empirical degradation model.

## 1.1. History of Fuel Cells

Fuel cells date back to 1839 when Sir William Grove first demonstrated the fuel cell reaction. Between 1899 and the 1950s fundamental discoveries for different types of fuel cells were made by Walther Nernst and Sir Francis Bacon, but without practical applications. During the 1950s fuel cells became part of the space race between the Soviet Union and the US, where in 1955 at General Electric, the low-temperature fuel cell was invented by William Grubb. The next push for fuel cells came due to rising energy costs in

the 1980s, and in 1991 United Technologies Company made the first commercially successful fuel cell device: fuel cell power generators. Breakthroughs in fuel cell manufacturing techniques and the discovery of Nafion™ gave rise to the modern proton exchange membrane fuel cell (PEMFC) [3]. By the mid to late 2000s, many of the major automotive companies started some form of research and development on PEMFCs for automotive applications. Fuel cells have also been explored for many other applications from powering small, portable electronics (0 to 100 W) at room temperature (direct methanol fuel cells, micro fluidic fuel cells), to providing hundreds of kilowatts of backup power at 700 °C (molten carbonate fuel cells, solid oxide fuel cells). Today, the two major applications for PEMFCs are in stationary power generation and in the automotive industry. The automotive fuel cell sector can be divided into light duty and heavy-duty vehicles. PEMFCs have achieved early forms of commercialization for both heavy and light duty vehicles in some countries, mostly in Asia [4], with the Hyundai Tuscan, the Toyota Mirai, the Honda Clarity, and fuel cell busses [5].

### **1.1.1. Commercialization Challenges**

PEMFCs have been used in different applications for many years. While commercialization was successful for stationary power generation applications, it has not yet happened for PEMFCs in automotive applications. The reasons behind this long and slow path to success are somewhat complex. The United States Department of Energy (US DOE) frequently outputs detailed documents on the status, methods and targets of fuel cells, and related technologies. Two such documents of interest are on fuel cells [6], and on hydrogen delivery [7]. Figure 1 illustrates the 2015 status of hydrogen delivery and Figure 2 that of PEMFCs against their 2020 targets. The status of hydrogen delivery is far away from its targets, while the PEMFCs status has nearly reached all targets. Since PEMFCs require a functioning hydrogen infrastructure, lack of this infrastructure may be the most dominant barrier to the commercialization of fuel cells.

Nevertheless, PEMFC technology still lacks in two key areas: cost and durability. The cost of PEMFC stacks is mostly due to platinum based catalysts, the membrane, and cell hardware such as bi-polar plates [6]. Additional costs stem from complex manufacturing methods. The durability of PEMFCs is reduced by the degradation of fuel cell components, most importantly the membrane and the cathode electrode. PEMFC durability is discussed in more detail in the next section.

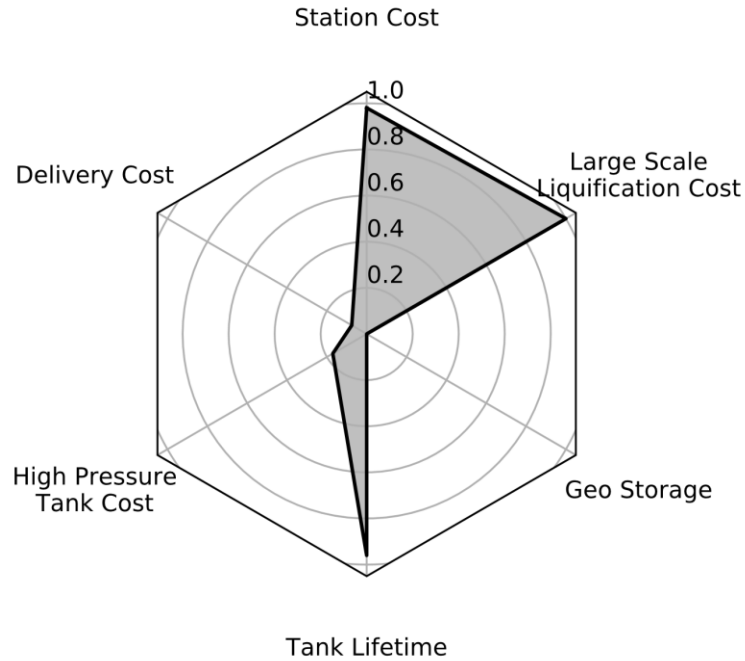


**Figure 1: Hydrogen delivery 2020 targets vs. 2015 status [7]**

The shaded area shows how close the status is to the targets, where no shading indicates zero progress towards the target, and full shading that the target has been met 100%.

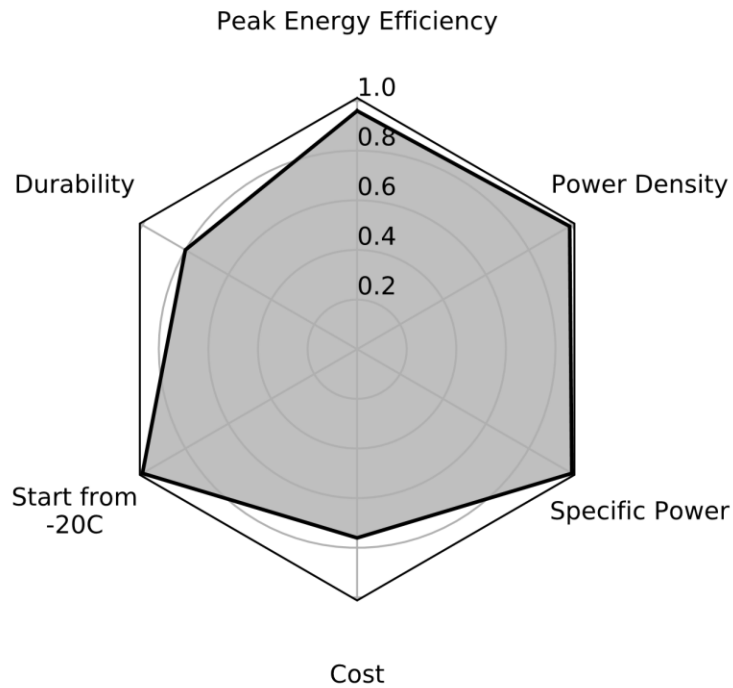


**Figure 2: Fuel cell 2020 targets vs. 2015 status [6]**

The shaded area shows how close the status is to the targets, where no shading indicates zero progress towards the target, and full shading that the target has been met 100%.

## 1.2. Proton Exchange Membrane Fuel Cells

While there are many different types of fuel cells, the Hydrogen PEMFC remains as the most suitable type of fuel cell for automotive applications. In a PEMFC, hydrogen and oxygen are consumed to produce heat, water, and electricity. Figure 3 shows a basic schematic of a PEMFC. On the anode, the hydrogen is split into protons ( $H^+$ ) and electrons ( $e^-$ ), and on the cathode, electrons and protons are combined with oxygen to form water. The proton exchange membrane (PEM) is used to separate the two reactions only allowing protons to conduct, but not electrons, which results in a difference in potential. The gas diffusion media (GDM, GDL + MPL) are added to facilitate gas, water, and electron transport, and the catalyst layers (CL) are used to accelerate the chemical reactions. To achieve voltage output from a fuel cell is relatively straight forward by simply arranging suitable materials according to Figure 3. However, to obtain optimal efficiency, stable output, and long lifetime, each component of the fuel cell must be carefully engineered and assembled.

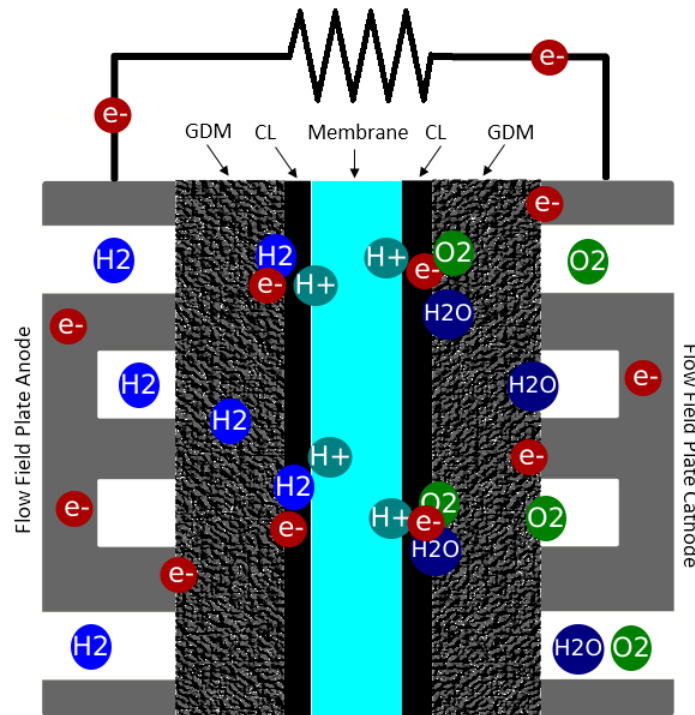


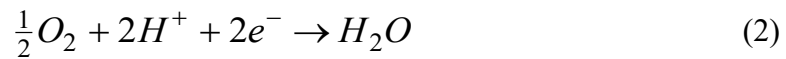
**Figure 3: Schematic of a PEMFC**

Hydrogen molecules ( $H_2$ ) enter on the anode flow field channels and move through GDM into the catalyst layer, where they split into hydrogen protons ( $H^+$ ) and electrons ( $e^-$ ). The  $H^+$  moves through the membrane into the cathode catalyst layer where it combines with oxygen ( $O_2$ ) and electrons to form water ( $H_2O$ ). The electrons move from the anode through a load, to the cathode, creating electricity.

Section 1.2.1 provides a background on the main chemical reactions taking place inside a fuel cell, and section 1.2.2 discusses some of the engineering challenges of the different fuel cell components.

### 1.2.1. Electrochemical Theory

To understand some of the challenges associated with fuel cell operation, a basic knowledge of the underlying chemical reactions is required. The reaction on the anode is a hydrogen oxidation reaction (HOR) shown in Equation 1. The reaction on the cathode is an oxygen reduction reaction (ORR) shown in Equation 2. Combining the HOR and ORR yields the overall fuel cell reaction shown in Equation 3.



Due to the relatively low operating temperature of around 80°C, both HOR and ORR natural reaction rates are much too slow to be useful, so the catalyst accelerates the reactions to usable levels. The ORR reaction is the slower of the two, so more catalyst is usually required on the cathode electrode.

The HOR is defined as the standard reference electrode, or standard hydrogen electrode (SHE), with a reduction potential of 0.00 V. The ORR has a reduction potential of +1.23 V. Therefore, the theoretical potential of a hydrogen PEMFC is +1.23 V. In practice, however, various overpotentials reduce this theoretical voltage to be around 1 V. These over potentials occur due to resistance to electron or proton transport, chemical reactions, gas and/or electron crossover through the membrane, and impurities or contamination [3].

### 1.2.2. Components and Materials

A state of the art fuel cell is made up of four main components: the membrane, the catalyst layers, the gas diffusion media, and the flow field plates. This section introduces each of those components.

## Membrane

The central component of a PEMFC is the PEM or electrolyte. Since its discovery, Nafion™ has been the standard for PEMs, its chemical structure is shown in Figure 3. The fluoropolymer backbone gives Nafion™ excellent chemical stability similar to Teflon. The sulfonic acid terminated side chains cause water to be adsorbed, and facilitate proton transport. The more water that is in the membrane, the better its proton conductivity. This is because water molecules weaken the bonds between the hydrogen proton (H<sup>+</sup>) and the sulfonic acid group, allowing hydrogen protons to move through the membrane along the side chains [3].

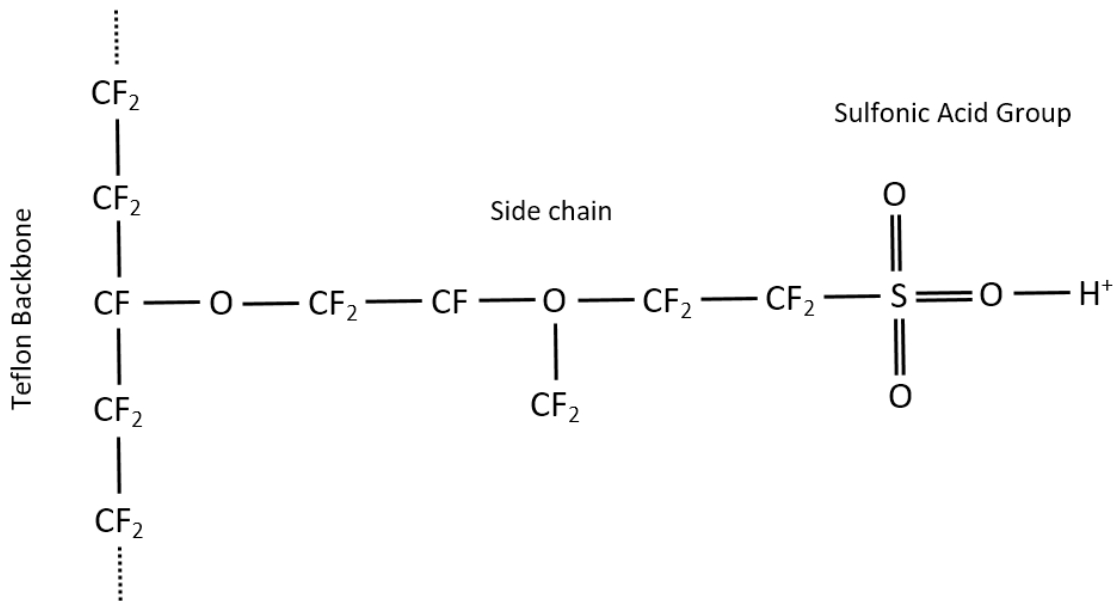
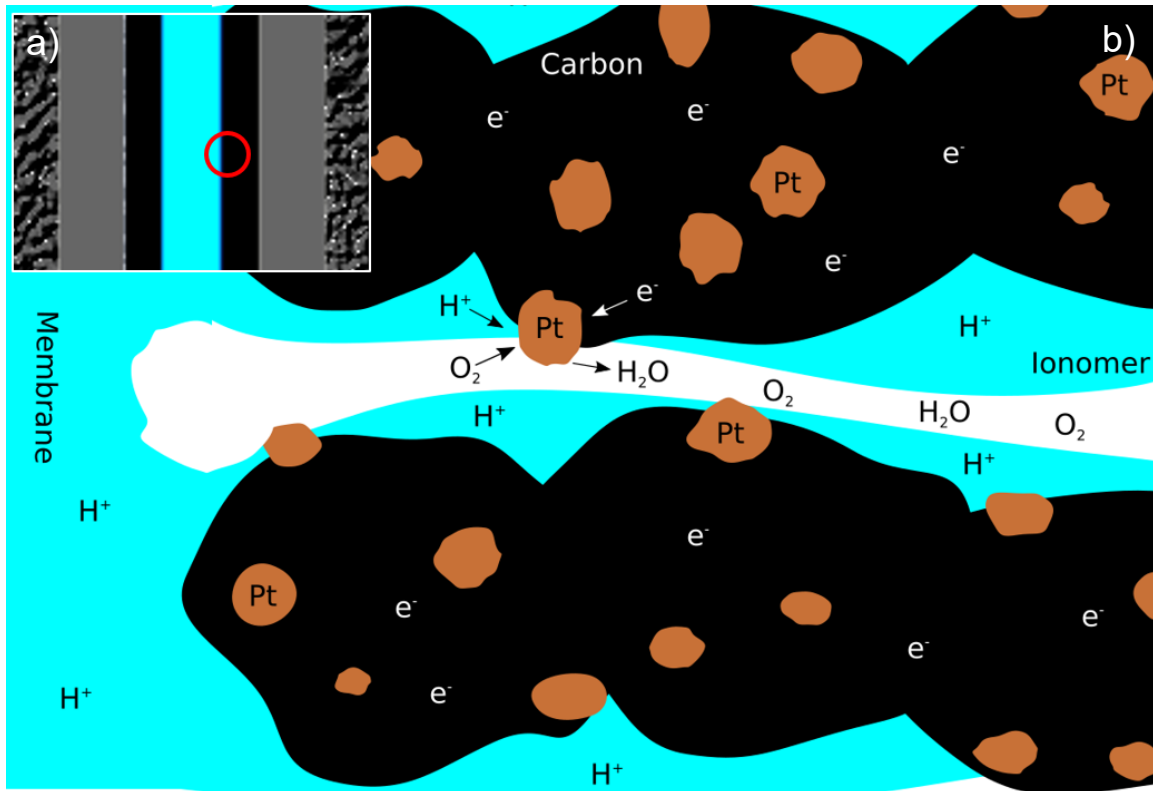


Figure 4: Nafion™ chemical structure

## Catalyst Layer

Catalyst layers are located on either side of the membrane. The most widely used type of catalyst is still platinum on carbon (Pt/C) [8]. The platinum particles are used as a catalyst to accelerate the electrochemical reactions on the anode and cathode of the fuel cell. Figure 5 b) shows a detailed schematic of the arrangements of the catalyst layer components, as well as a macro level view (a) of where the detailed view is located in the overall fuel cell. The carbon particles support the platinum, but also facilitate electron transport to and from the platinum catalyst reaction sites. The porous structure of the catalyst layers allows reactant gases to access the reaction sites, as well as water to leave

the reaction sites. Finally, ionomer is required to create a pathway for hydrogen protons from the membrane to the reaction sites [3].



**Figure 5: Catalyst Layer Schematic**

a) – macro level view of fuel cell membrane electrode assembly, b) – detailed view of catalyst layer

### ***Gas Diffusion Media***

The catalyst layers are connected to micro porous layers and gas diffusion layers. These two layers make up the gas diffusion medium of modern fuel cells. The gas diffusion layer is a paper or cloth engineered to facilitate electron transport, water transport, as well as reactant transport. It is made up of electrically conductive carbon fibers arranged in a macro-porous structure to allow reactant gases to flow through it. A Teflon coating causes the pores to be hydrophobic, allowing for increased water transport. The GDL also serves as a substrate for the MPL. The MPL is composed of carbon nanoparticles and Teflon particles to create a hydrophobic micro porous structure.

## ***Flow Field Plates***

Flow field plates are used to deliver the fuel cell reactants and remove exhaust gases (unused reactants) and water. In addition, the plates serve as a path for electrons to move from the carbon fibers of the gas diffusion media to the current collectors on the other side of the flow fields.

The automotive fuel cell industry is focusing on using metal as a material for flow field plates. While carbon plates have advantages in conductivity and resistance to corrosion, metal plates are cheaper to manufacture and significantly reduce the weight of fuel cell stacks.

There are many different designs for flow field patterns from simple parallel flow channels to nature inspired, tree root like patterns. However, simpler designs are easier to manufacture, and therefore preferred by industry [9], [6].

## **1.3. Fuel Cell Durability**

The US DOE names the membrane deterioration, loss of catalytic surface area, and carbon support corrosion as key contributors to fuel cell degradation [6], i.e. causes for reduced fuel cell durability. The first item on this list, the membrane, degrades due to chemical and mechanical stresses. Mechanical stresses such as swelling and shrinking of the membrane are caused by changes in humidity. Chemical degradation is due to impurities in the fuel and oxidant, and the formation of hydrogen peroxide ( $H_2O_2$ ). The by-products of  $H_2O_2$  are radicals such as hydroxyl (OH) and hydroperoxyl (OOH), which attack the chemical structure of the membrane [3], [10].

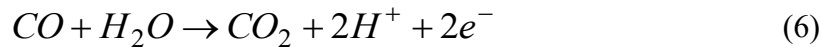
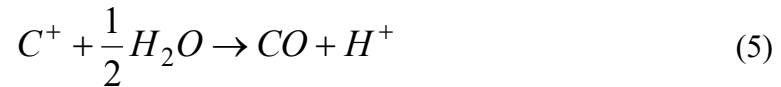
The other two items on the list of key degradation contributors are both part of the fuel cell electrodes. The anode and cathode electrodes in a fuel cell are comprised of similar components and materials. However, since the ORR, which occurs on the cathode, is much slower than the HOR, the cathode electrode is usually given more importance. The cathode electrode degradation can account for 30-40% of fuel cell degradation [11], and is therefore subject to much attention, and discussed in further detail in the following section.

### 1.3.1. Cathode Electrode Degradation

The cathode electrode degrades due to a complex interplay of many different degradation mechanisms. These degradation mechanisms can be grouped into catalyst degradation, ionomer degradation and carbon support degradation.

The ionomer is damaged by contaminants, such as OH radicals, and hydrogen peroxide, which are formed during fuel cell operation [12].

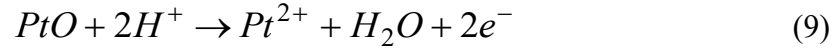
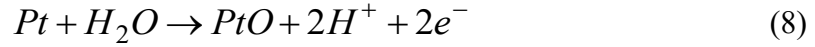
The carbon support degrades due to oxidation (or corrosion) of the carbon, which leads to damage to the carbon support structure, and its eventual collapse. The pathways of carbon corrosion are shown in Equations 4, 5 (CO formation), and 6 (CO<sub>2</sub> formation) [12], [13].



The most severe carbon corrosion is a result of large voltages across the fuel cell. These can be voltages near OCV (~0.98 V), or higher.

Catalyst degradation can be a result of Pt particle agglomeration or growth, Pt particle dissolution (loss or re-distribution), or poisoning due to contaminants. The degradation of the carbon support can cause/contribute to catalyst layer degradation as well, i.e. if the support collapses or thins out, the platinum particles it is supporting will be forced to re-distribute. Agglomeration and growth occur due to the natural tendency of nano-particles to lower their surface energy. Larger particles result in lower surface area and, therefore, lower surface energy. Beyond this natural tendency, Pt particle growth may also occur at a faster rate during fuel cell operation, as smaller particles detach from the carbon support but re-deposit to larger, adjacent Pt particles. Pt particle dissolution occurs directly as shown in Equation 7, or through the formation of platinum oxides shown in Equations 8 and 9 [3], [12], [13].





Contaminants may either originate from fuel and oxidant streams or from other components, such as seals or flow field plates, inside the fuel cell. Gas contaminants include carbon monoxide (CO), carbon dioxide (CO<sub>2</sub>), nitrogen oxides (NO, NO<sub>2</sub>), Ozone (O<sub>3</sub>), and sulfur oxides (SO<sub>2</sub>, SO<sub>3</sub>). Contaminants from fuel cell components include metallic ions and/or silicon [12], [14].

Figure 6 summarizes the most important (in the context of this work) degradation mechanisms: Pt dissolution (a), Pt agglomeration (b), ionomer chemical degradation (c), and carbon support corrosion (d). Contamination effects are insignificant in this study due to the contaminant-free materials, fuel, and oxidant used. The relevant degradation mechanisms occur under different operating conditions, which are discussed in the next section.

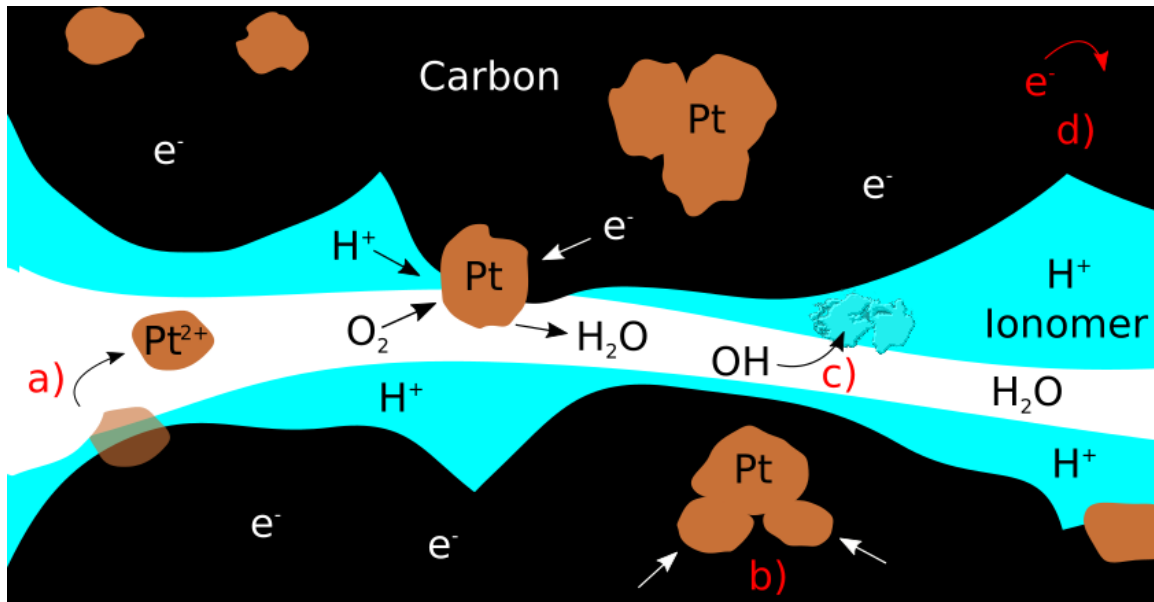


**Figure 6: Cathode electrode degradation mechanisms**

a) Pt dissolution: a Pt particle leaves its carbon support and becomes re-deposited in the ionomer, or membrane, migrates to the anode, or gets washed out through the pore, b) Pt agglomeration: Pt particles join to become a bigger particle with lower surface area/energy, c) ionomer degradation: an OH radical attacks the ionomer structure, and d) Carbon support degradation: an electron is freed from the carbon support, degrading its structure.

## ***Cause of Degradation and Mitigation***

As a vehicle is operated it is subjected to many different driving conditions, which re-occur at different frequencies throughout the vehicles lifetime. To understand and simulate these driving conditions, studies were conducted where vehicle operation was monitored. From the data collected in these studies, collections of driving conditions can be summarized into drive cycles, which are characteristic of a region, and vehicle usage purpose. For example, the US highway drive cycle, consist of characteristic vehicle speeds over time for US highway driving (Figure 7). Similarly, the US urban drive cycle consist of characteristic vehicle speeds over time for US cities (Figure 8).

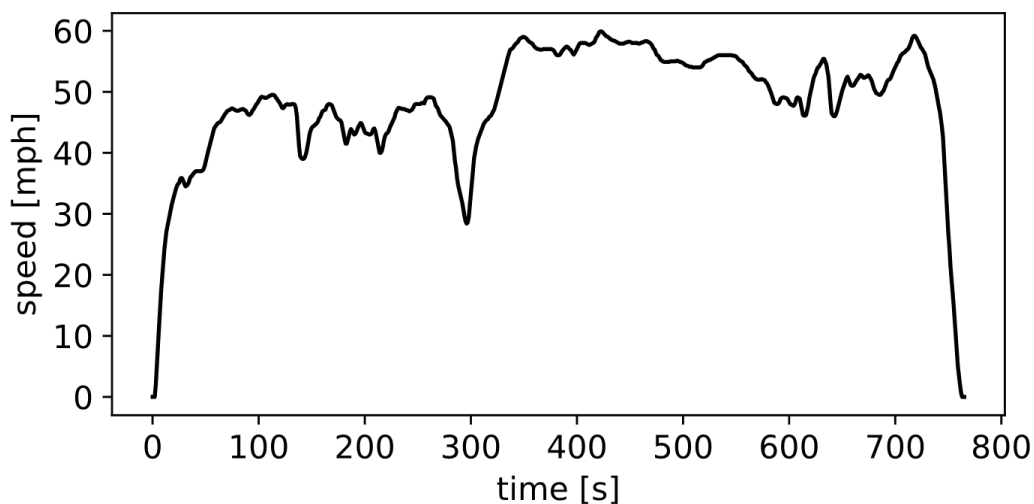


**Figure 7: US Highway Dynamometer Driving Schedule**

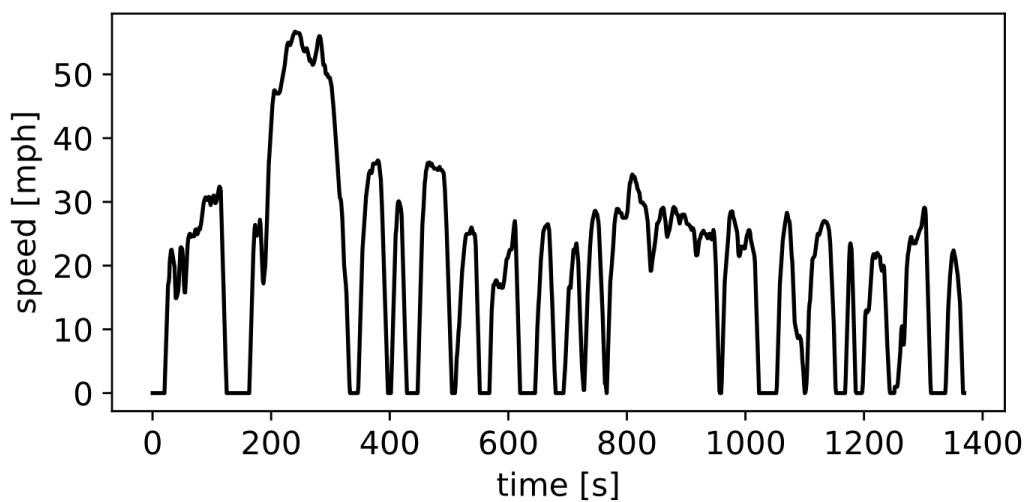


**Figure 8: US Urban Dynamometer Driving Schedule**

Different parts of these drive cycles have different effects on fuel cell degradation. The most basic drive cycles can be separated into two events: start-up/shutdown and load cycles. Start-up/shutdown occurs at the start of a trip and at the end of a trip, respectively. At the end of a trip normal fuel cell operation is stopped. At this point, air remains inside the cathode compartment, and hydrogen is trapped by seals and valves inside the anode compartment. However, hydrogen, as the smallest molecule, tends to escape its containers, and will therefore, eventually, be replaced by air. At some point, there will thus be both air and hydrogen in the anode channels, while air is also in the cathode channels. In this case, one half of the fuel cell remains at the normal OCV potential of around 1 V. The electrons freed from the hydrogen on the anode by the regular fuel cell reaction are consumed, instead of by the cathode, by the air inside the other half of the anode. This leaves the cathode starved of electrons, but having to balance the potential. It does this by freeing electrons from the carbon support, thereby degrading it. In addition, this type of condition can cause cell voltages of up to 1.5 V, which accelerate both carbon corrosion, and platinum dissolution. The reverse happens at the start of a trip. All the hydrogen has left the anode, leaving air on both sides of the fuel cell. As the hydrogen front moves in during fuel cell start-up, it again causes a condition where both hydrogen and air are on the anode at the same time, causing the cathode to degrade in the same way as during shut-down [15]. Figure 9 illustrates the start-up/shut-down degradation process.

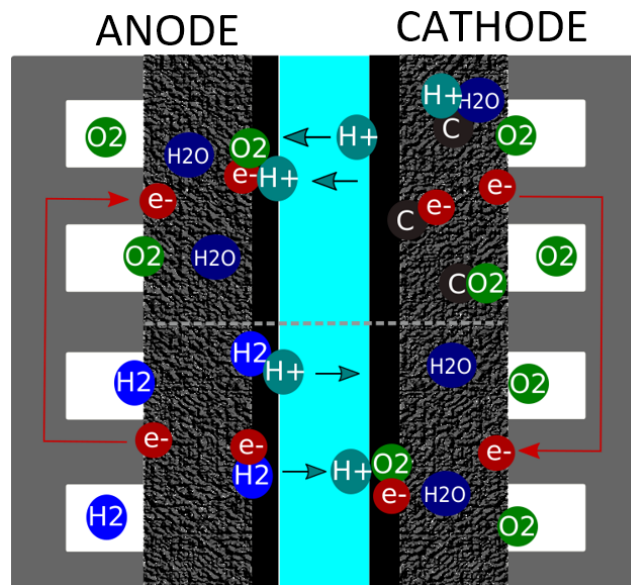


**Figure 9: Start-up/shut-down degradation**

During start-up or shut-down events, electrons (e<sup>-</sup>) freed on the anode are consumed instead of moving from anode to cathode. The cathode obtains e<sup>-</sup> via carbon (C) corrosion to balance potentials.

Degradation due to start-up/shut-down cycles can be mitigated by high-flowrate air on shutdown, and better seals to keep the hydrogen inside the channels longer. Since the degrading, chemical reactions are accelerated at higher temperatures, better seals may keep the hydrogen inside the channels at least until the fuel cell has cooled down, therefore reducing degradation.

Load cycles, on the other hand, are a result of acceleration and deceleration during vehicle operation. The fuel cell engine remains active, and the load demand changes depending on traffic conditions. Degradation due to load cycles is less severe than due to start-up/shut-down cycles, but occur much more frequently and can account for 66.6% of overall fuel cell degradation (with 33% due to start-up/shut-down cycles) [16]. During load cycling, it is mostly the platinum nano-particles which degrade, due to dissolution and increasing particle size [17].

### ***Degradation Testing***

Fuel cell degradation testing is often carried out using small scale (5 to 50cm<sup>2</sup>) laboratory setups, to evaluate fuel cell materials, understand and characterize degradation mechanisms, or to evaluate fuel cell durability. In many cases, accelerated stress tests (ASTs) are used to obtain results more rapidly, and by using less resources, such as fuel and operator time [18]. Such ASTs are also used to simulate load cycles and start-up/shut-down cycles. Takei et al. [17], for example, employed a combination of square wave voltage cycles, triangle voltage sweeps, and OCV idle as an AST for simulating different parts of load cycles, in order to understand the effect on electrode degradation of each part. Suk Joo et al. [19] used different square wave voltage cycles to accelerate start-up/shut-down degradation.

ASTs work well for the screening of materials or for generating highly degraded materials for analysis. However, if the objective is to evaluate durability of fuel cell components in the context of field conditions, there must be a strategy for relating accelerated conditions to use level conditions. This can often be done by testing different acceleration levels, and extrapolating the results to use-level conditions [20]. Alternatively, established protocols can be used together with adjusted degradation targets. Major government research organizations such as the US DOE [6], or the European Commission [21], publish guidelines for degradation testing for automotive fuel cells. These guidelines are based on their own in-house experiments, and/or published results from external

laboratories, and provide standardized experimental methods and targets for the assessment of fuel cell durability (and other aspects of fuel cell technologies).

### **1.3.2. Fuel Cell Lifetime Modeling**

The ability to accurately model the durability of fuel cell components and predict overall fuel cell lifetime is crucial not only for the development of better fuel cells, but also for predicting the future use and performance of fuel cell technology in the light of changes in the energy and transportation sectors. Therefore, durability models are needed for each component of the fuel cell. A fundamental model is the most desired type of model for a given fuel cell component, as it is built on a deep understanding of degradation mechanisms and the electrochemical, thermodynamic, and transport phenomena inside a fuel cell. However, since the exact details of many degradation mechanisms under different operating conditions for different components are not completely understood, approximations must be made. Empirical models, on the other hand, are derived from experimental data, and therefore reflect the performance of a given fuel cell under given conditions. However, if the conditions or the fuel cell materials change, new data is required. Furthermore, the exact cause of changes in performance is often not clear. Therefore, fuel cell component durability models may start as empirical models, and are slowly converted to fundamental models, as a deeper understanding of degradation mechanisms is gained. The experimental data can be used to validate fundamental portions of the model along the way [22].

Many fundamental [23], empirical, and even machine-learning orientated models exist [24]. Empirical models are most relevant to the subject of this work and are therefore reviewed in more detail. Macauley et al. [25] performed membrane durability ASTs and extrapolated acceleration factors to use level conditions, to build an empirical membrane durability model. Pucheng et al. [16] analyzed 1300 hours of fuel cell bus field data from 2008, and found 10% voltage loss after 1100 hours. They constructed AST protocols for different parts of the drive cycle (including start-up/shut-down, and load cycles), and obtained degradation rates for each. However, the ASTs were run between 50 and 100hrs (depending on which drive cycle part it was), and linear degradation rates were inferred from these short durations. Furthermore, potential was limited to 0.7 V on the low side, and below OCV on the high side by applying 10 mA/cm<sup>2</sup> during idle conditions. In 2015, Pucheng et al. used the same method to extrapolate 800 hours of field operation (for two

busses) to 10% voltage loss and predicted 1900 and 2600 hours [26]. Zhang et al. [27] developed a model based on fuel cell load demand. The non-parametric degradation model developed by Suk Joo et al. [19] can predict degradation due to start-up/shut-down cycles. The US National Renewable Energy Laboratory (NREL), which is part of the DOE, stated an average fuel cell durability of 2149 hours (until 10% voltage loss), with a maximum projected durability of 4130 hours [28].

A model for a fuel cell component which can predict the durability of that component, can be combined with models for other fuel cell components to achieve a comprehensive fuel cell durability model. Such a model can then be extrapolated to a fuel cell stack durability model. Furthermore, fuel cell efficiency, drive train configuration, and fuel storage may be considered as well, to form a fuel cell vehicle model. With fuel cell life predicted from the durability model, a life cycle assessment (LCA) can be carried out to determine the cost and emissions of a fuel cell vehicle over its lifetime. The FleetLCA tool, currently being developed by SFUs Fuel Cell Research Laboratory (FCReL), contains capabilities to do just that, perform LCA on fuel cell vehicles with a unique engineering approach. In addition, it allows for comparison of fuel cell vehicles against battery-electric, hybrid and gasoline/diesel drive trains, and factors in fuel price predictions, economic incentives, and future carbon penalties. Ahmadi and Kjeang estimated a break-even point of total life-time cost of fuel cell vehicles vs. gasoline vehicles at 6300 hours of operation [29].

## **1.4. Objectives**

The overall objective of this work is to degrade PEM fuel cell cathode electrodes under controlled conditions to build empirical datasets to lay the foundation for a better understanding of fuel cell durability. The dataset is then used to develop an empirical cathode electrode durability model, which outputs voltage loss as a function of drive cycles applied to the fuel cell and predicts voltage loss due to electrode degradation under use conditions. Specifically, the model shall be able to account for two types of drive cycle conditions: load cycling, and start-up/shut-down cycling.

Further objectives to facilitate the main objective are to develop small scale fuel cell testing procedures and knowledge, including fuel cell assembly and operation, catalyst

layer fabrication, accelerated stress testing, test automation, and advanced fuel cell diagnostics.

## Chapter 2. Fuel Cell Fabrication

The central component of any experimental fuel cell study is of course the fuel cell itself. While there are many components that make up a fuel cell, its heart is the membrane electrode assembly (MEA). The MEA is composed of a membrane, catalyst layers (CL), microporous layers (MPL), and gas-diffusion layers (GDL), arranged as shown in Figure 10.

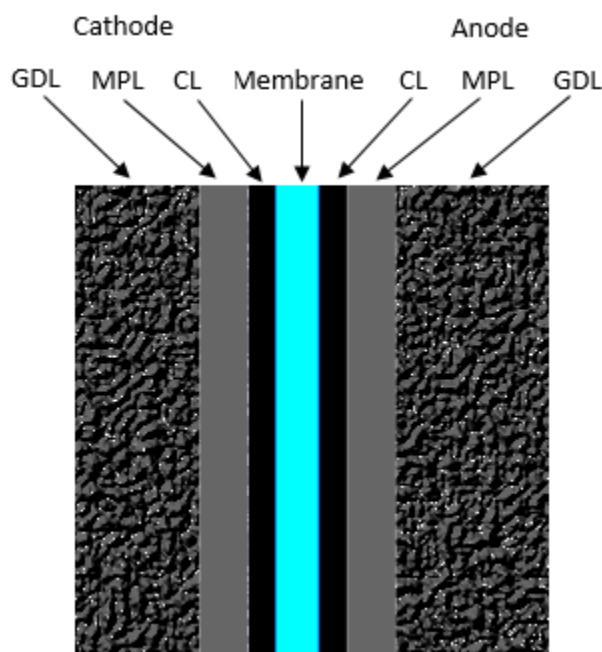


**Figure 10: Membrane Electrode Assembly**

All MEA components are commercially available from several vendors (fuelcellstore.com, nafionstore.com, fuelcellearth.com), even the MEA itself. The membrane, and the gas diffusion media are well specified and there is not much variance between products from different vendors. In contrast, to produce the catalyst layer, each vendor has their own, proprietary recipe and processes. This means that even if all parameters of the catalyst layer are specified, a significant variation exists between the performance of the catalyst layers from different vendors. Therefore, for this work, the catalyst layer was produced in-house.

Many different components and materials were used in the fuel cell manufacturing process. The materials and their usage are described in the following sections. For

reference, consumable materials used in each fuel cell are listed in Table 1 along with their manufacturers and suppliers. Similarly, the fuel cell hardware components are listed in Table 2.

**Table 1: Details of materials used in fuel cell fabrication**

Name	Purpose	Manufacturer	Supplier	Part No.
NR-211	Membrane	Nafion	Fuel Cell Store	1600001-2
29BC	GDL	SGL	Fuel Cell Store	1592004
Pt/C 50 wt% Pt, High Surface Carbon	Catalyst Powder	Tanaka	Tanaka	TEC10E50E
D521 1100 EW at 5 wt%	Ionomer Dispersion	Chemours	Fuel Cell Store	72500221
Teflon Sheet	Gasket	DuPont	Fuel Cell Store	592863-4
Polyimide Adhesive Film	Support	3M	Digi-Key	3M10221-ND

**Table 2: Details of fuel cell hardware components**

Component	Manufacturer/Supplier	Part No.
Poco block, 5 cm <sup>2</sup> parallel flow field	Fuel Cell Technologies	5SCH-PB
Heated endplate	Fuel Cell Technologies	5SCH
Gold-plated current collector	Fuel Cell Technologies	5SCH
Air bladder	Greenlight Innovation	FCCJ-001

The next section describes the fabrication method of the catalyst layer followed by the assembly method of the MEA.

## 2.1. Catalyst Layer Fabrication

The main objectives for catalyst layer fabrication are to control catalyst loading, layer thickness and layer porosity in a reliable, reproducible way. These objectives can be achieved, to varying degrees of success, by various methods including doctor blade/decal transfer, hand painting, air spraying, pulse spray swirl, ultrasonic spray deposition and ink jet printing [30], [31].

Simon Fraser University is home to 4DLabs (4dlabs.ca), a materials science research institute offering services for the design, development, demonstration and delivery of advanced functional materials and nanoscale devices. 4DLabs' inventory of fabrication tools includes a Sono-Tek ExactaCoat sonic spray coater. This spray coater was used to fabricate the catalyst layers used in this study. Besides its convenient availability, it was selected due to available support from other groups [31] who used it, as well as its automated, reliable and repeatable operation.

Any ultrasonic spray coating systems requires a few variables to be set to achieve a desired result. The main variables are surface temperature, flowrate, shaping air, run power, and idle power. The latter two control the sonic nozzle during operation and idling respectively. Idle power was used to disperse drop formation at the nozzle during idle. As a result, a fine mist is expelled from the nozzle during idle. While not ideal, the droplets that otherwise form often land on the coating area, resulting in large agglomerates.

**Table 3: Sono-Tek Exactacoat Setting for Pt/C ink CCM**

Name	Value	Unit	Description
$T_s$	85	$^{\circ}C$	Table temperature
$V_{ink}$	0.37	ml/min	Ink flowrate
$P_{air}$	0.78	kPa	Shaping air pressure
$P_{run}$	3	W	Sonicator run power
$P_{idle}$	0.5	W	Sonicator idle power

Once all parameters of the sonic spray coater are set, a substrate can be coated. The catalyst layer is sandwiched between the GDL and the membrane. Therefore, either the membrane or the GDL are suitable as substrates for spray coating. The product of applying a catalyst layer to the GDL is known as a gas diffusion electrode (GDE), whereas if the membrane is used as a substrate it is referred to as a catalyst coated membrane (CCM). Since it is generally accepted that CCMs provide better performance over GDEs [32], CCMs were produced for this study. To ultimately achieve a 5 cm<sup>2</sup> active area sample, a 16 cm<sup>2</sup> piece of membrane (as specified in Table 1) was placed under a mask with locating markers and onto the spray coater surface. The mask had a 6 cm<sup>2</sup> cut-out, to produce a 6 cm<sup>2</sup> CCM. The catalyst frame created by the difference between 5 and 6 cm<sup>2</sup> was used during assembly as described in section 2.2. Both sides of the membrane were coated in the same way, to produce equal anode and cathode electrodes.

It was determined that 28 to 30 coating cycles per side yield a suitable (as determined by the consistency of the in-situ results) catalyst loading, structure, and thickness on anode and cathode. To determine the loading, the weight of each side of the CCM was measured during fabrication, and compared to the weight of the bare membrane. Since weight measurements fluctuate as a function of membrane temperature, the measurements were obtained 90 s after removing the sample from the heated surface at each step (bare membrane, anode side coated, anode and cathode sides coated).

### 2.1.1. Catalyst Ink

In order to be able to deposit the catalyst layer using a spray coater, a liquid or ink has to be synthesized to conform with the maximum allowable amount of solids required by the spray coater to be used. Exceeding this maximum limitation can result in clogging lines or damaging the sonic nozzle. In the case of the ExactaCoat sonic spray coater, the requirement is that any solution used, be less than 2 % solids by weight. The inks used in this study were designed to have between 0.5 and 1 % solids by weight – well below the 2 % limit. For a Pt/C loading of 0.5 mg/cm<sup>2</sup> on a 5 cm<sup>2</sup> active area, 2.5 mg of Pt/C are required. In addition, ionomer must be added to the ink to facilitate ion transport in the catalyst layers. However, the amount of ionomer must be carefully balanced to achieve a maximum ionomer loading while maintaining sufficient porosity. Britton et al. [33] evaluated the effect of deposition parameters on the porosity of the catalyst layers and found that for the spray coating parameters described above, a 30 % ionomer loading is appropriate. Therefore, every gram of Pt/C, should contain 30 % ionomer, thus a total weight of 3.57 mg solids is required. To achieve 1 % solids by weight, 0.353 g of solvent must be added.

The active area is expanded to support the membrane (see section 2.2), and about 5 mL of ink is needed to fill the lines between the syringe and the nozzle of the ExactaCoat. In addition, samples were fabricated in batches of four per spray coating session. Therefore, a minimum of 30 g of ink were used per four samples.

Ionomer can be used in different forms: dry, as a water based dispersion, or as an alcohol based dispersion. For this work, D521 Nafion™ dispersion was used, which is alcohol based (50 wt. % VOC, 45 wt. % H<sub>2</sub>O).

Considering all the above, the components of the ink can be calculated as shown below.  $W$  is the desired, total weight of the ink (e.g. 30 g), and  $Ionomer$  is the amount of dry ionomer in the ink:

$$Ionomer = 0.01 * 0.3 * W$$

$$D521 [g] = \frac{Ionomer}{1 - (0.45 + 0.50)}$$

$$Pt/C [g] = W * 0.01 * 0.7$$

$$MeOH [g] = (W - (Pt/C + Ionomer) * 0.50) - (D521 * 0.50)$$

$$H_2O [g] = (W - (Pt/C + Ionomer) * 0.45) - (D521 * 0.45)$$

## 2.2. Membrane Electrode Assembly

Having fabricated a CCM the MEA can be built. The SGL 29BC gas diffusion medium was used in this work. The most important, additional components are hard stop gaskets (for details see Table 1). These gaskets are used to a) enclose the sides of the diffusion medium to prevent gas leaks, and b) to control how much the diffusion medium is compressed. In addition, by fitting the gaskets with strategically placed holes, locating pins can be used to align the gaskets inside the fuel cell hardware. Since the gasket encloses the diffusion media, they will also be aligned.

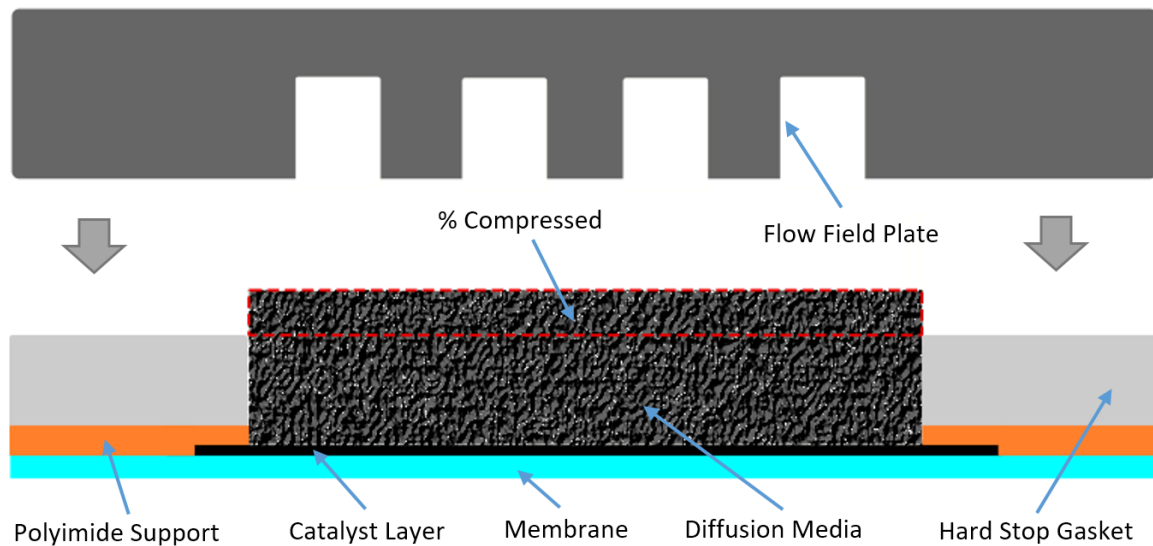


**Figure 11: MEA Components and Compression**

The CCM, however, is difficult to align. While attempting to fit the excess membrane around the CCM with holes for locating, it was found that the membrane is too thin for the holes to have the desired effect. Simply placing the CCM inside the fuel cell hardware also did not work, as it shifts unpredictably during hardware assembly. To align the CCM, it was enclosed on both sides with adhesive polyimide film made by 3M purchased through Digi-Key Canada (Table 1). The film provides just enough thickness, so that, when fitted with locating holes, it keeps the CCM in place inside the fuel cell hardware. The tape was cut with a die to have a square hole in the middle of the same

size as the active area. To apply the adhesive tape to the CCM, the CCM was placed on a vacuum table to keep it in place.

Figure 11 shows a schematic of one half of an MEA and the components used for assembly and to help achieve the desired GDL compression. Figure 12 shows a picture of one side of an MEA without gaskets.

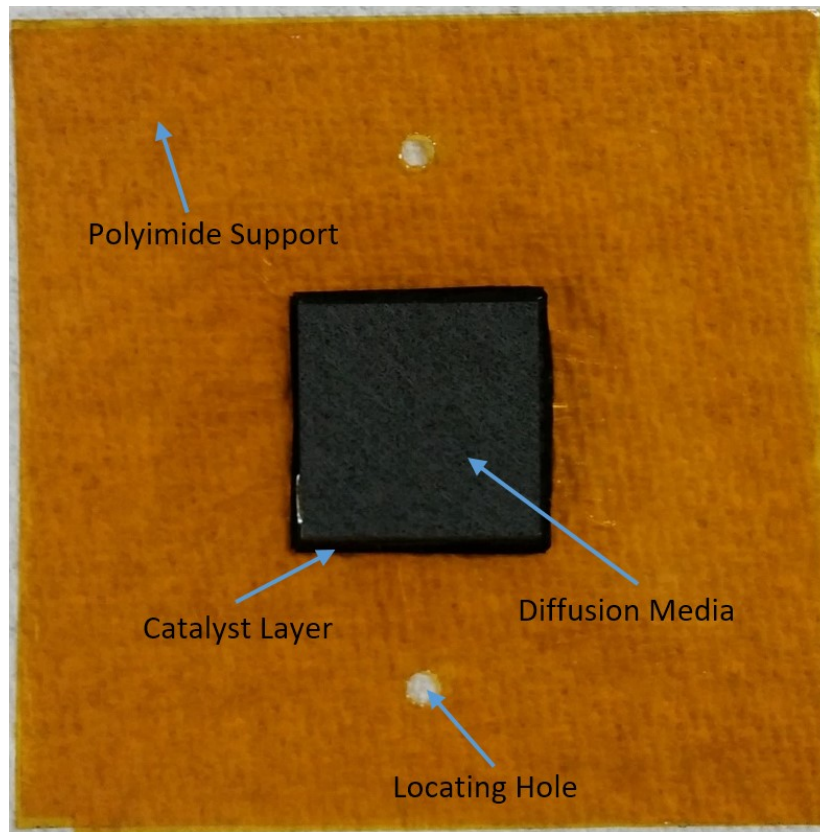


**Figure 12: Membrane Electrode Assembly**

## Chapter 3. Experimental Methods

A variety of different methods, materials, and devices were used in the experimental design. The following sections describe the testing hardware, custom automation techniques, and test protocols used to obtain the results presented in Chapter 5.

### 3.1. Test Stand and Fuel Cell Hardware

The fuel cell samples require fuel and oxidant gases to produce voltage. To produce repeatable results, the gases must be supplied under precisely controlled conditions such as flow rate, temperature, pressure, and humidity. The control of operating conditions was provided by a Greenlight Innovation G20 fuel cell test station (G20).

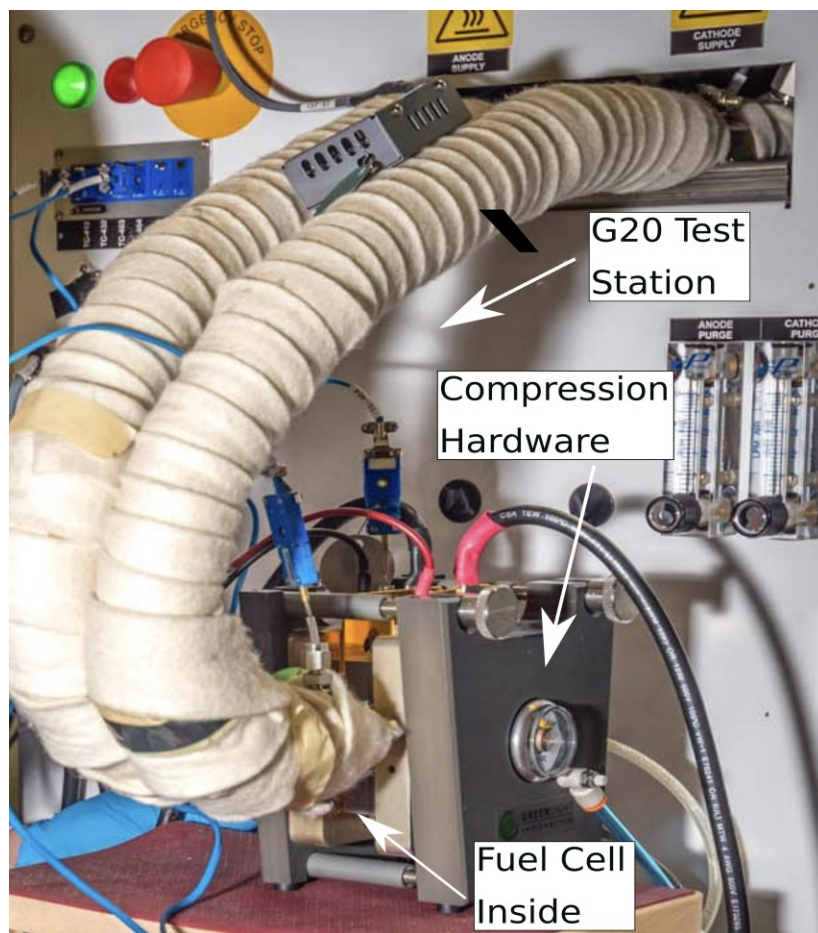


Figure 13: Fuel Cell Hardware

To deliver the gases evenly to the surface of the MEA, a single cell hardware with 5 cm<sup>2</sup>, parallel flow fields with 0.77 mm channel width was used (details in Table 2). This hardware also included gold plated current collectors, and end-plates fitted with resistive heating rods to keep the cell at a constant temperature. The cell was compressed using a pneumatic compression jacket (air bladder) from Greenlight Innovation, which allowed for repeatable, uniform, compression to 4.5 bar. The compression hardware was constantly supplied with air at 4.5 bar. Even though the compression hardware can maintain pressure without a continuous supply, the 4.5 bar supply was always connected, since most tests ran for several days. Figure 13 shows a picture of the fuel cell hardware inside the compression jacket and connected to the G20 test station.

Table 4 shows the fuel cell operating conditions generally used, unless specified otherwise. Ambient air compressed to 5.5 bar was used to supply the G20. Nitrogen at 99.998 % purity and hydrogen at 99.95 % purity were supplied to the station from cylinder banks.

**Table 4: General fuel cell operating conditions**

Temperature [°C]	RH [%]	Pressure [kPag]	Anode Flow [slpm]	Cathode Flow [slpm]	Anode Gas	Cathode Gas
80	90	80	0.5	0.5	H <sub>2</sub>	Air

## 3.2. In-Situ Diagnostics

Any fuel cell specimen will be subject to certain expected and unexpected performance losses. To quantify such performance losses, and explain why they occur, diagnostic techniques can be employed. The three main fuel cell diagnostic techniques used in this work, polarization curves, cyclic voltammetry, and impedance spectroscopy, are introduced in this section.

Diagnostics techniques such as cyclic voltammetry and electrochemical impedance spectroscopy require high precision electronics such as a potentiostat. A Gamry Interface 5000E was used for diagnostics. Table 5 shows the fuel cell operating conditions used for diagnostics and similar protocols.

**Table 5: Diagnostic fuel cell operating conditions**

Temperature [°C]	RH [%]	Pressure [kPag]	Anode Flow [slpm]	Cathode Flow [slpm]	Anode Gas	Cathode Gas
80	90	60	0.1	0.1	H <sub>2</sub>	N <sub>2</sub>

### 3.2.1. Polarization Curves

The performance of a fuel cell can be assessed by applying different loads and measuring its voltage output. Such measurements result in a characteristic curve known as the polarization curve. The voltage drops along the polarization curve can be used to determine potential faults in the various components of the fuel cell. Figure 14 shows a typical polarization curve for fuel cells used in this work. There are three main areas of interest. Between 0 A/cm<sup>2</sup> and ~0.25 A/cm<sup>2</sup>, the activation losses are dominant. Activation losses are due to what is sometimes referred to as “reaction friction”, i.e. losses associated with the chemical reactions. Between ~0.25 A/cm<sup>2</sup> and 1 A/cm<sup>2</sup>, the polarization curve is approximately linear, because the ohmic losses are dominant. The ohmic losses are due to anything that constrains or prolongs the pathway of electrons (such as wires, plates, GDL, and CL), and ions (such as the membrane) [3]. Finally, at ~1 A/cm<sup>2</sup> and above, the mass transport losses are dominant. These are losses associated with the rate at which fuel and oxidant can reach the reaction sites. This rate is often limited due to flooding of pores inside the gas diffusion medium, which blocks access to reaction sites. Since the water production inside the fuel cell increases with current demand, flooding becomes more likely at higher current densities.

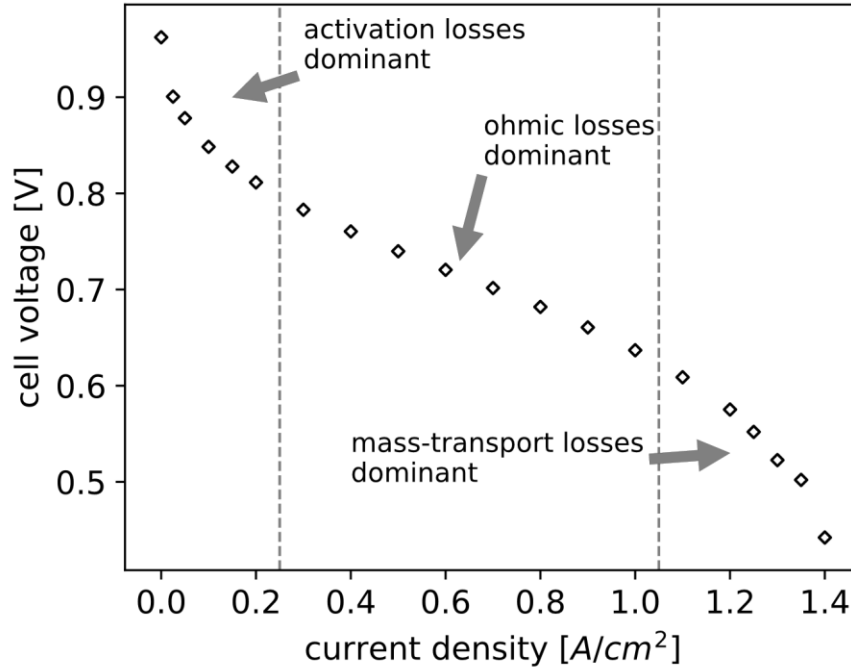


**Figure 14: Polarization Curve**

### 3.2.2. Cyclic Voltammetry

Voltage losses which can be seen in the polarization curves can be used to determine how well a given fuel cell is performing. However, it is usually not clear from the polarization curve alone which fuel cell component is causing high or low fuel cell performance. Therefore, other techniques are needed to obtain more information about the condition of individual fuel cell components. Cyclic Voltammetry (CV) is an electrochemical measurement technique where a triangle wave voltage signal is swept between voltage limits, while the fuel cell current is measured. The resulting curve, known as a voltammogram, is characteristic of different chemical reactions which occur at specific voltages inside the fuel cell. It can be used to obtain certain pieces of information about the catalyst layer, and the membrane. Cyclic voltammetry is performed with hydrogen on the anode and a low flow, inert gas (such as nitrogen) on the cathode. Under these conditions, the hydrogen protons adsorb onto reaction sites of the cathode catalyst layer, and combine with electrons.

Figure 15 shows a typical voltammogram for a fuel cell used in this work. Between voltages of ~50 mV and ~300 mV, the hydrogen atoms which sit on the platinum (Pt) reaction sites, desorb and release their electrons ( $e^-$ ) to generate a current. As the voltage

increases further, the current decreases as all  $H^+$  are desorbed, until a steady exchange current is reached. This current is due to a capacitance which is created by an electrochemical double-layer. Once the voltage falls below  $\sim 300$  mV,  $H^+$  is adsorbed again, and the current decreases.

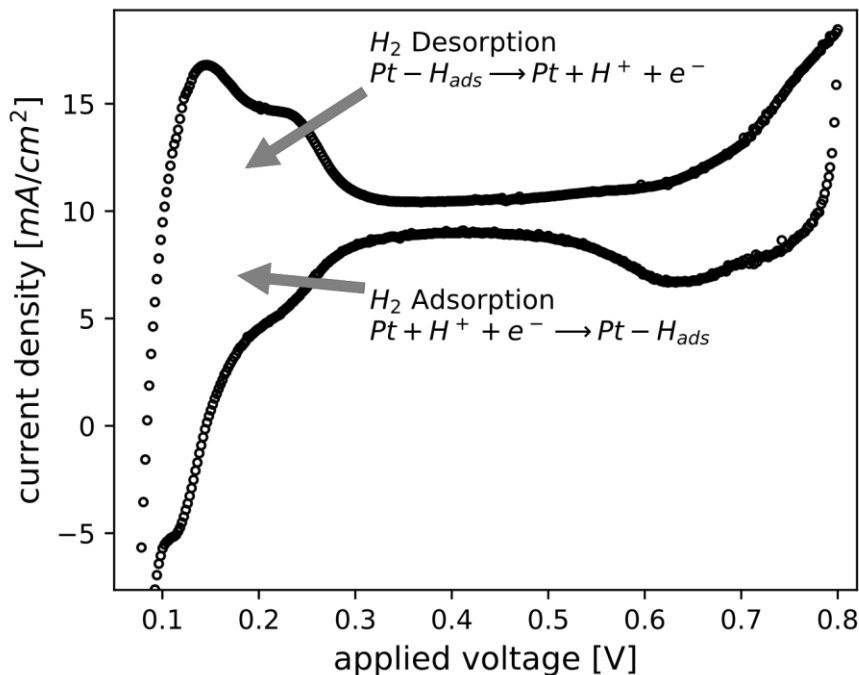


**Figure 15: Cyclic Voltammogram**

A parameter frequently studied is the electrochemically active surface area (ECSA). This area is an indication of how much platinum is accessible and takes part in the fuel cell reactions. Since the ORR is the slower, more critical reaction, ECSA is measured for the ORR in this study. The ECSA can be calculated from the area under part of the CV curve. Figure 16 shows the relevant portion of the voltammogram to illustrate the steps taken in this work to compute the area used to calculate the ECSA. First, the lowest point (M) in the linear region is found. The current density value of this point is used as the horizontal boundary for integration (3). The left, vertical integration boundary is defined by the intersection of line (3) and the voltammogram. The right, vertical integration boundary is set to the vertical line at 0.4 V (1). However, if the voltage component of M is smaller than 0.4 V, it is used as the right, vertical integration boundary instead (2). Finally, M is subtracted from each point of the voltammogram to move the curve to the x-axis, where the integral is computed.

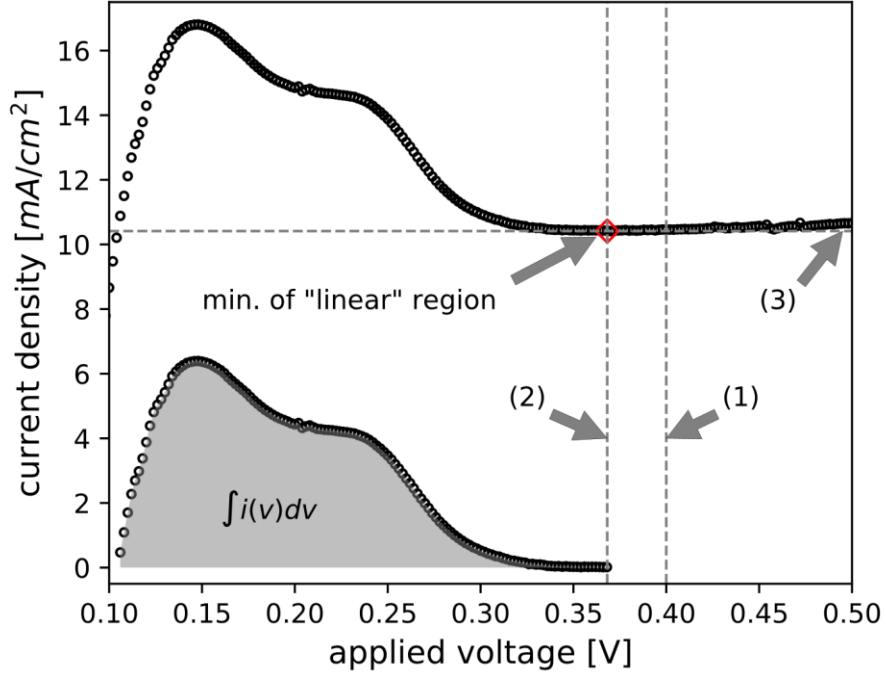


**Figure 16: ECSA integration boundaries**

(1) default high voltage boundary, (2) high voltage boundary adjusted to voltage value of minimum, (3) current boundary through current of minimum.

The ECSA is calculated from the area under the hydrogen desorption peak, a proportionality constant  $S$  and the catalyst loading  $C$  as shown in Equation 10.

$$ECSA = \frac{\int I(t)dt}{S \times C} = \frac{m^2}{g_{catalyst}} \quad (10)$$

The area shown in Figure 16 is the integral of the current density with respect to the voltage, but Equation 10 requires the integral of the current with respect to time. Therefore, the conversion shown in Equation 11 is performed before integration:

$$I(t) = i(v \times r) \times A \quad (11)$$

where  $r$  is the scan rate of the cyclic voltammogram:

$$r = 0.020V/s$$

The catalyst loading  $C$ , must be in grams of catalyst. For the fuel cells used in this work, the catalyst loading is set to  $0.5 \text{ mg/cm}^2$ , for both anode and cathode, and the active area is  $5 \text{ cm}^2$ . Therefore:

$$C = 0.5 \text{ mg/cm}^2 \times 5 \text{ cm}^2 = 2.5 \text{ mg}_{\text{platinum}}$$

The proportionality constant  $S$  is used to relate the charge per unit area of catalyst to the effective catalyst active area. For platinum this is [3]:

$$S = 210 \mu\text{C/cm}^2$$

Typical values for the ECSA of this type of fuel cell are  $30 \text{ m}^2/\text{g Pt}$  [33].

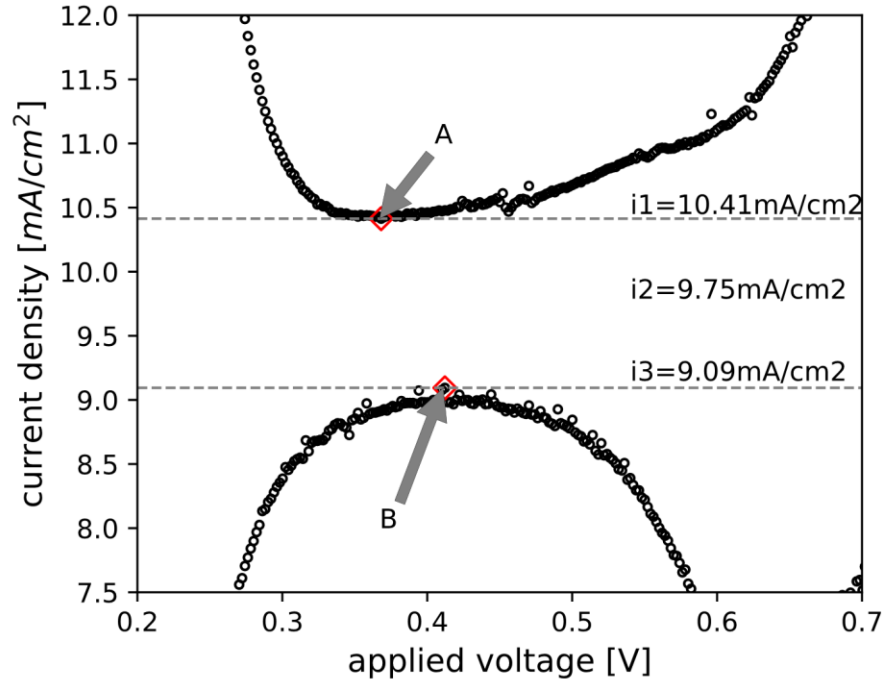


**Figure 17: Double layer capacitance current and crossover current approximation** (A) upper minimum of linear region, (B) lower maximum of linear region, ( $i_1$ ) and ( $i_3$ ) current densities used in double layer capacitance and crossover current calculation.

Figure 17 shows the double-layer region of the voltammogram (0.35-0.5 V). From this plot, three current densities can be obtained: the minimum current density of the upper portion  $i_1$ , the maximum current density of the lower portion  $i_3$ , and the midpoint current density between  $i_1$  and  $i_3$ :  $i_2$ . The midpoint between  $i_1$  and  $i_3$  is the current density associated with fuel ( $\text{H}_2$ ) crossover from the anode to the cathode (Equation 12):

$$i_x = i_2 \quad (12)$$

The double-layer charging current is the difference between either  $i_1$  or  $i_3$  and  $i_x$ :

$$i_{dl} = i_1 - i_x \quad (13)$$

Using the double layer charge current, the double layer capacitance can be calculated as per Equation 14, where  $r$  is again the scan rate of the cyclic voltammogram.

$$C_{dl} = \frac{i_{dl}}{r} \quad (14)$$

For fuel cells similar to those used in this study  $i_x$  is typically on the order of 3 mA/cm<sup>2</sup>, and  $C_{dl}$  is on the order of 1.1 mF/cm<sup>2</sup>.

### 3.2.3. Electrochemical Impedance Spectroscopy

Another useful diagnostic technique uses sine waves of either voltage or current which are super imposed onto the fuel cell voltage or current, respectively. The frequency of the sine wave is varied, and the fuel cell response is measured at each frequency. The voltage or current frequency, magnitude and phase data can be converted to complex impedance using the fast Fourier transform.

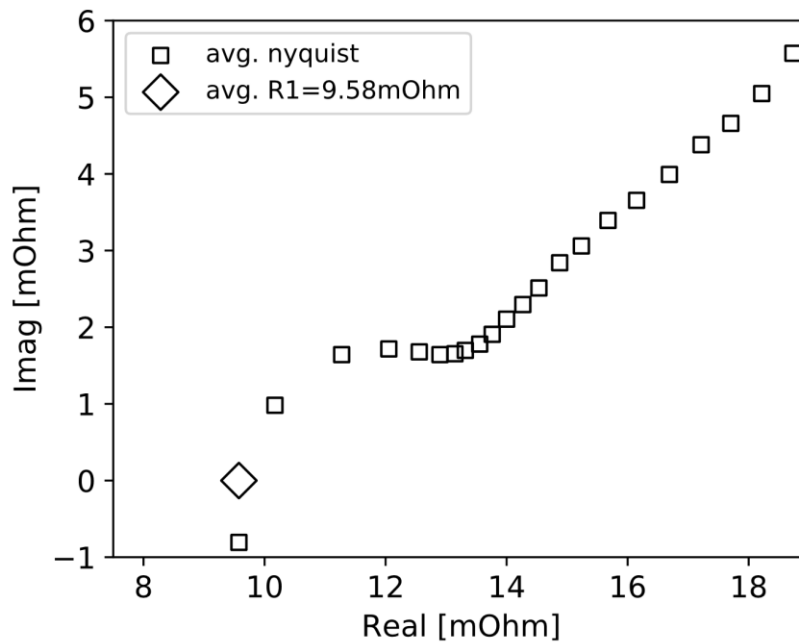


Figure 18: Nyquist Plot

The complex impedance is usually plotted as Nyquist plots, such as the one shown in Figure 18. From the Nyquist plot, several parameters can be obtained to model a fuel cell to an equivalent electrical circuit. However, for this work, only the ohmic resistance  $R_1$  is of interest. The high frequency resistance  $R_1$  is the real part of the complex impedance at zero (or near zero) phase.

### 3.3. Degradation Testing

Degradation experiments were carried out to simulate fuel cell aging under controlled conditions, which approximate two specific types of vehicle operation: load cycling and start-up/shut-down cycling. Both conditions cause cathode electrode degradation, and were therefore of interest to this study. The details of the experiment designs are discussed next.

#### 3.3.1. Load Cycling

The load cycle degradation test was based on the US DOE [6] electro catalyst degradation protocol, which simulates load cycles by switching between a lower potential limit (LPL), and an upper potential limit (UPL). The UPL was set to 0.98 V and held for a duration of 3 s. The lower potential limit was varied among 0.6, 0.7, and 0.8 V, and held for 3s. Data from a load cycling experiment showing this protocol is plotted in Figure 19. The general operating conditions (Table 4) were used for this test. The tests were run until 30k load cycles were completed, with diagnostics at 0, 1k, 5k cycles, and every 5k cycles after that.

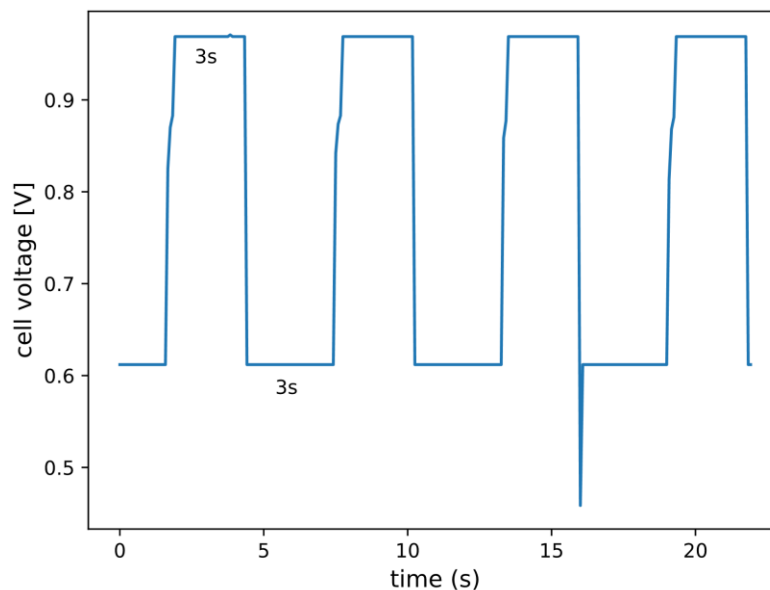


**Figure 19: Voltage data from load cycle protocol implementation**

The G20 station is equipped with a programmable load. However, the time required for it to switch between on and off, is too long to achieve steady state during the

relatively short load cycles. Therefore, an external, programmable load (BK8500) was used instead to achieve the LPL. The UPL was achieved using the Gamry Interface 5000E, which was also used for diagnostics.

### 3.3.2. Start-up/Shut-down Cycling

To achieve sharp H<sub>2</sub>/Air fronts during start-up and shutdown, respectively, the gas switching should occur a) as close to the inlets as possible, and b) from continuously flowing gas. To achieve this, a two-way, Burkert magnetic valve was connected with a tee fitting to the air inlet. When the valve is off, air flows through the cathode. When the valve is on, air flows through the cathode, but also out of the valve. The other end of the valve was connected to the anode inlet. A three-way, Burkert magnetic valve was connected to the anode with a tee. The other two ends of this valve were connected to a hydrogen exhaust, and to the hydrogen supply. When this valve is on, the hydrogen flow is diverted away from the fuel cell into the exhaust. Therefore, when both valves are switched on, air flows through the cathode and the anode, and hydrogen flows to the exhaust. If this is followed by switching both valves off, hydrogen displaces the air on the anode, and air flows through the cathode only. Figure 20 illustrates the start-up/shut-down test setup.

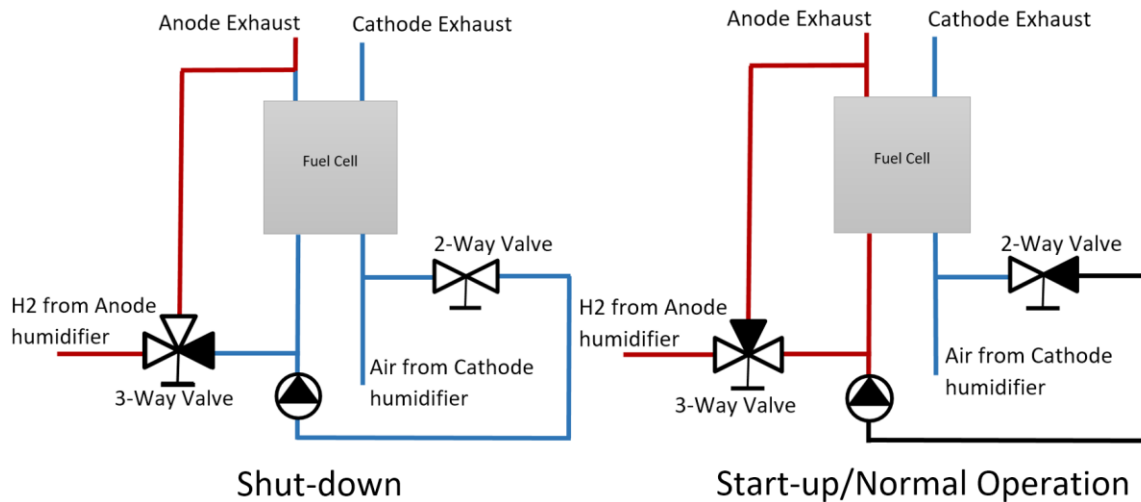


**Figure 20: Start-up/shut-down test setup schematic**

With the test setup described above, a modified version of the US DOE unmitigated start-up/shut-down protocol [6] was implemented. It was modified to shorten the shut-down and start-up durations to 20-seconds each (Figure 21). The DOE protocol was designed with 25 to 50 cm<sup>2</sup> hardware in mind, but 5 cm<sup>2</sup> hardware was used in this

study. Therefore, shorter durations are appropriate. This protocol was run until 5k start/stop cycles were completed, with diagnostics at 0 cycles, and every 1k cycles after that.

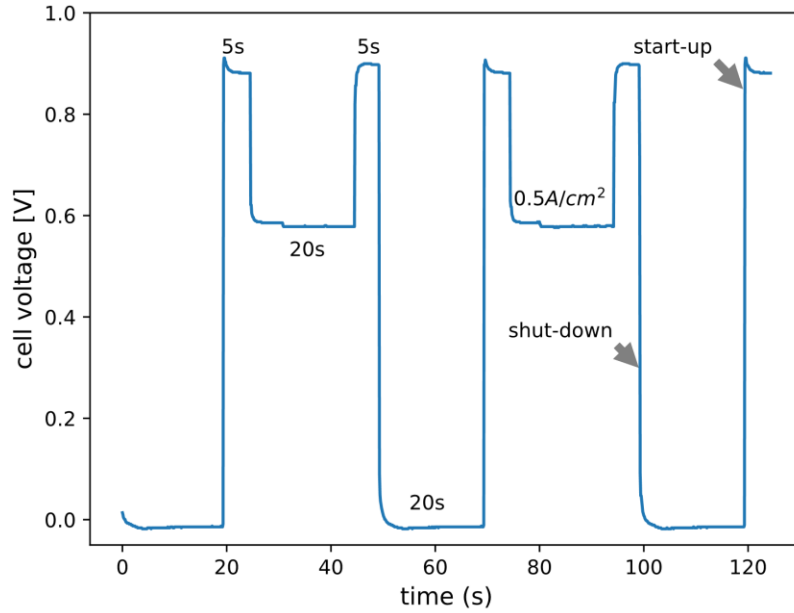


**Figure 21: Voltage data from start/stop protocol implementation**

## 3.4. Conditioning and Recovery

This section describes the fuel cell conditioning procedure, as well as a recovery protocol which was used to recover reversible losses after degradation cycles, and before performing diagnostics.

### 3.4.1. Conditioning

Fuel cell conditioning was used to break in each new sample. A few different techniques were used for conditioning including cyclic voltammetry, constant current conditioning, and air starvation. Cyclic voltammetry is used to cycle the fuel cell voltage to induce hydrogen evolution. As the hydrogen evolves on the cathode catalyst, the porosity and tortuosity of the catalyst layer improve, leading to an increase in the number of available reaction sites. Constant current conditioning over several hours is used to a) ensure full hydration of the membrane and the ionomer inside the catalyst layer, and b) to improve and stabilize component interfaces. Finally, air starvation (or air braking) causes reducing conditions on the cathode due to the absence of oxygen. As a result, oxidized species will be reduced [34]. The overall goal of conditioning is to achieve maximum stable performance. The total conditioning procedure takes approximately 24 hours. The steps were carried out as follows:

1. Conditioning was started with 200 cyclic voltammetry cycles, at 50 mV/s, between 0.2-0.8 V. For this step, the operating conditions were according to Table 5.
2. The CVs were followed by 5 cycles of air starves. The conditions were similar to those in Table 4, and a load of  $500 \text{ mA/cm}^2$  was applied. For each cycle, cathode air was replaced with nitrogen until voltage dropped to 200 mV. At this point the load was reduced to hold the voltage constant, until a load value of 200 mA was reached. Air was returned to the cathode and nitrogen turned off. This was repeated 5 times.
3. Next, 6 hours of constant load were applied. For each cell, the load was automatically chosen to be so that a voltage of  $700 \text{ mV} \pm 15 \text{ mV}$  was achieved. For nearly all fuel cells this resulted in a load of  $700 \text{ mA/cm}^2$ .

4. Step 2 was repeated.
5. Step 3 was repeated.
6. Step 2 was repeated.
7. Step 3 was repeated for 8 hours instead of 6.

### 3.4.2. Recovery

Table 6 shows the protocol used for the recovery step. This step was performed prior to any diagnostics cycle, to eliminate any influence of reversible losses. Reversible losses can result from contaminants, such as CO and CO<sub>2</sub>, created by degradation reactions discussed in Section 1.3.1. These contaminants can obstruct access to the cathode catalyst layer, and therefore, reduce performance. In addition, flooding may have occurred during degradation testing, which will also reduce performance. Gas at high flowrates on the anode and cathode can clear pooling water (steps 1 and 4). In addition, air on the cathode can undo some of the degradation reactions (step 2) [3]. Finally, removing oxygen from the cathode (step 4) will reduce oxidized species [34].

**Table 6: Recovery Protocol**

Step	Step Name	Anode Gas	Anode Flow [slpm]	Cathode Gas	Cathode Flow [slpm]	Duration [s]
1	N <sub>2</sub> soak	N <sub>2</sub>	3	N <sub>2</sub>	3	120
2	Air soak	N/A	0	Air	3	900
3	N <sub>2</sub> soak	N <sub>2</sub>	3	N <sub>2</sub>	3	120
4	H <sub>2</sub> soak	H <sub>2</sub>	3	N/A	0	600
5	H <sub>2</sub> -air back on	H <sub>2</sub>	0.4	Air	1.2	5

### 3.5. Automation

A special feature of the experimental setup used in this study was its degree of automation. While most modern fuel cell test stands are automated to some degree, most are not fully automated. The reason for less than 100 % automation is likely because upgrading for automation can be costly. For example, a test system that was fully automated when it was purchased, possibly using large amounts of funding, will likely need modifications as the project evolves. Most researchers do not have to know-how to modify sophisticated test stands without sacrificing automation. Instead, modifications manifest as external equipment, which must at least be connected, or activated manually.

This was also the case for this study. The G20 test stand could perform temperature, humidity, flowrate, data-logging, safety limit monitoring, real time data plotting, and all combinations of these features automatically (with the help of a custom scripting tool). However, EIS and CV diagnostics, and load cycling ASTs required manual intervention. While this is a common situation, not just in fuel cell research labs, there are a few concerns to note:

First, manual intervention always wastes a lot of time. In the case of this study, the AST required diagnostics to be taken at specific intervals during the test, for example after 1000, 5000, and 10000 cycles. Even if each cycle only takes 6s, it still takes more than 8 hours for 5000 cycles to be completed. On many occasions, the diagnostic interval occurred in the middle of the night, which meant that the station was either shut down or idling until an operator was available to activate the diagnostics equipment. In the meantime, many hours of testing time were wasted. In addition, if the station was left to idle, fuel or purging gas was also wasted.

Second, since new ASTs are started at different times, the idling times vary from test to test, which may result in inconsistent data. For example, during this study it was observed that fuel cell performance could be impacted significantly by a single cooldown and warmup cycle.

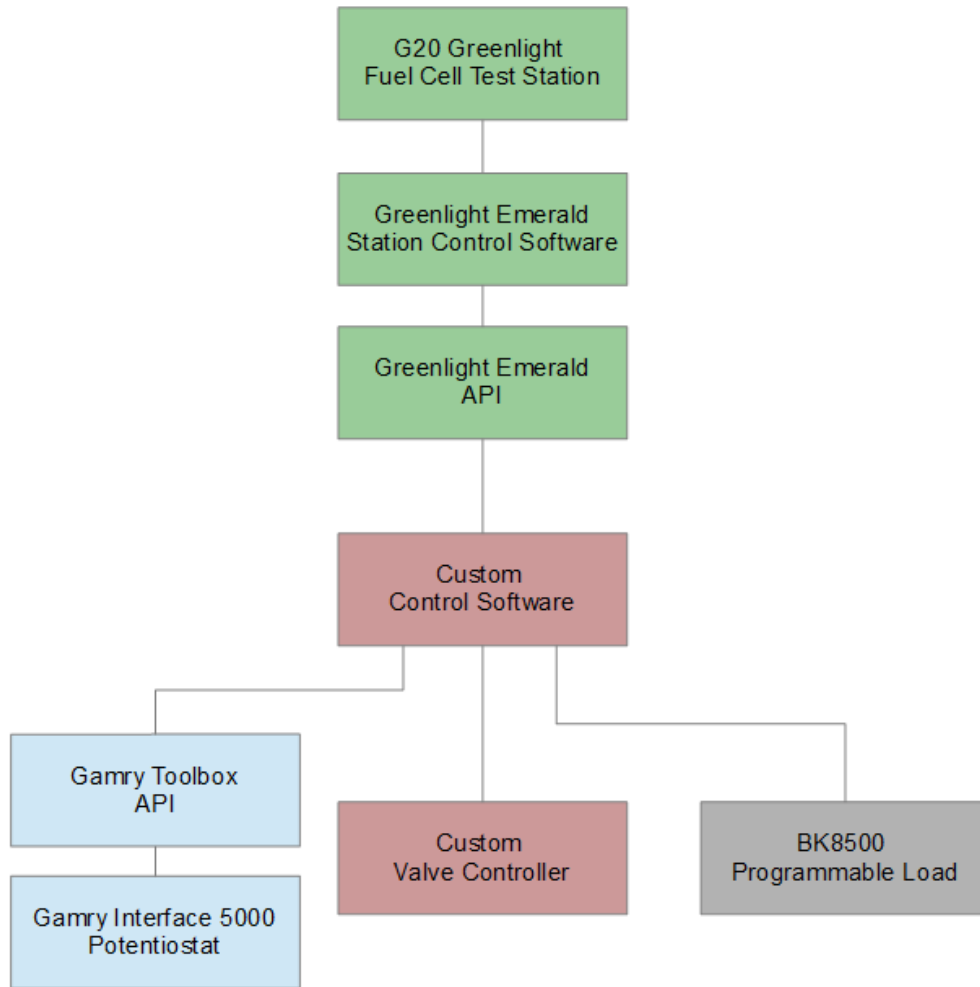


**Figure 22: Test System Diagram**

To avoid the above concerns, an effort was made to fully automate all aspects required for this study. The result was a test system which could run a 4 to 8-day degradation test including all diagnostics and break-in procedures without operator intervention. Figure 22 shows a high-level view of the test system. Since load cycle stress tests, start-up/shut-down stress test, diagnostics, and break-in all require different combinations of the potentiostat and the programmable load, as well as different fuel cell operating conditions, all devices must be centrally controlled so that the right device operates at the right time under the right conditions. The custom control software, named FCR<sub>e</sub>L Fuel Cell System Controller and developed mostly in Python, provided the central control, as well as a simple graphical user interface (GUI) to allow a user to see test progress and schedule different tests in different orders and even repeat certain sets of tests in a loop (Figure 23). The System Controller interfaced with the Emerald G20 control software through an application programming interface (API) supplied by Greenlight, to

set and read temperatures, gas flows, load, and more. It also interfaced with the potentiostat through its API from Gamry, to start tests and read/write data for CV, EIS, and stress tests (supply of UPL). The programmable load featured a simple RS232 based API through which the load could be set and current and voltage could be read. Finally, a custom valve controller was designed to operate magnetic valves to switch the cathode gas to nitrogen (for diagnostics) as well as to perform start-up/shut-down gas switching. The valves were controlled by sending commands via USB (universal serial bus) to an Arduino Uno Rev 3 microcontroller board which actuated the valves using a custom switching circuit shown Figure 24. With the help of this system, any combination of devices and conditions could be programmed into test routines and made available to the user via the GUI. With the GUI the user can build test scripts and monitor the progress of multi-day tests. Additional details of the components required to implement this automation can be found in Appendix B.

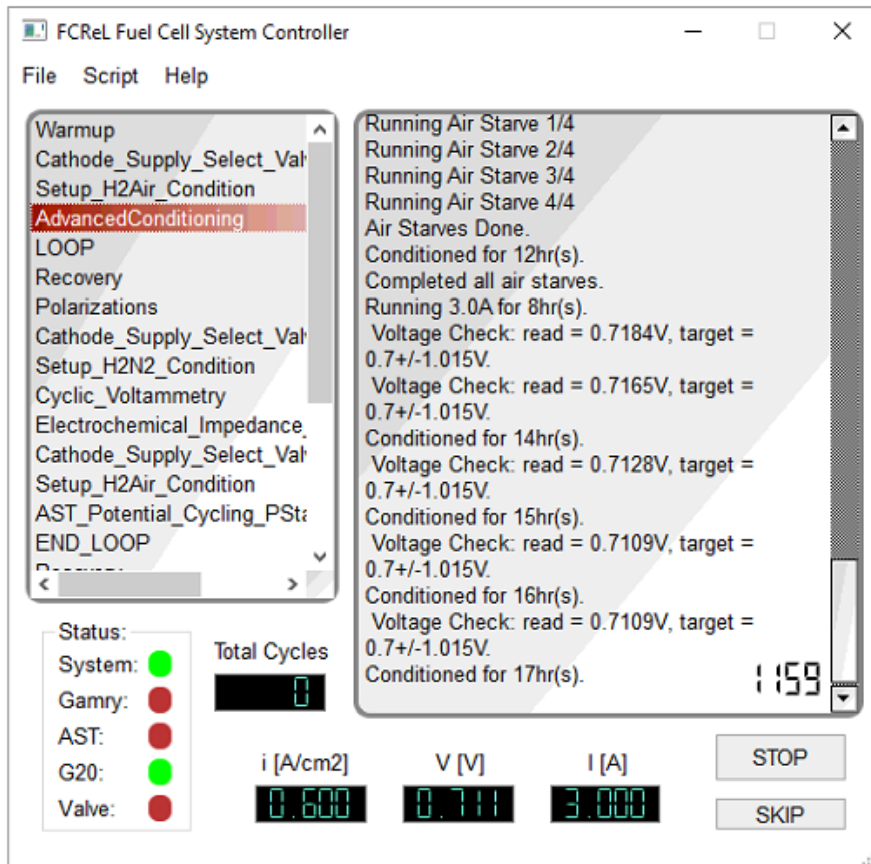


**Figure 23: Custom control software GUI**

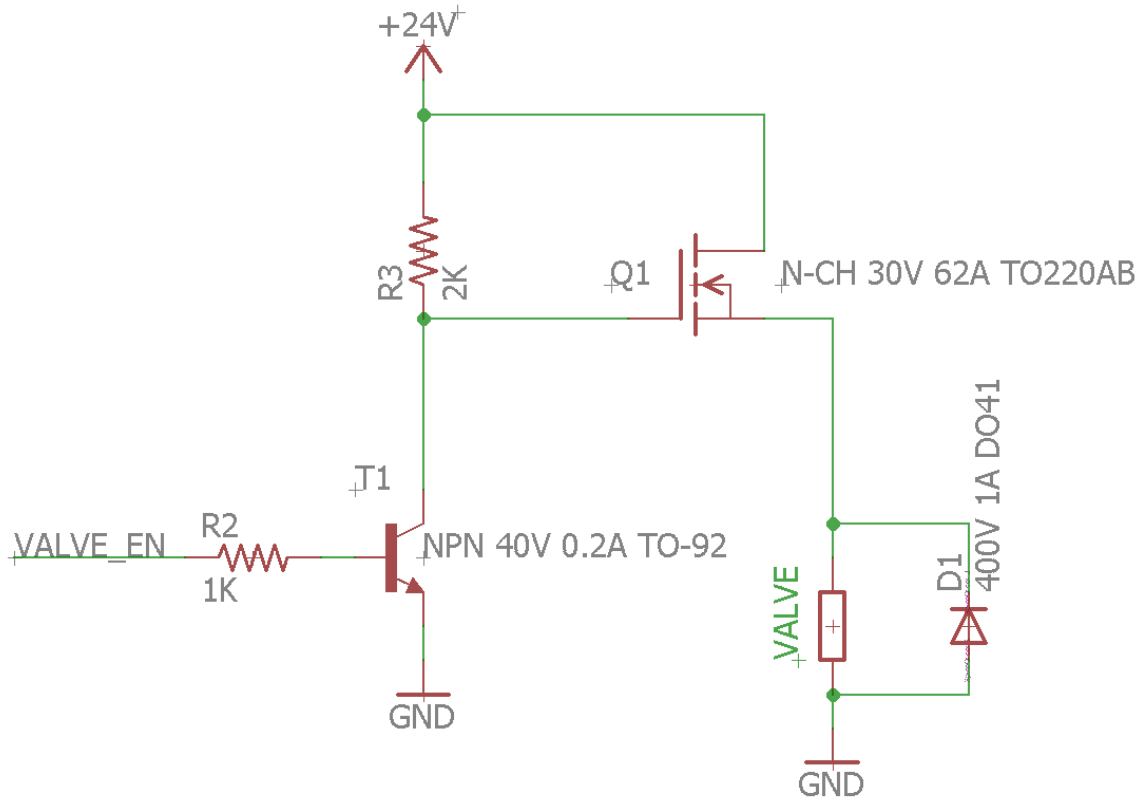


**Figure 24: Custom valve control circuit**

### 3.5.1. System Controller Software

The system controller software, which was developed as part of this work, controls several different devices with various communication protocols. It allows for numerous methods of user interaction through a GUI; logs test data; sends emails; and follows test plans. In addition, the software allows new tests and devices to be added with minimal modifications to the existing code. To achieve all this functionality several design patterns were used, most notably the model view controller (MVC) pattern and the observer pattern. The MVC pattern separates the GUI from the underlying model, where the model is often a data access layer. In this case, the model are the parts of the program which, given a test plan, schedule all the different devices according to the plan and log data in the process. This model is completely separate from the GUI, in that it could be run from a simple command line interface, or through a different GUI such as a web interface – all without any modifications to the model. The GUI was designed using the QT Designer program, which has its own graphical interface by which a developer can place controls such as buttons, text boxes etc. to build a custom GUI. The output of the QT Designer is

a xml-based file which contains the configuration of the GUI controls (buttons, indicators, text fields, etc.). Between the model and the GUI are controllers for the different controls of the GUI. A controller is aware of the xml file, so it can use the various controls and their names. In addition, it is also aware of the model, and the functions it possesses. The controller communicates with the GUI controls via QT signals; these signals can be attached to any control, and triggered by user interaction, or by the controller to modify the control on the GUI. For example, if a user presses a button a signal triggers a function in the button controller which calls the necessary functions of the model. Similarly, the model can send data to a text box controller, which uses a signal to update the text box control with that data. But, at this point, there is a problem: the model should not be aware of the functions of the controllers. If it was, it would be bound to this one set of controllers, and would therefore have to be modified to be used with a different interface. The observer pattern is used to avoid this problem. This pattern is built on the principle of subscriber and publisher. In this case, the publisher is the model, and the subscriber (or observer) is any program which wants to receive data from the model. This pattern is implemented by adding a function called "update" in every subscriber, and maintaining a list of subscribers in the publisher. This subscriber list is initially empty, and can be populated or modified at runtime. For example, when the system controller GUI starts, the controllers put themselves on the subscriber list of the model. Every time the model has an update, it calls the "update" function of each subscriber in the list, without knowing what will happen. The observer pattern is used as the main communication path not only between the model and the controllers, but also within the model itself.

With the help of the MVC and observer patterns the system controller software can be extended without the need for extensive modification of the existing code.

## Chapter 4. Empirical Modeling Methods

This chapter describes different methods which were used to build an empirical fuel cell cathode electrode degradation model. First, polynomial fitting is described, which is used to model fuel cell voltage and power, as well as cathode electrode voltage degradation. Next, a simplified vehicle model from literature is described and paired with an empirical fuel cell model based on fuel cell performance data collected in this study. The fuel cell voltage and power polynomials are used as a fuel cell model, and together with the vehicle model, make up a fuel cell vehicle model which can be used to convert vehicle speeds to fuel cell voltage. The conversion process and other aspects of drive cycles are discussed in the final section. The focus of these sections is on describing the methods behind the empirical model, while the implementation of some of these methods and the model itself are discussed in Chapter 5.

### 4.1. Polynomial Models

Polynomial models are among the simplest models, and usually easy to implement. In general, polynomials are of the form shown in Equation 15:

$$y(x) = a_n \times x^n + a_{n-1} \times x^{n-1} + \dots + a_1 \times x + a_0 \quad (15)$$

where  $n \in [1, d]$ , where  $d$  is the degree of the polynomial, the highest exponent of  $x$ , and  $a_n, a_{n-1}, \dots, a_1, a_0$  are constant coefficients determined by reducing the error given by a suitable objective function. One such objective function is the weighted sum of squares shown in Equation 16:

$$e^2 = \sum_{i=1}^K \left( \frac{y_i - \hat{y}(x_i)}{\sigma_i} \right)^2 \quad (16)$$

where  $K$  is the number of data points in the dataset,  $x_i$  and  $y_i$  are the  $x$  and  $y$  coordinates of the  $i^{th}$  data point, respectively,  $\hat{y}$  is the polynomial to be optimized, and  $\sigma_i$  is the error associated with the  $i^{th}$  data point [35].

In this study, polynomials for degrees  $d = 1$ ,  $d = 2$ , and  $d = 4$  are considered. A polynomial of degree 1 is the equation of a line given by Equation 17:

$$\hat{y}(t) = m \times t + b \quad (17)$$

where  $m$  is the slope of the line and  $b$  the intercept of the line with the vertical axis. A polynomial of degree 2 is the equation of a parabola curve given by Equation 18:

$$\hat{y}(t) = a_2 \times t^2 + a_1 \times t + a_0 \quad (18)$$

where  $a_0$ ,  $a_1$  and  $a_2$  are coefficients. Higher order polynomials are similar, with higher powers of  $t$  and more coefficients.

A polynomial of degree 2 was used to model fuel cell polarization curves, and a model of degree 4 to model current density vs. fuel cell power data. This is described in detail in Chapter 4.2.

Linear polynomials were used to model the degradation data discussed in Chapter 5. Other models were briefly explored (Appendix C), but abandoned since many studies in literature show that fuel cell degradation is approximately linear to 10 % voltage loss [15], [16], [26], which is considered end of life (EOL) by the US DOE [6]. By fitting the linear polynomial to the voltage degradation data, a voltage,  $\hat{y}$ , can be obtained at any point  $t$ , where  $t$  can be in units of stress cycles, or, by applying a conversion factor, in units of hours. The conversion factor can be obtained from the drive cycle, by counting the number of stress cycles within a given time interval. For example, if there are 10 cycles in 1 hour, the conversion factor is  $\frac{1}{10} \text{ hrs/cycle}$ .

## 4.2. Fuel Cell Vehicle Model

This section describes a vehicle model and a fuel cell model which can convert general drive cycles to vehicle power demand, and to a voltage response of any fuel cell, using vehicle and fuel cell stack specifications. The vehicle model was a simplified version of a model described by Ahmadi and Kjeang [29], which is a comprehensive dynamic model which includes factors such as aerodynamics, rolling resistance, road angle, regenerative braking, vehicle specifications, and engine performance. For this work, parameters such as road angle and regenerative braking were excluded, as was rolling resistance. Rolling resistance can have a significant impact on the power demand of the car, but varies heavily with road and tire conditions. Determining a suitable constant or

expression for the rolling resistance was beyond the scope of this work. Finally, it was assumed that all the vehicle power demand is supplied by the fuel cell stack.

Equations 19 to 26 were used to convert drive cycle data in the form of voltages  $\vec{V}$  and corresponding time in seconds  $\vec{t}$ , to fuel cell power demand  $\vec{P}_{cell,demand}$ . Arrows over a variable indicate vectors of values. First a vector of accelerations  $\vec{a}$  is calculated from the drive cycle data as shown in Equation 19.

$$\vec{a} = \frac{d\vec{V}}{d\vec{t}} = \left[ \frac{V_1 - V_0}{t_1 - t_0}, \dots, \frac{V_{i+1} - V_i}{t_{i+1} - t_i}, \dots, \frac{V_n - V_{n-1}}{t_n - t_{n-1}} \right] \quad (19)$$

The acceleration  $\vec{a}$  can then be used to calculate the power required to move the mass  $m_{car}$  of the vehicle using Equation 20.

$$\vec{P}_{weight} = m_{car} \vec{a} \vec{V} \quad (20)$$

From Equation 21, the power needed to overcome air drag resistance can be calculated, where  $\rho_{air}$  is the density of air,  $A_{front}$  is the frontal area of the car, and  $C_D$  is the drag coefficient of the car.

$$\vec{P}_{drag} = \frac{1}{2} \rho_{air} A_{front} C_D \vec{V}^3 \quad (21)$$

Adding  $\vec{P}_{weight}$  and  $\vec{P}_{drag}$  gives the total power necessary to move the vehicle according to the drive cycle. However, since some power is lost in the vehicles drive train, this total power must be divided by the efficiency of the drive train  $\eta_{drivetrain}$ . In addition, the accessories inside the car such as lights, radio etc. draw some power  $P_{aux}$ , which must be added to the overall power requirement. Finally, the total power must be divided by the fuel cell stack efficiency  $\eta_{stack}$ , to account for power lost inside the stack, mostly due to heat, which is a bi-product of the chemical reactions. The overall equation to calculate the stack power demand  $\vec{P}_{stack,demand}$  is shown in Equation 22.

$$\vec{P}_{stack,demand} = \frac{1}{\eta_{stack}} \left( \frac{\vec{P}_{weight} + \vec{P}_{drag}}{\eta_{drivetrain}} + P_{aux} \right) \quad (22)$$

The stack design can be specified by the number of cells  $N_{cells}$  it has and the area of each cell  $A_{cell}$ . From this specification,  $\vec{P}_{stack,demand}$  can be converted to the stack power density demand  $\vec{p}_{cell,demand}$ , which can be used to compare to stacks or cells of different specifications.

$$\vec{p}_{cell,demand} = \frac{\vec{P}_{FC,demand}}{N_{cells}} \times \frac{1}{A_{cell}} \quad (23)$$

With the vehicle model defined by the above equations the fuel cell power demand can be calculated. To find the fuel cell voltage which corresponds to a calculated power demand, a fuel cell model is required. The BOL fuel cell polarization curves measured in this work can serve as an empirical fuel cell model. From the cell voltage measured  $V_{cell}$  at different current densities  $i_{cell}$ , the cell power density  $p_{cell,out}$  can be calculated at each current density using Equation 24.

$$p_{cell,out} = V_{cell} \times i_{cell} \quad (24)$$

The average measured BOL polarization curve and the corresponding cell power curve are shown in Figure 25. The current density vs. calculated cell power data,  $i_{cell}$  vs.  $p_{cell,out}$  was fitted with a polynomial of degree 2 shown in Equation 25. This polynomial can be used to calculate the current density which corresponds to a given power demand. The average polarization curve data,  $V_{cell}$  vs.  $i_{cell}$ , was fitted with a polynomial of degree 4 shown in Equation 26. From this polynomial, the voltage at any current density can be found. Therefore, the given power demand obtained from the vehicle model can be converted to current density using Equation 25, and the current density can be converted to voltage with Equation 26.

$$i_{cell,emp}(p) = 1.197p^2 + 0.894p + 0.010 \quad (25)$$

$$V_{cell,emp}(i) = 0.84i^4 - 2.31i^3 + 2.10i^2 - 0.97i + 0.94 \quad (26)$$

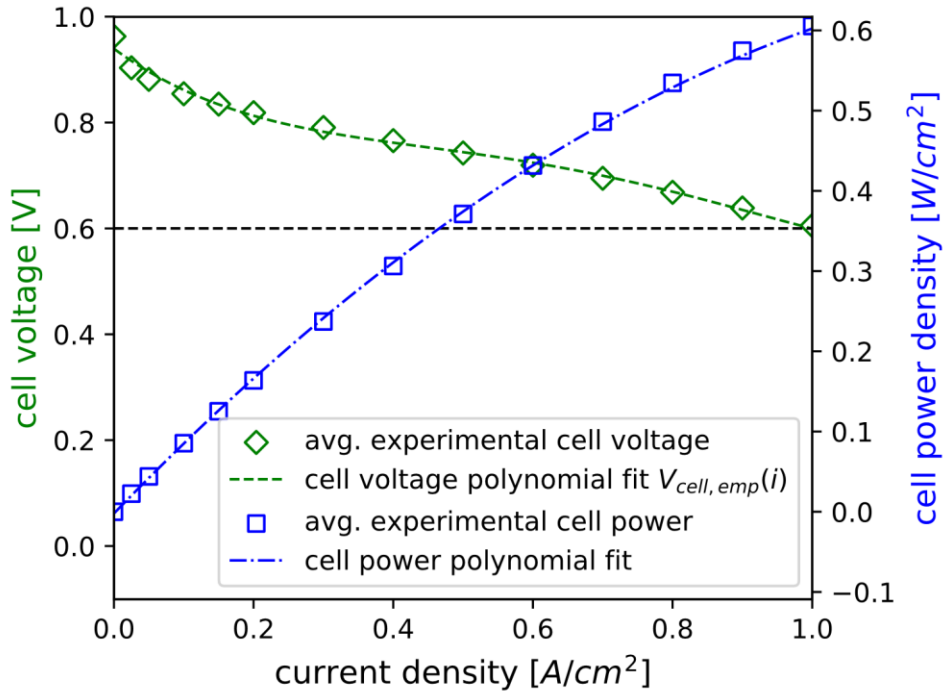
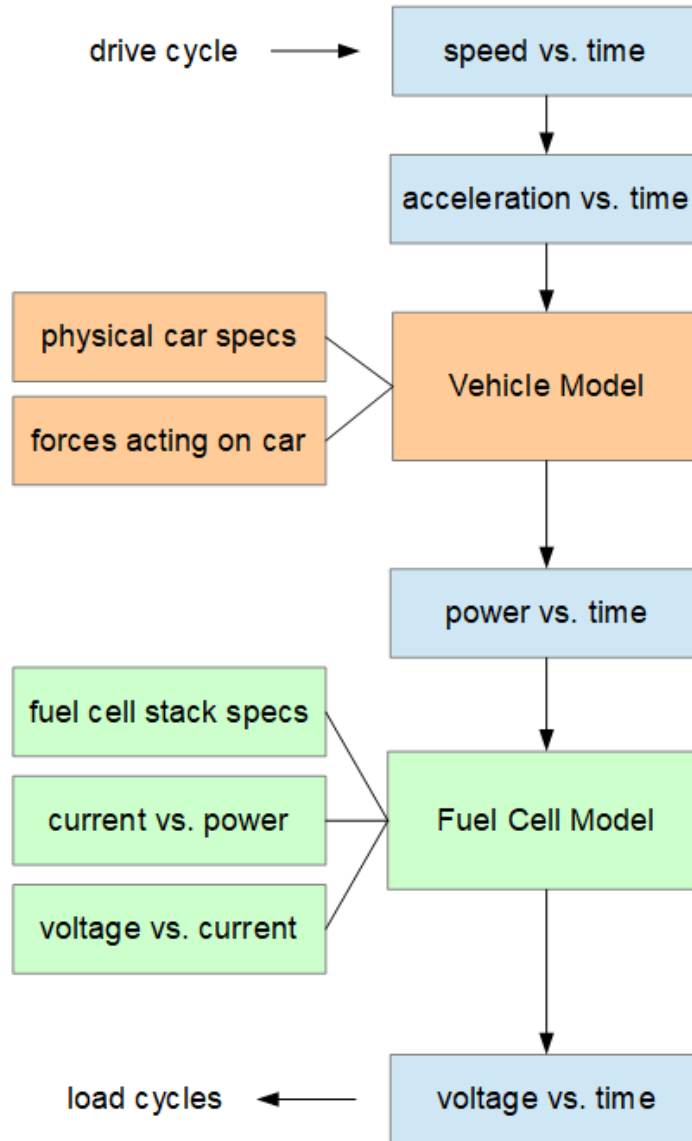


Figure 25: Empirical Fuel Cell Model Voltage and Power Data

### 4.3. Drive Cycles

The aim of this work was to empirically model cathode electrode voltage loss. As discussed in Chapter 1.3.1, the two causes for cathode electrode degradation considered in this study are: fuel cell load cycles due to changes in vehicle speed; and start/stop cycles which occur when turning the fuel cell car on or off. The drive cycles, which can be used to simulate fuel cell voltage loss due to vehicle usage, are composed of periods of load cycles with interspersed start/stop cycles. Any number of start/stop cycles can be assumed and directly used as an input in the empirical model. For example, if the drive cycle models a trip to work which takes 20 minutes, a start/stop cycle should occur for every 20-minute interval.



**Figure 26: Conversion Methodology**

The load cycles can be calculated from changes in vehicle speed. Data for vehicle speed is available from the US DOE in the form of vehicle velocity vs. time data, as discussed in Chapter 1.3.1. This velocity vs. time data can be converted to a corresponding fuel cell voltage profile using the fuel cell vehicle model discussed in Chapter 4.2. Figure 26 summarizes the conversion methodology between changes in vehicle speed and fuel cell voltage. The main parameters used in the vehicle model are shown in Table 7. Parameters such as weight and frontal area were taken from the specifications of the 2014 Toyota Mirai JPD10 fuel cell car [36], the drive train efficiency (composed of motor, battery, and inverter efficiencies) approximated with data from

Sulaiman et al. [37] while the remaining parameters were taken from Ahmadi and Kjeang [29].

**Table 7: Vehicle Model Parameters** [36], [29]

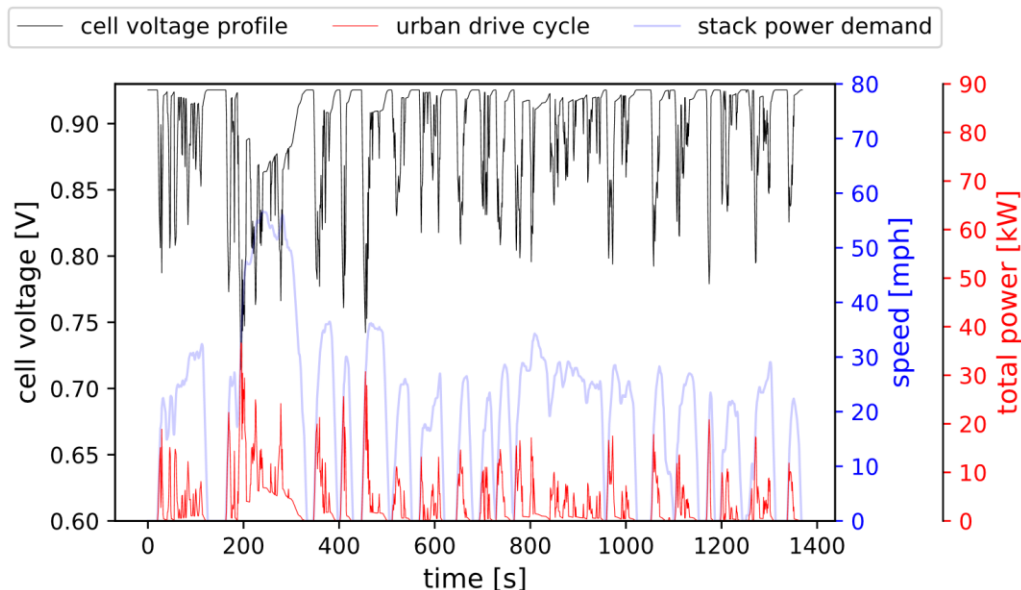
Weight [kg]	Frontal Area [m <sup>2</sup> ]	Drive Train Efficiency	Accessory Power [W]	Air Density [kg/m <sup>3</sup> ]	Drag Coefficient
1850	2.7	70%	750	1.2	0.26

Second, the power requirement from the vehicle model must be converted into the fuel cell power demand, using a suitable fuel cell stack configuration, fuel cell efficiency, and power-train model. In this study, it is assumed that the fuel cell is responsible for all the power demand. Table 8 shows the fuel cell stack configuration approximating that of the Toyota Mirai [36]. The fuel cell efficiency is the 2015 status as stated by the US DOE [6].

**Table 8: Fuel Cell Stack Configuration** [36], [6]

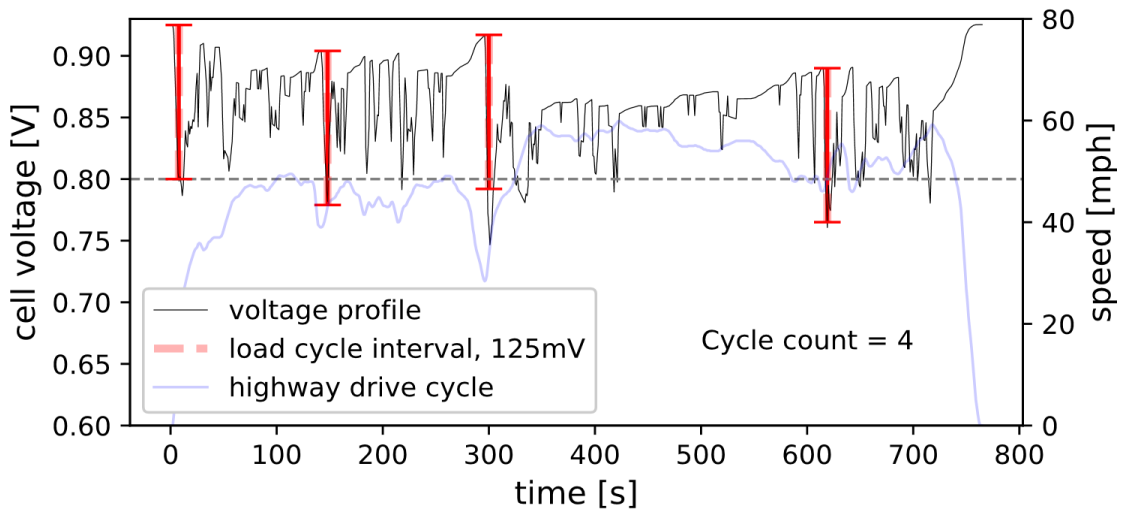
Number of Cells	Area per Cell [cm <sup>2</sup> ]	Efficiency
370	513	60%

Figure 27 shows the US urban drive cycle, the power calculated with the vehicle model and the stack configuration, as well as the voltage profile corresponding to the fuel cell model. The same calculations were also performed for the US highway drive cycle.



**Figure 27: US Urban Drive Cycle Converted to Power and Voltage**

The next objective was to estimate a suitable number of load cycles from each drive cycle. According to Figure 27, cycles of different depths exist, so it must be determined which cycle depth is to be considered as a full load cycle. From the analysis in Section 5.2 it was found that cycles between OCV and LPLs of 0.6 V, 0.7 V, and 0.8 V all result in the same level of degradation. Therefore, OCV (~0.925 V) to 0.8 V was chosen as the minimum load cycle to be considered, which corresponds to a depth of 125 mV. Figure 28 shows the voltage profile for the US highway drive cycle, with depth thresholds applied. Four cycles with depths of 125 mV or greater were found. Similarly, Figure 29 shows the voltage profile for the US urban drive cycle, for which 12 load cycles were found.



**Figure 28: Counting Load Cycles in US Highway Drive Cycle**

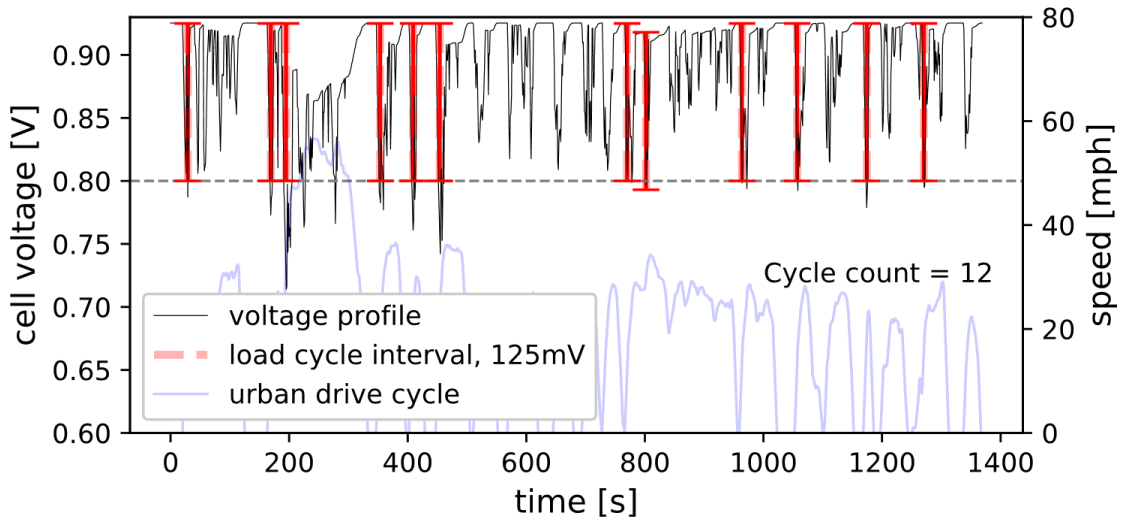


**Figure 29: Counting Load Cycles in US Urban Drive Cycle**

Choosing slightly different voltage depths results in different numbers of load cycles, which will change the outcome of the prediction for a given drive cycle. Different numbers of load cycles were chosen and the resulting change in predictions evaluated. The same was done with start/stop cycles, and the chosen numbers are shown in Table 9. The medium (or med) numbers obtained with the Mirai stack configuration, and the 125 mV cycle depths assumption, were varied to change the voltage profile. Larger stacks need smaller voltage cycles to produce the same power as smaller stacks, which means that fewer load cycles are counted for larger stacks. The resulting high, and low numbers for load and start/stop cycles were chosen to obtain upper and lower values for predictions. Also shown is the bus drive cycle used by [16], with 56 load cycles and 0.5 start/stop cycle per hour. The start/stop cycles are fractions, which means that it takes longer than the given drive cycle duration before one cycle is performed. Table 9 and Figure 30 also show predictions for hours of operation until 10% of the fuel cell voltage is lost, as well as the averages and standard deviations of the predictions. The standard deviations were applied to predictions shown in Section 5.4.

**Table 9: Drive cycle details with high, medium, and low cycle variations**

Drive Cycle	Load cycles (high/med/low)	Start-up/shut-down cycles (high/med/low)	Duration $t_{dc}$ [s/min]	Prediction to 10% voltage loss (high/med/low) [h]	Prediction Average/Std. Dev. [h]
Urban	16/12/8	0.35/0.25/0.15	1352/22.5	1300/1700/2600	1866/544
Highway	5/4/3	0.35/0.25/0.15	754/12.6	1900/2400/3300	2533/579
Bus	56	0.5	3600/60	1100	-

The number of cycles  $c_{dc}$  and the duration  $t_{dc}$  of a given drive cycle can be used to calculate the total number of cycles  $c_{tot}$  for a projected duration  $t_p$ , using Equation 27. The total number of cycles  $c_{tot}$  is then used to obtain the amount of degradation from the model.

$$c_{tot} = c_{dc} \times (t_p / t_{dc}) \quad (27)$$

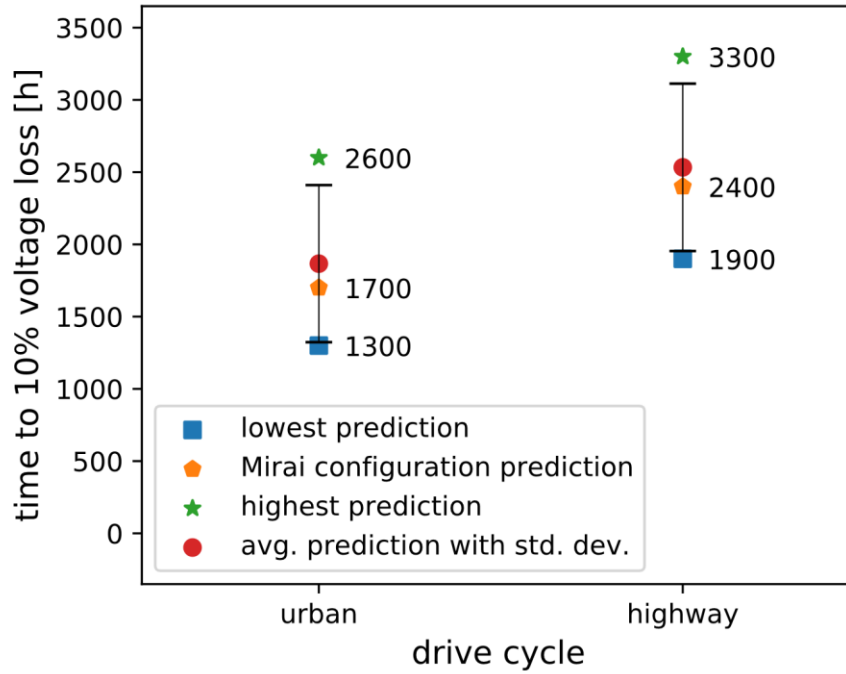


**Figure 30: Sensitivity of different model configurations**

## Chapter 5. Results and Discussion

The following sections discuss the results obtained using the methods described in the previous chapters. First, baseline experiments were conducted to ensure repeatability and to determine the variance between fuel cells. Second, a set fuel cells were degraded using different voltage limits to simulate different types of load cycles. Third, a second set of fuel cells were degraded with start/stop cycles. Finally, the data was combined into a degradation model to predict the performance loss (voltage degradation) and lifetime of fuel cells under different drive cycles.

### 5.1. Baseline

All fuel cells used in this analysis were manufactured and assembled in the same way (Chapter 2), and experimental procedures were kept constant (Chapter 3). Nevertheless, due to the inherent complexity of fuel cell manufacturing, assembly, and operation, the performance of the fuel cell specimens is subject to some variance. Therefore, the first objective for this work was to characterize the variance in the beginning of life (BOL) performance of the fuel cells used. Table 10 summarizes the set of fuel cell specimens. 10 BOL samples were analyzed and subjected to degradation testing (6 for load cycling and 3 for start-up/shut-down). At this point it should be noted that the total number of fuel cell specimens tested during this work was much larger. More than 40 fuel cells were tested before fuel cell manufacturing and assembly procedures were optimized, and experimental design was completed. The analysis that follows in this and later sections only pertains to the samples shown in Table 10, which were tested under fully optimized circumstances.

**Table 10: Fuel Cell Specimens Summary**

Number of BOL Samples	Number of degraded samples	Average platinum loading (CA/AN) [mg/cm <sup>2</sup> ]	Std. div. of platinum loading (CA/AN) [mg/cm <sup>2</sup> ]
10	10	0.60/0.55	0.06/0.06

Figure 31 shows the average fuel cell performance and standard deviation at different current densities. The performance variance is less than 6 mV up to 0.6 A/cm<sup>2</sup>, but doubles for 0.7 A/cm<sup>2</sup> and 0.8 A/cm<sup>2</sup> current densities. At current densities of 0.9 A/cm<sup>2</sup> and above, the variance ranges between 17 mV and 122 mV. This variance in

performance is mostly due to slight differences in the structure of the catalyst layers. The catalyst layer structure is largely affected by the size and distribution of particles in the catalyst ink, and the uniformity of ink deposition. The catalyst structure can have an especially large impact on water management inside the fuel cell, which can be seen in the large performance variance in the mass-transport region of Figure 31. Fuel cell assembly and test conditions were simpler to control and, therefore, have a smaller impact on the performance variance.

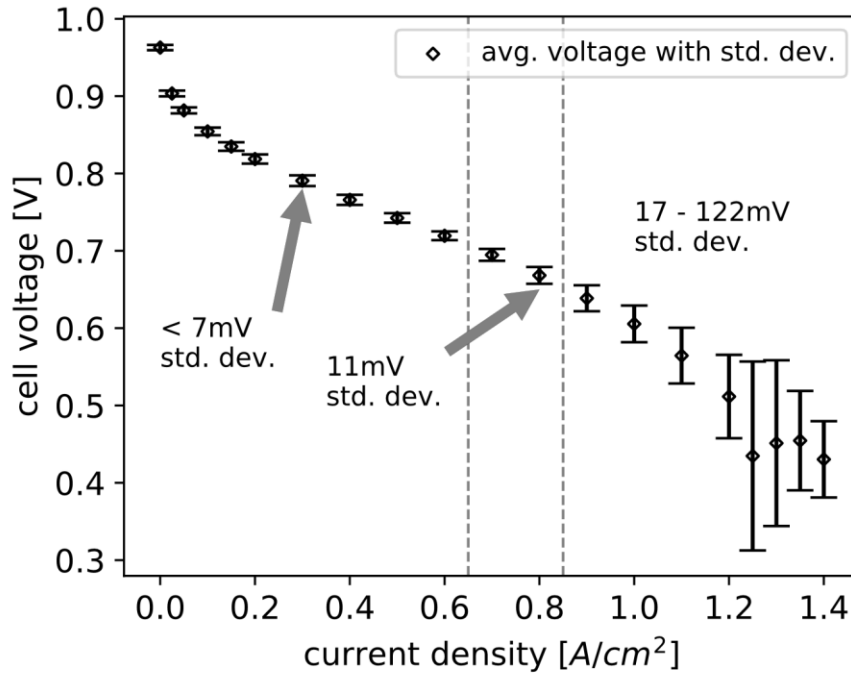


**Figure 31: Baseline BOL Polarizations with Variance**

Since the target performance degradation is 30 mV or less, tracking performance above 0.8 A/cm<sup>2</sup> is futile, due to the large variance in this region. On the other hand, any current density below 0.7 A/cm<sup>2</sup> will allow for tracking of changes in performance of less than 10 mV. At 0.7 and 0.8 A/cm<sup>2</sup> performance changes of less than 15 mV can still be distinguished. In addition, 0.8 A/cm<sup>2</sup> is the current density specified by the US DOE for tracking performance loss. Therefore, performance loss during degradation was tracked at current densities of 0.6, 0.7, and 0.8 A/cm<sup>2</sup>.

In addition to fuel cell performance loss measured under load, two additional diagnostics techniques were used to track degradation: cyclic voltammetry, to track

changes in ECSA, cross-over current, and double-layer capacitance, and electrochemical impedance spectroscopy to track changes in ohmic resistance.

Figure 32 shows the average cyclic voltammogram with standard deviations for the BOL fuel cell specimens. Again, the variance here is largely due to the catalyst layer structure. The overall range of standard deviations is relatively small, 0.8 mA to 3.3 mA. However, the ECSA is calculated using different parts of the curve, so that the different variances compound. The average ECSA, calculated from Figure 32, was 65 m<sup>2</sup>/g of platinum, with a standard deviation of 12 m<sup>2</sup>/g of platinum (Table 11). This shows that even though the variances in the cycle voltammograms are small, the standard deviation of the ECSA calculation is almost 19% of its mean value. However, the target ECSA loss of 40% of its initial area can still be distinguished, especially when monitoring the changes to a given MEA with known ECSA at BOL. The average fuel cell cross-over current  $i_x$  and double-layer capacitance  $C_{dl}$  were calculated to be 6.9 mA/cm<sup>2</sup> and 32 mF/cm<sup>2</sup> respectively, with standard deviations of 1.5 mA/cm<sup>2</sup> and 12 mF/cm<sup>2</sup>.

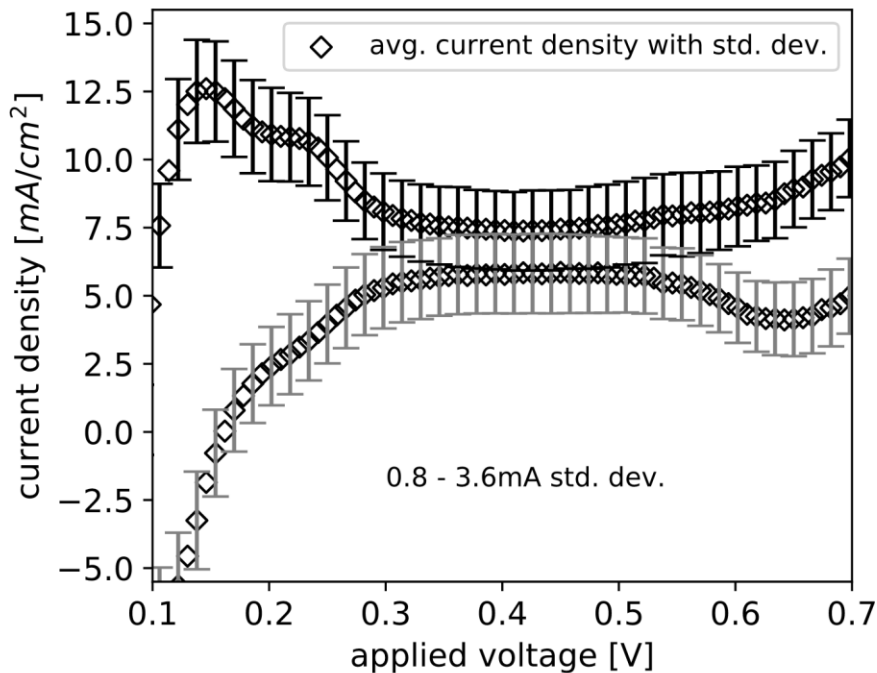


**Figure 32: Baseline BOL Cyclic Voltammograms**

Figure 33 shows the average Nyquist plot for the BOL fuel cell specimen. While many parameters can be obtained from this plot, only the ohmic fuel cell resistance is

used in this work. The average ohmic resistance R1 was found to be 10  $m\Omega$  with a standard deviation of 1.4  $m\Omega$  (Table 11).

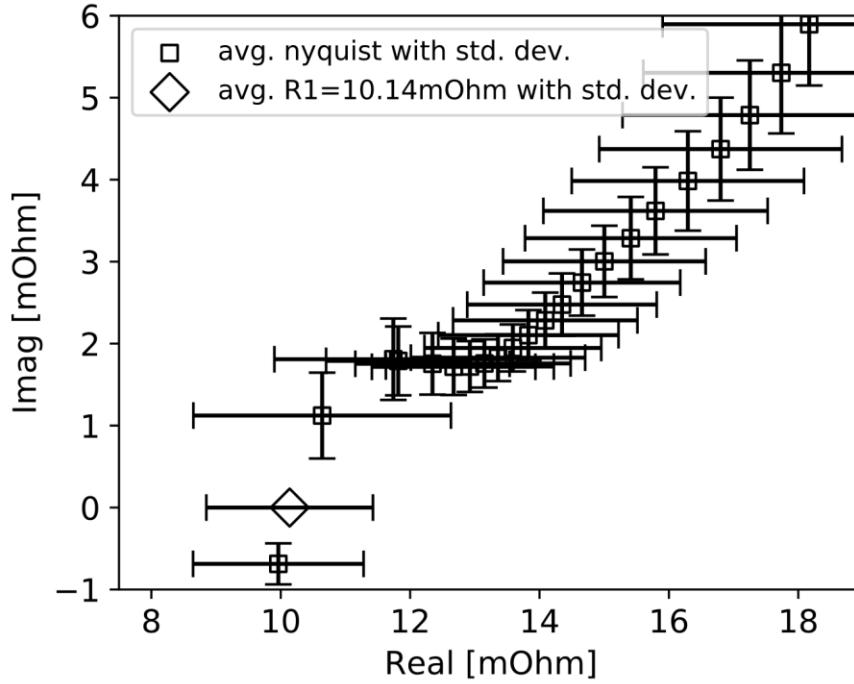


**Figure 33: Baseline BOL Nyquist Plots**

Table 11 summarizes the means and standard deviations for the ECSA,  $i_x$ ,  $C_{dl}$ , and R1 calculated from the CVs, and Nyquist plots, which were frequently measured to track degradation.

**Table 11: Electrochemical Measurements**

	ECSA [m <sup>2</sup> /g]	Crossover Current [mA/cm <sup>2</sup> ]	Double Layer Capacitance [mF/cm <sup>2</sup> ]	R1 [mOhm]
Mean	32	6.6	31	10
Std. Dev.	5.5	1.5	11	1.3

## 5.2. Degradation

After having ensured repeatable fuel cell performance and diagnostics, degradation experiments were carried out. Degradation data was obtained for load cycles and start-up/shut-down cycles according to the protocols discussed in Chapter 3, which are similar to those proposed by the US DOE. For the two protocols, the US DOE specifies voltage loss targets of 30 mV or less at 0.8 A/cm<sup>2</sup> after 30k load cycles and less than 5%

change in voltage at 1.2 A/cm<sup>2</sup> after 5k start-up/shut-down cycles. Table 12 summarizes the DOE voltage loss targets along with similar ECSA targets.

**Table 12: DOE Degradation Targets**

Test	Target # Cycles	Performance Target	ECSA Target
load cycling	30,000	<30mV @ 0.8A/cm <sup>2</sup>	<40% loss
start-up/shut-down	5,000	<5% change @ 1.2A/cm <sup>2</sup>	<20% change

The next two sections discuss the results obtained for load cycle, and start-up/shut-down degradation experiments.

### 5.2.1. Load Cycles

The first objective of this part of the study was to determine how the different lower potential limits, which occur during real load cycles, impact the degradation rate. The LPLs were selected to be 0.6, 0.7 and 0.8 V, others could be added if needed. For each LPL, two fuel cell specimens were degraded up to 30k load cycles. Figure 34 and Figure 35 show the fuel cell performance degradation for different LPLs at current densities of 0.8 A/cm<sup>2</sup> and 0.6 A/cm<sup>2</sup>. The cell voltages were adjusted to the same voltage at cycle 0. A large variance can be seen at most points for 0.8 A/cm<sup>2</sup>, as expected from the analysis in section 5.1. The variance is much smaller for 0.6 A/cm<sup>2</sup>. Nevertheless, a degradation trend can be seen in both cases. However, in the case of 0.8 A/cm<sup>2</sup>, no clear distinction can be made between the different LPLs (Figure 34).

The 0.6 A/cm<sup>2</sup> case (Figure 35) shows slower degradation for the LPL of 0.8 V, but a similar degradation rate for LPLs 0.7 and 0.6 V., except for LPL 0.8 V, which improved at 1k cycles, and was therefore lowered at 0 cycles. However, even after adjustment and lowering, the degradation rate with the LPL of 0.8 V remains slower than the other two. Figure 36 shows the ECSA loss during the load cycle test, and indicates slower degradation for LPLs 0.7 and 0.8 V. However, the error bars overlap with those from the LPL of 0.6 in almost all cases, so the result is not clear.

The results from Figure 35 and Figure 36 vaguely suggest that the degradation rate of the LPL of 0.6 V will be the highest, and that of 0.8 V the lowest. However, without fuel cell load demand field data, it is difficult to distinguish different LPLs from drive cycles, and the degradation rates, even if different, are similar. Therefore, the average

performance loss of all the results across the three different LPLs is used for model development.

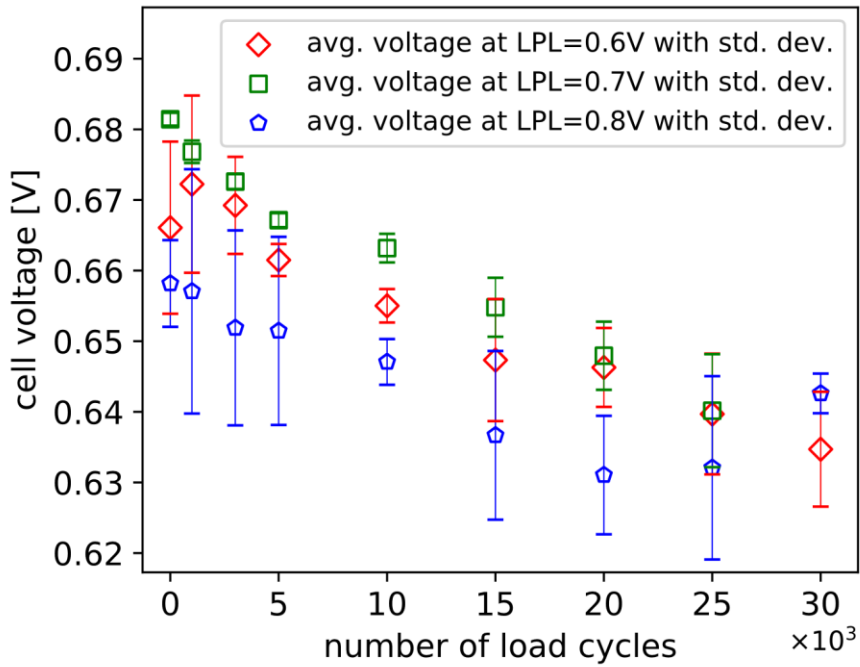


Figure 34: Performance at 0.8 A/cm<sup>2</sup> loss for different LPLs

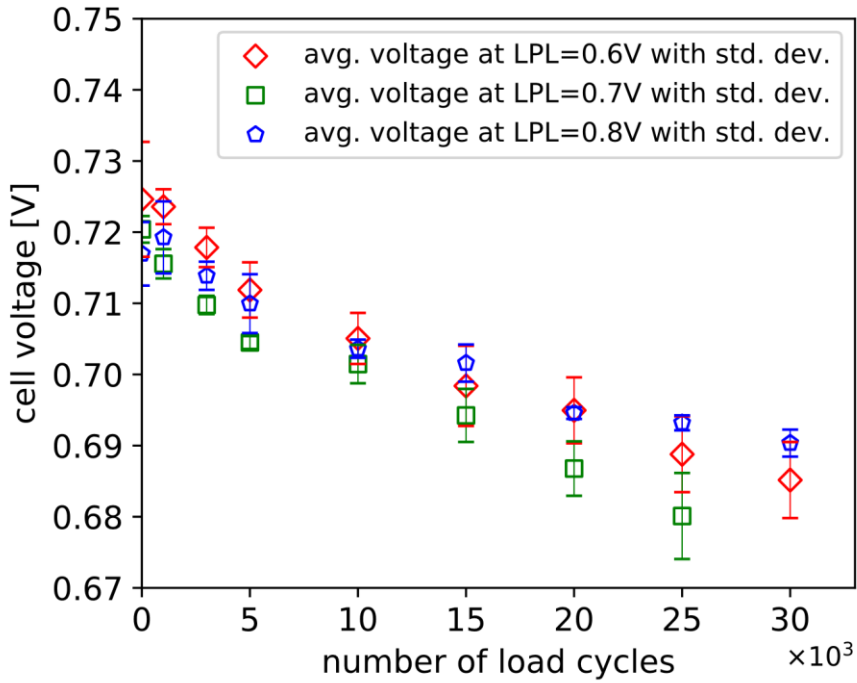
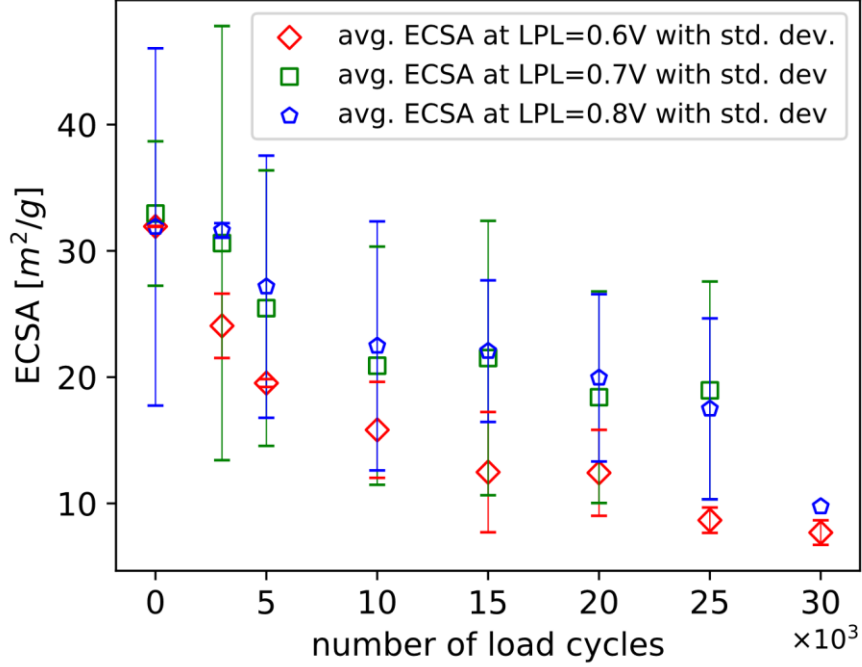


Figure 35: Performance at 0.6 A/cm<sup>2</sup> loss for different LPLs (Adjusted)



**Figure 36: ECSA loss for different LPLs**

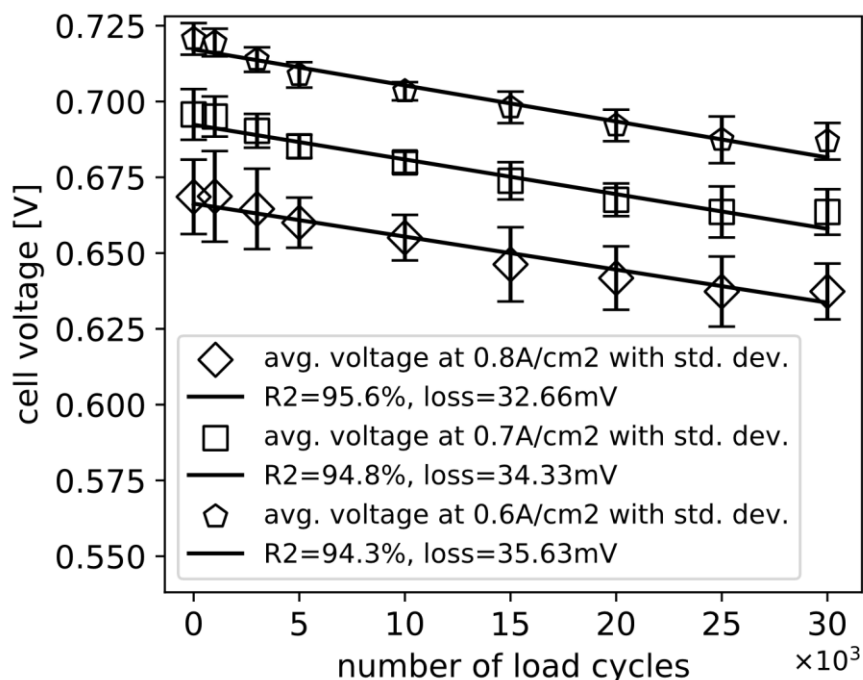
Figure 37 shows the fuel cell performance degradation at current densities 0.6, 0.7, and 0.8A/cm<sup>2</sup>, each modeled with a linear polynomial, as shown in Equations 28, 29, and 30, where  $x_L$  is the number of load cycles at which the performance should be predicted. Equation 30 was chosen since it was based on the data with the lowest standard deviation. It was used in Section 5.4 to predict fuel cell degradation due to load cycles.

$$V_{0.8}(x_L) = -1.09 \times 10^{-6} x_L + 0.666 \quad (28)$$

$$V_{0.7}(x_L) = -1.15 \times 10^{-6} x_L + 0.692 \quad (29)$$

$$V_{0.6}(x_L) = -1.19 \times 10^{-6} x_L + 0.717 \quad (30)$$

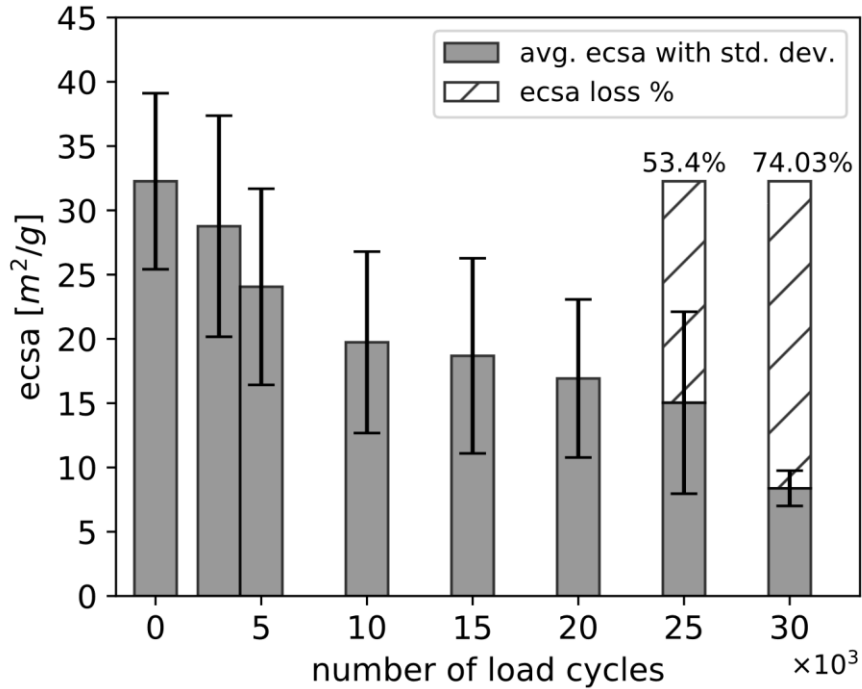
All three models show a voltage performance loss of 36 mV after 30k load cycles. Given the US DOE target performance loss of less than 30 mV after 30k load cycles, this result is off-target by 6 mV, which means 20% more voltage loss.



**Figure 37: Cell performance degradation**

Figure 38 shows the ECSA over 30k load cycles. The decline in ECSA is steady up to 10k load cycles, then flattens out until 25k. At 30k a sharp drop can be seen. The results suggest an ECSA loss of 74 % of its initial area after 30k cycles. This is a significantly larger loss of ECSA than the 40% or less ECSA loss target set by the US DOE (Table 12). However, it should be noted that less data was obtained for the 30k cycles data point, mainly due to disruptions in some of the long-term experiments. The data shown may be at the lower end of the error range (comparing to the error ranges of the previous cycles). Therefore, a loss of ECSA closer to 60% after 30k cycles is likely. As the cathode electrode degrades, the initial loss of ECSA is approximately linear, Shan et al. [38] showed a linear ECSA loss using a dynamic drive cycle, with 50% loss after 200 cycles. However, after nearly 50% of the ECSA has been lost, the degradation rate flattens. Platinum agglomeration is more rapid at the beginning, since platinum particle size is small at this stage. Once large agglomerates have been formed, the catalyst layer degradation rate can reduce [39]. Platinum dissolution continues, however, and degradation increases again.

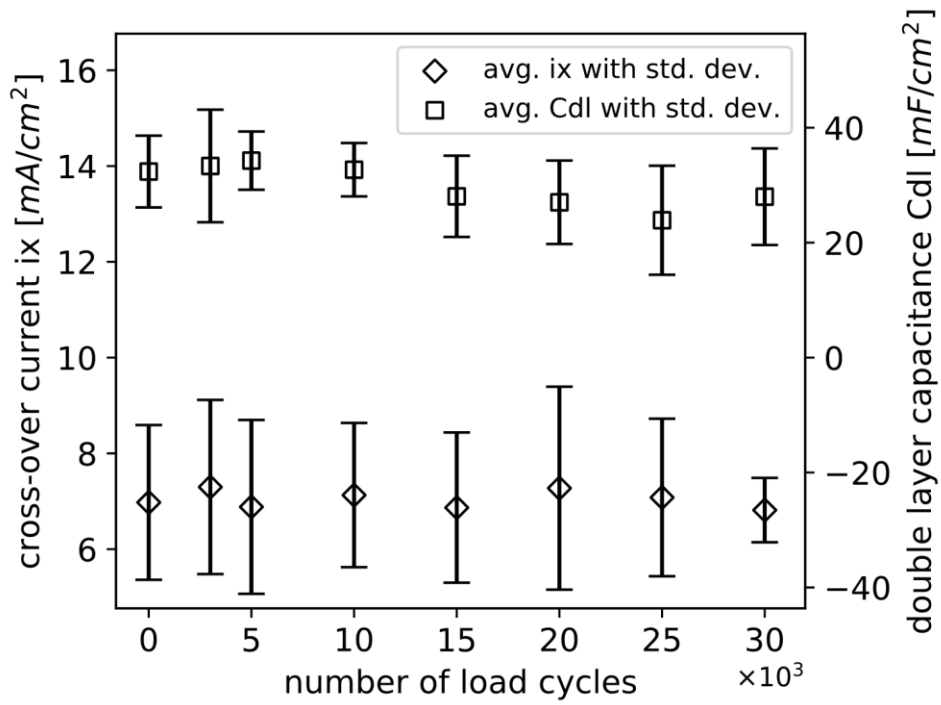
As shown in Figure 37, the performance is less steep, seemingly unaffected by the large initial loss in ECSA. This is because the impact of ECSA loss on performance is also related to the catalyst loading. A larger catalyst loading will compensate for ECSA loss.



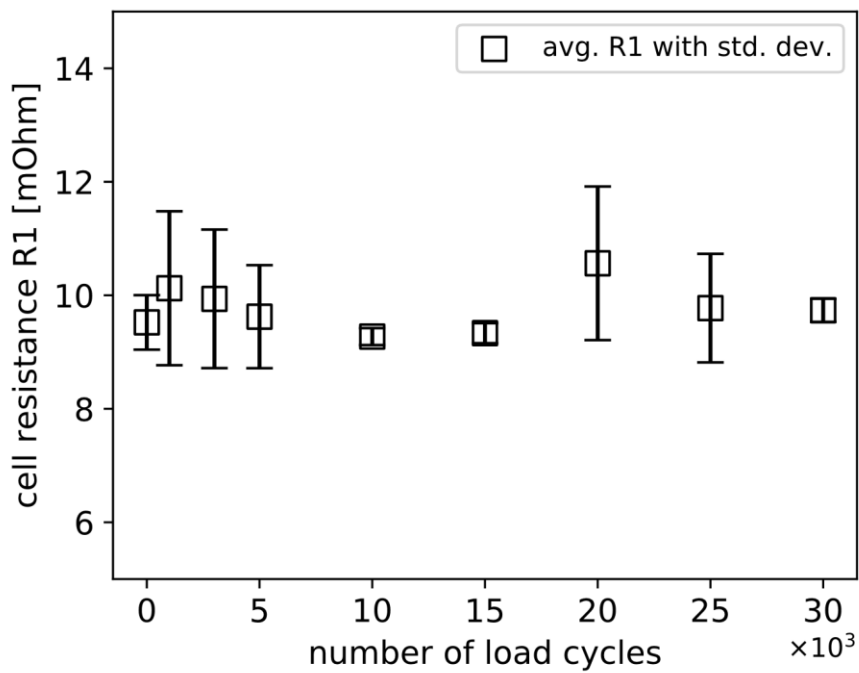
**Figure 38: ECSA Loss**

Figure 39 shows that the double layer capacitance  $C_{dl}$  and cross over current  $i_x$  remain approximately constant throughout the load cycle degradation test. This suggests that both membrane and carbon supports are not experiencing significant degradation. Similarly, the cell resistance (Figure 40), although noisy, remains approximately constant as well, indicating no major change in the electrical conductivity of the fuel cell components and component interfaces.

The heavy loss of ECSA, but with an absence of significant changes in  $i_x$ ,  $C_{dl}$ , or  $R_1$  is expected, since the stress test was designed to allow for controlled degradation of the cathode catalyst layer only, while limiting the degradation of other fuel cell components. The ECSA loss is due to platinum dissolution, re-deposition, and agglomeration. Carbon corrosion is associated with changes in  $C_{dl}$  [40], which are not seen here, which suggests little carbon corrosion is taking place during the load cycle degradation test.



**Figure 39: Double Layer Capacitance and Cross-Over Current Change**



**Figure 40: Cell Resistance Change**

## 5.2.2. Start-Up Shutdown Cycles

The second part of the degradation study focused on fuel cell degradation under start-up/shut-down cycles. Figure 41 shows the voltage loss of a fuel cell degraded with up to 5000 start-up/shut-down cycles, fitted linear polynomials as described in Section 4.1. The DOE target for the performance loss after 5000 start/stop cycles is less than 5% change from BOL at a current density of 1.2 A/cm<sup>2</sup> (Table 12). After 5000 cycles, the results in Figure 41 show a change in performance between 3% and 4% at current densities 0.6 A/cm<sup>2</sup> and 0.8 A/cm<sup>2</sup>, respectively. At 1.2 A/cm<sup>2</sup> a performance increase is suggested, however, the fit to the 1.2 A/cm<sup>2</sup> data has an accuracy of only 3%. As explained in Section 5.1, the error at high current densities such as 1.2 A/cm<sup>2</sup> is large, and therefore unreliable. Nonetheless, this result still suggests that the performance loss at 1.2 A/cm<sup>2</sup> is small. Equations 31, and 32, show the linear polynomial fits for the 0.6 A/cm<sup>2</sup> and 0.8 A/cm<sup>2</sup> data, where  $x_s$  is the number of start/stop cycles at which the performance should be predicted. Equation 32 was chosen to be consistent with the chosen load cycle model at the same current density (0.6 A/cm<sup>2</sup>). It was used in Section 5.4 to predict cathode electrode degradation due to start-up/shut-down cycles.

$$V_{0.8}(x_s) = -5.01 \times 10^{-6} x_s + 0.661 \quad (31)$$

$$V_{0.6}(x_s) = -6.80 \times 10^{-6} x_s + 0.716 \quad (32)$$

Figure 42 shows the ECSA loss up to 5k start/stop cycles. As was the case with the performance loss, the ECSA is reduced heavily after 5k cycles, and as much as 76 % was lost, 56 % more ECSA loss than the DOE target. Again, the impact of the heavy ECSA degradation on voltage loss is low. This suggests that a lower catalyst loading may show similar voltage loss, but less ECSA loss.

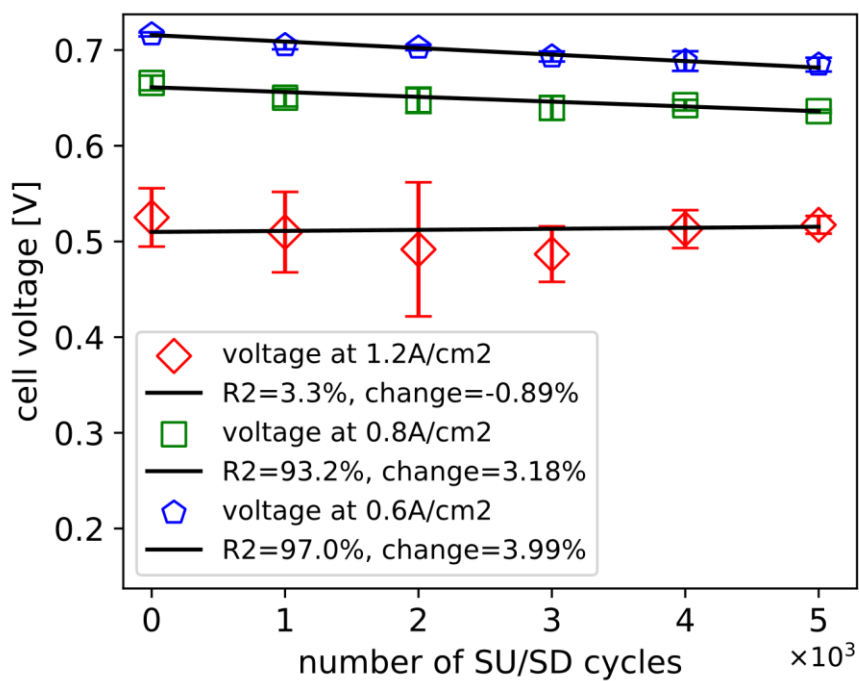


Figure 41: Performance degradation during SU/SD cycling

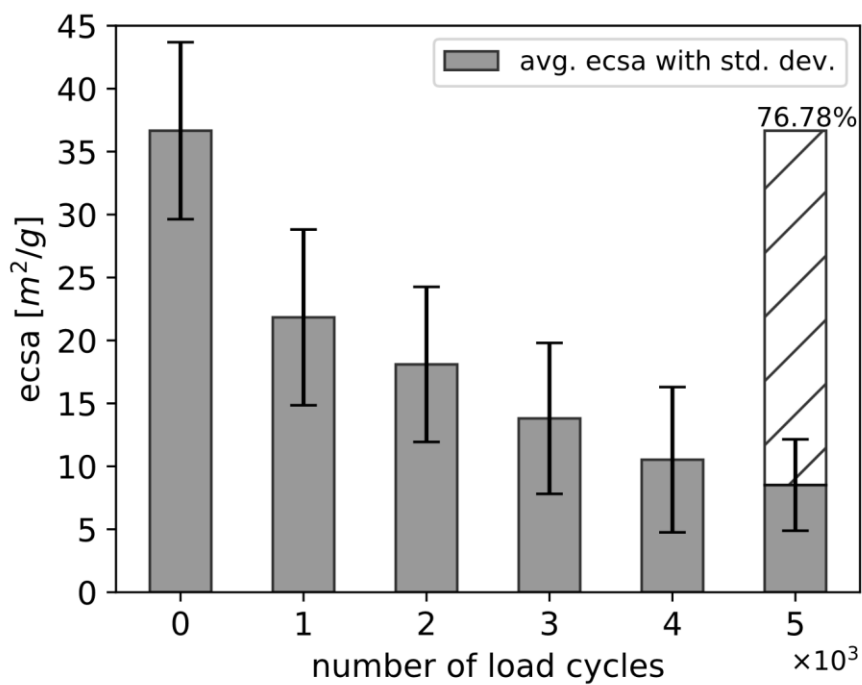
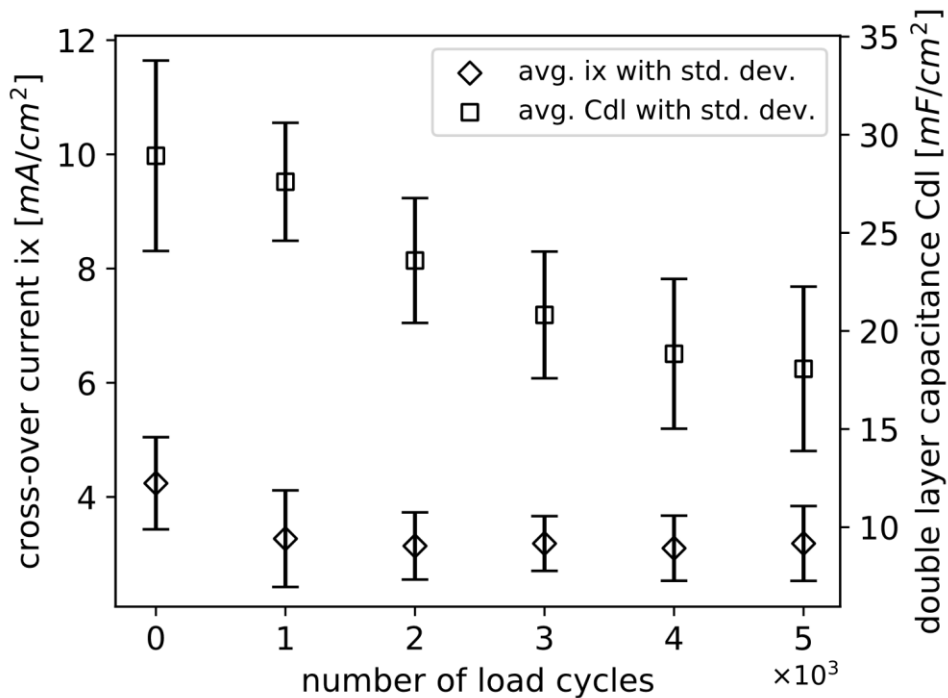
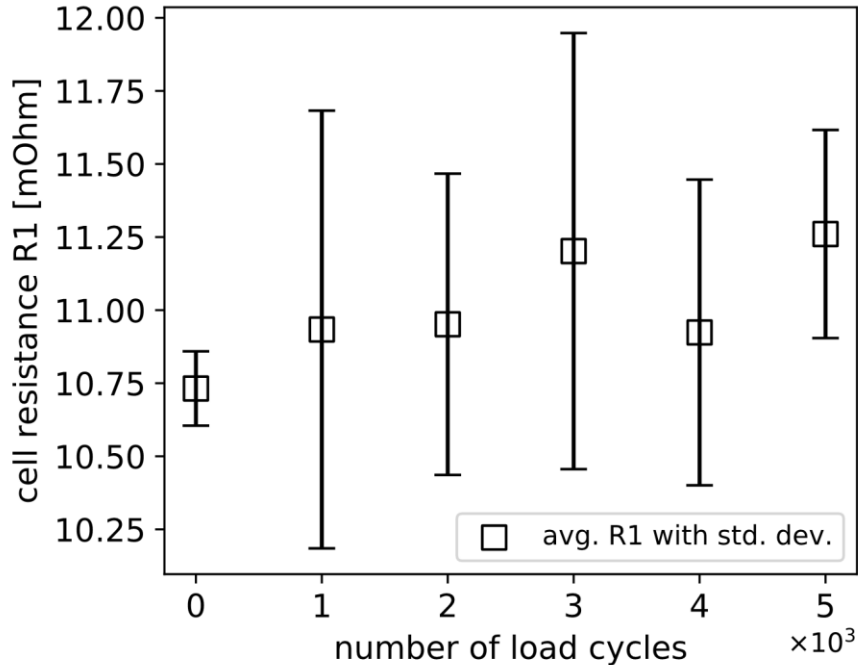


Figure 42: ECSA loss during SU/SD cycling

Figure 43 shows the cross-over current and double-layer capacitance change. The cross-over current change is insignificant, suggesting low membrane degradation. The double layer capacitance, on the other hand, decreases after 1k start/stop cycles, which was attributed to the reduction in platinum particles due to loss of carbon support during carbon corrosion by Part et al. [40]. However, they also saw an initial increase in double layer capacitance, which is not seen here. Figure 44 shows a change of less than 4% in ohmic resistance throughout start-up/shut-down degradation, suggesting that failure has not been reached. The ohmic resistance can increase due hollowing of the carbon support, and loss of ionomer [13]. Under failure conditions, however, the ohmic resistance may decrease drastically due to carbon support collapse [41], [13]. The small change in ohmic resistance, combined with the low voltage loss, may suggest that the changes that were made to the DOE protocol have reduced the severity of the stress test. The main change was the shortening of the start-up/shut-down steady state durations during each of the two parts of one cycle (start-up and shut-down). The DOE recommends active areas of 25 to 50 cm<sup>2</sup>, but 5 cm<sup>2</sup> were used in this study, hence it was assumed that less time is needed to achieve steady state, while causing the same amount of degradation.



**Figure 43: Crossover-current and double layer capacitance change**



**Figure 44: Resistance change**

### 5.3. Empirical Degradation Model

This section summarizes the empirical cathode electrode degradation model and explains how to use it. First, the limitations and assumptions of the model must be considered. The key limitation of the model is that it only applies to one type of fuel cell cathode electrode, with specifications as shown in Table 13. While this is a state of the art electrode used in most fuel cell vehicles, the effect of changing any of these specifications may significantly alter the electrode degradation.

**Table 13: Modeled Cathode Electrode Specification**

Catalyst	Loading	Support	Ionomer Loading	GDM
Platinum	0.5 mg/cm <sup>2</sup>	Carbon	30%	SGL 29BC

Furthermore, the model is subject to a number of different assumptions which further limit its applicability under certain conditions. The list of assumptions is shown below:

- Driving is done on flat roads only, and rolling resistance is neglected. The simplified vehicle model shown in this work does not support road angles or rolling resistance. However, changes in fuel cell power demand can be calculated with additional formulas, provided that data for road angles, road friction, and tire conditions is available.

- All of the vehicle power demand is supplied by the fuel cell. Modern fuel cell vehicles use lithium-ion battery packs to handle some of the power demand. This can potentially mitigate some of the degradation effects, but was beyond the scope of this study.
- No power is recovered through regenerative braking. Since no battery is used, power can also not be recovered.
- Factors which can mitigate degradation such as lower operating temperature or preventing OCV are not used. Such mitigation factors can reduce fuel cell degradation. The model assumes a temperature of 80 °C and that the fuel cell returns to OCV when no power is drawn.
- Coupling between load and start/stop cycle degradation is negligible. Even though preliminary data shown in this work suggests a significant coupling effect, more experimental work is required to characterize this effect and include it in the model.
- The difference between lab scale degradation tests and real conditions is small. The start/stop cycling experiments were designed to re-create real conditions, however, since testing was done on small scale fuel cells, differences may exist which can change the degradation rate.
- Load cycles with a depth of less than 125 mV do not contribute significantly to degradation. It was shown that load cycles with a depth of at least 125 mV do contribute to degradation, but it is unclear how much lower cycle depths contribute.
- The anode electrode contribution to the overall degradation is negligible. The cathode reaction is much slower, so cathode degradation has a larger impact on fuel cell voltage loss. However, a small portion of the voltage loss may be due to the anode, and it is unclear how small this portion is.

The model can be used to predict fuel cell voltage loss due to cathode electrode degradation after any number of hours of operation. To do this, a few inputs to the model must be specified:

- Vehicle speed vs. time drive cycle data. This data can be in the form of repeats of standard driving schedules. From this the total drive cycle duration  $t_{dc}$  can be calculated.
- The number of start/stop cycles  $x_s$ .
- Vehicle specifications: weight  $m_{car}$ , frontal area  $A_{front}$ , drag coefficient  $C_d$ .
- Fuel cell stack specifications: number of cells  $N_{cells}$ , area of each cell  $A_{cell}$ .
- The number of hours  $t_p$  at which voltage loss should be predicted.

If all of the above input parameters are supplied, the voltage loss due to cathode electrode degradation can be calculated using the methodologies described in Chapter 4 and the empirical degradation models for voltage loss due to start/stop cycles  $V_S$  and load cycles  $V_L$ . The final models that were chosen in Chapter 5.2 are reproduced here as Equation 33 for start/stop cycling, and Equation 34 for load cycling.

$$V_S(x_S) = -6.80 \times 10^{-6} x_S + 0.716 \quad (33)$$

$$V_L(x_L) = -1.19 \times 10^{-6} x_L + 0.717 \quad (34)$$

The steps to compute the overall fuel cell voltage loss due to start/stop and drive cycles are listed below:

1. Convert the speed vs. time drive cycle data to a corresponding voltage profile using the methodology described in Section 4.3.
2. Count the number of voltage drops which are at least 125 mV deep (see Section 4.3).
3. Calculate total number of load cycles  $x_L$  using Equation 27.
4. Compute the voltage loss due to start/stop cycles  $V_{loss,S}$ :

$$V_{loss,S} = V_S(0) - V_S(x_S)$$

5. Compute the voltage loss due to load cycles  $V_{loss,L}$ :

$$V_{loss,L} = V_L(0) - V_L(x_L)$$

6. Compute the total voltage loss  $V_{loss}$ :

$$V_{loss} = V_{loss,S} + V_{loss,L}$$

The voltage losses due to start/stop and load cycles may alternatively be converted to percentages with respect to each BOL voltage using Equation 35. This approach was used to find the number of hours to 10% voltage loss.

$$V_{loss,pct} = 100 \times \frac{V(0) - V(x)}{V(0)} \quad (35)$$

## 5.4. Lifetime Prediction

The voltage loss due to electrode degradation can be predicted under various fuel cell use conditions with the models and methodology described in Chapter 5.3. In this work, the purpose of lifetime predictions was to compare the voltage degradation results to similar results in literature and validate the empirical model for field operating conditions of fuel cell vehicles.

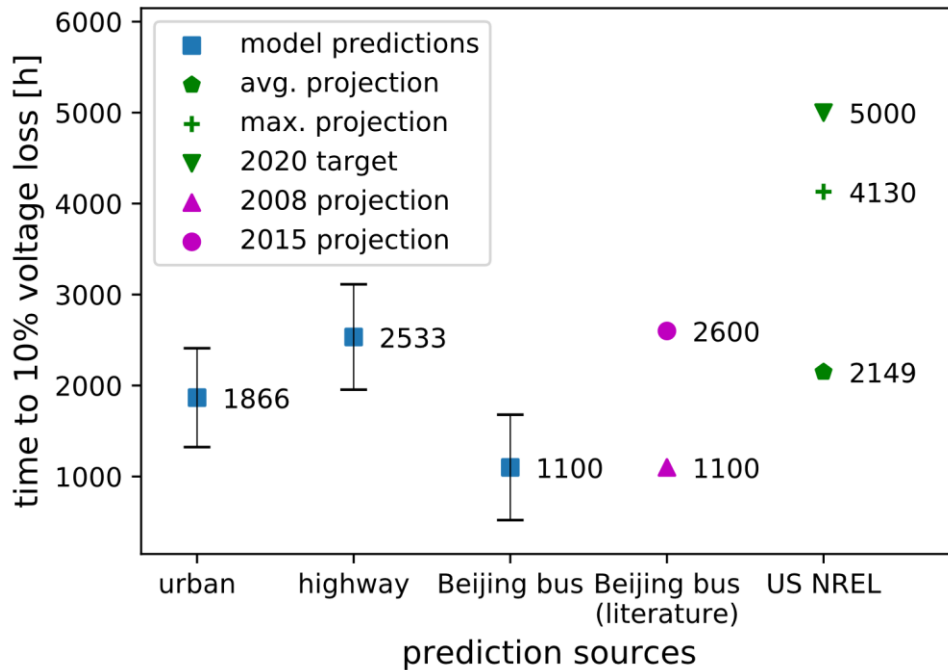


**Figure 45: Model predictions compared to literature predictions**

Predictions from the model for the two drive cycles (US urban and highway) are shown in comparison to projections from US DOE [28], and from a china bus project [16], [26].

Figure 45 shows model predictions to 10% voltage loss (blue squares, with errors bars explained in Chapter 4.3) for US urban and highway drive cycles, as well as predictions made by the US National Renewable Energy Laboratory (NREL), and Pucheng et al. [16], [26] (Beijing bus). The NREL projections are for average and maximum fleet durability, from different fuel cell vehicle projects. The DOE 2020 durability target is also shown. The Beijing bus projections are from 2008 [16], and 2015 [26] publications, from which drive cycle information was extracted (Table 9), and the model predictions for the Beijing bus drive cycle were made. The modeled bus predictions match the published 2008 data, but are below the 2015 data. Compared to the NREL predictions, both US highway and urban drive cycle predictions are similar to the average, but below

the maximum projections. Overall, the model gap between the projections and the 2020 target of 5000 hours is between 38 % (highest highway prediction) to 74 % (lowest urban prediction). The smallest literature gap is 17.4 % (maximum NREL projection), which is similar to the gap between current durability status and 2020 target shown in Figure 2, Section 1.1.1.

There are many possible reasons for the gap seen between the modeled results and the 2020 target, and modeled Beijing bus lifetime and the 2015 projection. First, the catalyst layer fabrication method used in this study, especially the mixing of the ink, may not result in sufficiently durable catalyst layers. This may be due to large agglomerates in a non-uniform ink, which could be helped by better dispersion methods. Second, the exact conditions, such as limiting voltages (LPL and UPL) are unknown in the case of the DOE data, and for the known case, the bus data from [16], the conditions were less severe (LPL = 0.7 V, UPL < OCV). Mitigating degradation due to high potentials at OCV can be achieved by ensuring that a minimum load is always applied to the stack, i.e. setting a UPL lower than OCV. Such mitigation is highly desirable, since OCV conditions also cause membrane degradation.

Since the data sets for start-up/shut-down degradation were obtained in separate experiments, an assumption for this analysis was that start-up/shut-down cycles do not significantly affect the degradation rate of load cycles and vice versa. It is possible that the degradation rates of the two conditions are coupled in some way, which could change the overall degradation. A preliminary investigation was therefore carried out to evaluate coupling effects between load cycles and start-up/shut-down cycles. For this preliminary experiment, diagnostics were performed every 3.5k cycles, composed of 3k load cycles (at 80 °C) followed by 500 start/stop cycles (at 35 °C). Figure 46 shows modeled voltage degradation trends due to start-up/shut-down (SU/SD) only, due to load cycles only, and due to combined cycles, along with the results from the preliminary combined experiment (red squares). This first preliminary dataset started by following the combined model until 17.5k cycles, after which it seemed to move over to follow the load cycles only model. The predicted 10% voltage loss occurred at around 35k combined cycles, however, the real data did not reach that point until 50k combined cycles. This result suggests that the model was underestimating the time to 10% voltage loss. Further analysis of these combined results was beyond the scope of this work, and more experiments are required to use the results to update the model. As the real combined results were obtained for one

configuration of load and start-up/shut-down cycles only, they cannot be applied to other drive cycles. Therefore, further experiments should be designed in a way that results can be used to model voltage degradation due to general drive cycles.

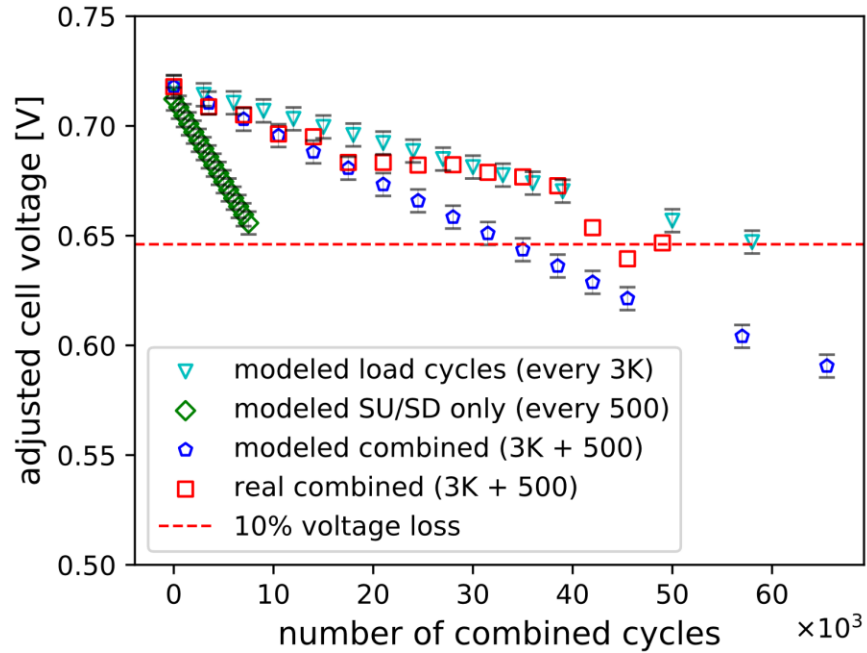


**Figure 46: Preliminary data for combined degradation**

Modeled voltage loss due to load cycles only, start-up/shut-down cycle only, and combined cycles are shown along with a preliminary dataset of real combined cycles. Error bars correspond to the standard error in modeling data. Protocol: 3k load cycles, followed by 500 start-up/shut-down cycles, repeat.

## Chapter 6. Conclusion

This thesis was carried out in an effort to contribute to the improvement of PEMFC durability, a barrier to the commercial success of fuel cell vehicles. Fuel cell durability is compromised by the degradation of the fuel cell components. The cathode electrode, one such component, was the focus of this work. The main objective was to build an empirical model of the voltage loss due to the degradation of the cathode electrode, and predict the voltage loss due to load cycle and start/stop drive cycle conditions for real-world operation of fuel cell vehicles. The first step to this model was to establish degradation test protocols and testing capabilities including fuel cell fabrication, diagnostics, and test automation. Procedures for catalyst ink synthesis and sonic spray coater operation were implemented and adapted, and sufficiently repeatable CCM manufacturing was achieved. Fuel cell assembly methods were developed that allowed controlled GDL compression, and leak-free assembly. Finally, the fuel cell test system was automated by developing several custom hardware and software solutions, which allowed for un-interrupted degradation testing to 30K cycles and more (8+ days), with any number of regular diagnostics intervals, including polarization curves, CV and EIS.

First, different lower potential limits of the load cycles were tested, to understand their effect on electrode degradation. It was concluded that even though some trends could be observed (mainly in the loss of ECSA), the effect of different limits on voltage degradation was negligible. Therefore, a single degradation test protocol, with a fixed LPL, is sufficient to simulate general load cycles.

The degradation data for load cycles and start/stop cycles was compared against DOE targets. For load cycles the voltage loss was 20% higher than the target, and for start/stop cycles, the voltage loss target was achieved. However, approximately 20% more ECSA loss was observed for load cycles, and 56% for start/stop cycles. The rate of ECSA loss fluctuated (large initial drop, flat region, further drop), however, the voltage degradation remained approximately linear. Degradation experiments using fuel cells with lower cathode catalyst loadings may be useful to understand at what point the ECSA loss starts affecting the voltage loss more heavily.

Using the experimental results, empirical models were developed for voltage degradation as a function of the numbers of load cycles and start/stop cycles. Linear

polynomial models were used, since different literature studies showed that fuel cell degradation is linear under real conditions.

With the linear models in place, drive cycle velocity data was converted to voltage profiles, to determine the corresponding number of load cycles. Similarly, assumptions were made to determine a suitable number of start/stop cycles for each drive cycle. The US urban and highway drive cycles were used, as well as a Beijing fuel cell bus drive cycle. The first two drive cycles were used to evaluate the sensitivity of determining load cycle numbers from voltage profiles, selecting start/stop intervals, and different stack configurations. A range of predictions was obtained, from which the standard deviation was calculated (max. +/- 575 hours) to be used as uncertainty intervals for further predictions.

Next, fuel cell vehicle operation to 10% voltage loss was predicted and compared to literature values. The US highway and urban drive cycle predictions were found to be within range of the average projection made by the US NREL (2149 hours of operation until 10% voltage loss). However, the predictions were below the NREL maximum projection and at least 38% below the 2020 US DOE durability target of 5000 hours. Similarly, the modeled Beijing bus voltage loss was also below the latest projection. Several reasons for lower durability were discussed. For load cycles, mitigation strategies (such as lowering idle voltage, limiting voltage cycle depth, or operating at below 80 °C) were neglected in the model. Including mitigation strategies in the load cycle part of the model can improve the predictions. The start/stop model did include mitigation by running at 35 °C instead of 80 °C. However, real start/stop temperatures could be even lower. Furthermore, preliminary results show that real combined load cycles and start/stop cycles have a degradation rate different from that predicted by the compounded models. To further improve predictions, investigation of the combined degradation effect is recommended.

Since the model was in range of comprehensive NREL average data, it can still be used to obtain an initial, conservative estimate of the fuel cell durability based on any available drive cycle. It may also be used to evaluate the effect of different voltage profiles (which depend on power train design), by changing load cycle counts and predicting the effect on vehicle lifetime.

## **6.1. Future Work**

This section first describes improvements to empirical degradation model which can be done by performing new experiments. This is followed by a description of a suggested use case for the model.

### **6.1.1. Model Improvements**

Throughout the process of manufacturing fuel cells, designing test protocols, implementing test procedures, and modeling results, many lessons were learned. The current method of fuel cell fabrication may be improved by using more sophisticated tools to synthesize catalyst ink, such as sonic stirring and/or microfluidizers. With the aid of these devices, a more uniform catalyst ink may be obtained, fuel cell performance may be improved, and degradation rates may be reduced. Additional characterization of the catalyst layers may help to fine-tune Pt loading, composition and thickness, possibly reducing flooding and degradation.

To improve the model predictions, the model should be extended to incorporate mitigation strategies and effects. Strategies include limiting the UPL and LPL, and reducing the operating temperature during start-up/shut-down cycles. For load cycles, the real fuel cell operating temperature may also be lower than 80 °C, which will reduce degradation reaction rates. It is recommended to upgrade the experimental setup to include a coolant loop, to be able to control conditions at lower temperatures, as well as reduce testing time by being able to heat/cool faster.

The coupling of load cycles and start-up/shut-down cycles should also be further investigated. The preliminary experiment was conducted by combining a specific number of load and start-up/shut-down cycles. However, this reduces the generality of the model, since only drive cycles with similar cycle configurations can be modeled accurately. Instead, experiments should be designed to determine a relationship between degradation and cycle configuration.

### 6.1.2. Model Use Case

The model assumptions and limitations discussed in Chapter 5.3 place a few restrictions on how the model can be used. However, the first three assumptions are a result of the simplified vehicle model used in this work. The vehicle model can easily be exchanged for a more comprehensive one, which can include hybridization, road angle, rolling resistance, and regenerative braking in the fuel cell power demand calculation. Furthermore, although the model only supports one specific electrode design, it is applicable to many fuel cell cars, since this design is similar to the industry standard. Other assumptions such as no mitigation, no coupling effects, etc. are likely to cause underestimation of fuel cell lifetime. Therefore, the model can be used to obtain conservative estimates of fuel cell voltage loss under start/stop and load cycle conditions.

To make the case for fuel cell vehicles, it is useful to show how fuel prices, government policies, engine emissions and different vehicle usage scenarios can impact the life cycle cost of using fuel cell vehicles. For example, fuel cell vehicles could become competitive in price to conventional cars, trucks or busses with the help of sufficient government subsidies for zero emission transportation. Tools such as the FCReL fleetLCA mentioned in Section 1.3.2 can be used to show how much government subsidy might be required, and by how much emissions could be reduced. Since life cycle cost is heavily influenced by the lifetime of the fuel cell stack, it is important to predict fuel cell degradation under different usage scenarios. As described in Section 1.3, the fuel cell membrane and the cathode electrode contribute the most to fuel cell degradation. Membrane durability was modeled by Macauley et al. [25], and the model described in this work can be used to provide conservative estimates of voltage loss due to cathode electrode degradation. With these two models, the fleetLCA and other tools can perform more accurate life cycle analysis, and deliver convincing data to show the benefits of using fuel cell vehicles.

## References

- [1] W. J. Ripple, C. Wolf, M. Galetti, T. M. Newsome, M. Alamgir, E. Crist, M. I. Mahmoud, and W. F. Laurance, "World Scientists' Warning to Humanity: A Second Notice," *Bioscience*, vol. XX, no. X, pp. 1–9, 2017.
- [2] P. J. Landrigan, R. Fuller, N. J. R. Acosta, O. Adeyi, R. Arnold, N. N. Basu, A. B. Baldé, R. Bertollini, V. Fuster, M. Greenstone, A. Haines, D. Hanrahan, D. Hunter, M. Khare, A. Krupnick, B. Lanphear, B. Lohani, K. Martin, K. V Mathiasen, M. A. Mcteer, C. J. L. Murray, J. D. Ndahimananjara, F. Perera, J. Potočnik, A. S. Preker, J. Ramesh, J. Rockström, C. Salinas, L. D. Samson, K. Sandilya, P. D. Sly, K. R. Smith, and A. Steiner, "The Lancet Commissions The Lancet Commission on pollution and health," vol. 6736, no. 17, 2017.
- [3] M. M. Mench, *Fuel Cell Engines*. John Wiley & Sons, Inc., 2008.
- [4] K. Itaoka, A. Saito, and K. Sasaki, "ScienceDirect Public perception on hydrogen infrastructure in Japan : Influence of rollout of commercial fuel cell vehicles," *Int. J. Hydrogen Energy*, vol. 42, no. 11, pp. 7290–7296, 2016.
- [5] A. F. Ambrose, A. Q. Al-amin, R. Rasiah, R. Saidur, and N. Amin, "ScienceDirect Prospects for introducing hydrogen fuel cell vehicles in Malaysia," *Int. J. Hydrogen Energy*, vol. 42, no. 14, pp. 9125–9134, 2016.
- [6] U. DOE, "3.4 Fuel Cells," *FUEL CELL Technol. Off. MULTI-YEAR Res. Dev. Demonstr. PLAN*, pp. 1–58, 2016.
- [7] D. Section, "3.2 Hydrogen Delivery," pp. 1–29, 2015.
- [8] M. Arenz and A. Zana, "Fuel cell catalyst degradation: Identical location electron microscopy and related methods," *Nano Energy*, pp. 1–15, 2015.
- [9] B. H. Lim, E. H. Majlan, W. R. W. Daud, T. Husaini, and M. I. Rosli, "Effects of flow field design on water management and reactant distribution in PEMFC : a review," pp. 301–316, 2016.
- [10] T. Ous and C. Arcoumanis, "Degradation aspects of water formation and transport

- in Proton Exchange Membrane Fuel Cell: A review," *J. Power Sources*, vol. 240, pp. 558–582, 2013.
- [11] P. Urchaga, T. Kadyk, S. G. Rinaldo, A. O. Pistono, J. Hu, W. Lee, C. Richards, M. H. Eikerling, and C. A. Rice, "Catalyst Degradation in Fuel Cell Electrodes: Accelerated Stress Tests and Model-based Analysis," *Electrochim. Acta*, vol. 176, pp. 1500–1510, 2015.
- [12] S. Zhang, X. Z. Yuan, J. N. C. Hin, H. Wang, J. Wu, K. A. Friedrich, and M. Schulze, "A review of platinum-based catalyst layer degradation in proton exchange membrane fuel cells," *J. Power Sources*, vol. 194, no. 2, pp. 588–600, 2009.
- [13] L. Li, L. Hu, J. Li, and Z. Wei, "Enhanced stability of Pt nanoparticle electrocatalysts for fuel cells," vol. 8, no. 2, pp. 418–440, 2015.
- [14] S. Mezzavilla, S. Cherevko, C. Baldizzone, and E. Pizzutilo, "Experimental Methodologies to Understand Degradation of Nanostructured Electrocatalysts for PEM Fuel Cells : Advances and Opportunities," pp. 1524–1536, 2016.
- [15] T. Mittermeier, A. Weiß, H. Gerold, and H. A. Gasteiger, "PEM Fuel Cell Start-up / Shut-down Losses vs Temperature for Non-Graphitized and Graphitized Cathode Carbon Supports," vol. 164, no. 2, 2017.
- [16] P. P. Á, Q. Chang, and T. Tang, "A quick evaluating method for automotive fuel cell lifetime," vol. 33, pp. 3829–3836, 2008.
- [17] C. Takei, K. Kakinuma, K. Kawashima, and K. Tashiro, "Load cycle durability of a graphitized carbon black-supported platinum catalyst in polymer electrolyte fuel cell cathodes," *J. Power Sources*, vol. 324, pp. 729–737, 2016.
- [18] K. Artyushkova, P. Atanassov, M. Dutta, S. Wessel, and V. Colbow, "Structural correlations: Design levers for performance and durability of catalyst layers," *J. Power Sources*, vol. 284, pp. 631–641, 2015.
- [19] S. Joo, S. Kim, J. In, C. Woong, J. Lee, I. Song, N. Lee, K. Kim, and J. Park, "Lifetime prediction of a polymer electrolyte membrane fuel cell via an accelerated

- startup e shutdown cycle test,” *Int. J. Hydrogen Energy*, vol. 37, no. 12, pp. 9775–9781, 2012.
- [20] J. H. Shiau and H. Lin, “Analyzing Accelerated Degradation Data By Nonparametric Regression,” vol. 48, no. 2, pp. 149–158, 1999.
- [21] G. Tsotridis, A. Pilenga, G. De Marco, and T. Malkow, *EU Harmonised Test Protocols for PEMFC MEA Testing in Single Cell Configuration for Automotive Applications; JRC Science for Policy report*. 2015.
- [22] G. Napoli, M. Ferraro, F. Sergi, G. Brunaccini, and V. Antonucci, “Data driven models for a PEM fuel cell stack performance prediction,” vol. 8, no. 0, 2013.
- [23] S. F. Burlatsky, M. Gummalla, J. O. Neill, V. V Atrazhev, A. N. Varyukhin, D. V Dmitriev, and N. S. Erikhman, “A mathematical model for predicting the life of polymer electrolyte fuel cell membranes subjected to hydration cycling,” *J. Power Sources*, vol. 215, pp. 135–144, 2012.
- [24] W. Gong and Z. Cai, “Engineering Applications of Artificial Intelligence Parameter optimization of PEMFC model with improved multi-strategy adaptive differential evolution,” vol. 27, pp. 28–40, 2014.
- [25] N. Macauley, M. Watson, M. Lauritzen, S. Knights, G. G. Wang, and E. Kjeang, “Empirical membrane lifetime model for heavy duty fuel cell systems,” *J. Power Sources*, vol. 336, pp. 240–250, 2016.
- [26] H. Chen, P. Pei, and M. Song, “Lifetime prediction and the economic lifetime of proton exchange membrane fuel cells,” *Appl. Energy*, vol. 142, pp. 154–163, 2015.
- [27] X. Zhang, D. Yang, M. Luo, and Z. Dong, “ScienceDirect Load profile based empirical model for the lifetime prediction of an automotive PEM fuel cell,” *Int. J. Hydrogen Energy*, vol. 42, no. 16, pp. 11868–11878, 2017.
- [28] J. K. Pi, S. Sprik, and C. Ainscough, “Fuel Cell Electric Vehicle Evaluation,” 2017.
- [29] P. Ahmadi and E. Kjeang, “Realistic simulation of fuel economy and life cycle metrics for hydrogen fuel cell vehicles,” no. October 2016, pp. 714–727, 2017.

- [30] M. B. Sassin, Y. Garsany, B. D. Gould, and K. E. Swider-lyons, "Fabrication Method for Laboratory-Scale High-Performance Membrane Electrode Assemblies for Fuel Cells," 2017.
- [31] M. Breitwieser, M. Klingele, B. Britton, S. Holdcroft, R. Zengerle, and S. Thiele, "Electrochemistry Communications Improved Pt-utilization efficiency of low Pt-loading PEM fuel cell electrodes using direct membrane deposition," *Electrochem. commun.*, vol. 60, pp. 168–171, 2015.
- [32] W. Liu, L. Wan, J. Liu, and M. Zhao, "ScienceDirect Performance improvement of the open-cathode proton exchange membrane fuel cell by optimizing membrane electrode assemblies," *Int. J. Hydrogen Energy*, vol. 40, no. 22, pp. 7159–7167, 2015.
- [33] B. Britton and S. Holdcroft, "The Control and Effect of Pore Size Distribution in AEMFC Catalyst Layers," vol. 163, no. 5, pp. 353–358, 2016.
- [34] X. Yuan, S. Zhang, J. C. Sun, and H. Wang, "A review of accelerated conditioning for a polymer electrolyte membrane fuel cell," *J. Power Sources*, vol. 196, no. 22, pp. 9097–9106, 2011.
- [35] A. Zielesny, *From Curve Fitting to Machine Learning An Illustrative Guide to Scientific Data*. Springer, 2016.
- [36] M. Millikin, "Toyota FCV Mirai launches in LA; initial TFCS specs; \$57,500 or \$499 lease; leaning on Prius analogy," *Green Car Congress*, 2014. [Online]. Available: <http://www.greencarcongress.com/2014/11/20141118-mirai.html>.
- [37] N. Sulaiman, M. A. Hannan, A. Mohamed, E. H. Majlan, and W. R. Wan Daud, "A review on energy management system for fuel cell hybrid electric vehicle: Issues and challenges," *Renew. Sustain. Energy Rev.*, vol. 52, pp. 802–814, 2015.
- [38] J. Shan, R. Lin, S. Xia, and D. Liu, "ScienceDirect Local resolved investigation of PEMFC performance degradation mechanism during dynamic driving cycle," *Int. J. Hydrogen Energy*, vol. 41, no. 7, pp. 4239–4250, 2016.
- [39] L. Dubau, L. Castanheira, F. Maillard, O. Lottin, G. Maranzana, J. Dillet, J. Perrin,

E. Moukheiber, G. De Moor, C. Bas, L. Flandin, and N. Caqué, "A review of PEM fuel cell durability : materials degradation , local heterogeneities of aging and possible mitigation strategies," vol. 3, no. December, 2014.

- [40] J. H. Park, S. D. Yim, T. Kim, S. H. Park, Y. G. Yoon, G. G. Park, T. H. Yang, and E. D. Park, "Understanding the mechanism of membrane electrode assembly degradation by carbon corrosion by analyzing the microstructural changes in the cathode catalyst layers and polarization losses in proton exchange membrane fuel cell," *Electrochim. Acta*, vol. 83, pp. 294–304, 2012.
- [41] M. Shaneeth, S. Basu, and S. Aravamuthan, "PEM fuel cell cathode catalyst layer durability : An electrochemical spectroscopic investigation," *Chem. Eng. Sci.*, vol. 154, pp. 72–80, 2016.

# Appendix A.

## Datasets

**Table A1. Load cycle dataset**

<b>load_cycle</b>	<b>avg_voltage_4A_ _V</b>	<b>std_4A _V</b>	<b>avg_voltage_3p5A _V</b>	<b>std_3p5A _V</b>	<b>avg_voltage_3A_ _V</b>	<b>std_3A _V</b>
0	0.669	0.012	0.696	0.008	0.721	0.005
1000	0.669	0.015	0.695	0.007	0.719	0.005
3000	0.665	0.013	0.690	0.006	0.714	0.004
5000	0.660	0.008	0.685	0.004	0.709	0.004
10000	0.655	0.008	0.680	0.003	0.703	0.003
15000	0.646	0.012	0.674	0.006	0.698	0.005
20000	0.642	0.010	0.668	0.005	0.692	0.005
25000	0.637	0.012	0.664	0.008	0.687	0.008
30000	0.637	0.009	0.664	0.008	0.687	0.006

**Table A2. Start-up/shut-down cycle dataset**

<b>susd_cycle</b>	<b>avg_voltage_4A_ _V</b>	<b>std_4A _V</b>	<b>avg_voltage_3p5A _V</b>	<b>std_3p5A _V</b>	<b>avg_voltage_3A_ _V</b>	<b>std_3A_ _V</b>
0	0.534	0.034	0.669	0.008	0.717	0.001
1000	0.532	0.020	0.653	0.004	0.702	0.008
2000	0.497	0.072	0.643	0.013	0.695	0.010
3000	0.498	0.019	0.636	0.018	0.684	0.016
4000	0.524	0.004	0.640	0.006	0.683	0.007
5000	0.522	0.004	0.636	0.002	0.681	0.000

## Appendix B.

### Automation

**Table B1. BOM for valve automation**

<b>Name</b>	<b>Purpose</b>	<b>Part No.</b>	<b>Manufacturer/Supplier</b>
N-Ch MOSFET	Switches valves on/off.	IRF3708PBF-ND	Digikey
NPN Transistor	Controls valve switch.	2N3904FS-ND	Digikey
Diode	Prevents current fly back.	1N4004GOS-ND	Digikey
2K Resistor	Limits current to MOSFET gate.	CF14JT2K00CT-ND	Digikey
1K Resistor	Limits current to transistor.	1.0KQBK-ND	Digikey
Arduino UNO	Turns valves on/off through USB interface.	1050-1024-ND	Digikey
Power Supply	AC/DC Desktop adapter 24V 24W supply for valves.	62-1252-ND	Digikey
AC Cord	AC cord for power supply	T1166-NA-ND	Digikey
3-way-valve	Switch H2-to-exhaust, N2-to-cathode	0330 T 2,0 FKM VA, G1/4 PNVAK-8bar, 24V DC 8W	Bürkert
2-way-valve	Switch Air-to-anode	6013 A S/64 FKM BR, NPT 1/4 PMAx 174 PSI, 24V DC 8W	Bürkert

**Table B2. BOM for system automation components**

<b>Name</b>	<b>Purpose</b>	<b>Part No.</b>	<b>Manufacturer/Supplier</b>
Load	Provide fast acting load.	BK8500	Digikey
Emerald API	Emerald Data Exchange Interface (TCP/IP Comm) to control G20 station.	P16-597-01	Greenlight
Potentiostat API	Toolkit to control Interface5000E potentiostat.	eChemDC/eChemAC	Gamry

**Table B3. Main automation software**

<b>Name</b>	<b>Purpose</b>	<b>File</b>	<b>Developer</b>
FCReL Fuel Cell System Controller	Custom software to control all system components and provide GUI control.	SystemControllerApp.py (and additional files + libraries)	FCReL
C# Gamry control library	Custom compiled library containing functions to control Gamry Interface5000E potentiostat.	GamryLib.sln (and additional files)	FCReL
Arduino Firmware	Custom firmware providing serial communication interface to Arduino and control valve circuit.	ValveController.ino	FCReL

**Table B4. Programming frameworks and libraries**

<b>Name</b>	<b>Purpose</b>	<b>Developer</b>
Python 3.4	Main development environment for FCReL Fuel Cell System Controller	Python Software Foundation
PyQt5	Python binding for Qt5 GUI framework	Riverbank Computing Limited
Microsoft .NET Framework	Framework for developing Gamry control library.	Microsoft
dload.py	API file for BK8500 programmable load	B&K Precision (Don Peterson)

## Appendix C.

### Non-parametric Model & Scale Factor

#### Non-parametric Model

While polynomials are so called parametric models (defined by their parameters, or coefficients), another class of models are non-parametric models (defined directly by the underlying data). The non-parametric degradation model presented here is a locally weighted least squares with a Epanechnikov kernel smoother according to [20] and [19]. This model has been used by [19] to fit start-up/shutdown AST data.

Given time series degradation data, this model can be used to estimate the voltage at time  $t$  as per Equation (36). The time index  $t$  can be interchanged with the corresponding cycles number, since there is a direct conversion between cycles and time:  $t = \text{cycle duration} \times \text{cycle number}$ . The cycle duration is the time it took to complete one cycle (e.g. 6s, as common in this study).

$$\hat{y}_i(t) = \frac{1}{d_i} \sum_{j=1}^{d_i} \frac{\{h_{2,i}(t, \omega) - h_{1,i}(t, \omega)(t_{ij} - t)\} \kappa(t_{ij} - t, \omega) y_{ij}}{h_{2,i}(t, \omega) h_{0,i}(t, \omega) - h_{1,i}(t, \omega)^2} \quad (36)$$

where  $h_{q,i}$  is given by Equation (37), and the Epanechnikov kernel  $\kappa(u, \omega)$ , with bandwidth parameter  $\omega$  by Equation (38).

$$h_{q,i}(t, \omega) = \frac{1}{d_i} \sum_{j=1}^{d_i} (t_{ij} - t)^q \kappa(t_{ij} - t, \omega) \quad (37)$$

$$\kappa(u, \omega) = \begin{cases} \frac{3\sqrt{5}}{4} \left[ 1 - \frac{1}{5} \left( \frac{u}{\omega} \right)^2 \right] & \text{if } \left( \frac{u}{\omega} \right)^2 < 5 \\ 0 & \text{otherwise} \end{cases} \quad (38)$$

Table 14 shows descriptions of the symbols used in Equations (36), (37), and (38). The bandwidth parameter  $\omega$  can be used to balance the bias and variance at each point. In other words, it can be used to balance between over and under fitting the data. Suitable

values for  $\omega$  were determined experimentally (by observing the fitting result). This is sufficient for small, initial datasets, since a good fit can be early identified visually. However, for larger datasets (with more variance), more sophisticated, computational methods should be used.

**Table 14: Description of symbols used in degradation model.**

Parameter	Range	Units	Description
$\omega$	0 to $\infty$	-	Bandwidth parameter for kernel smoother.
$\kappa(u, \omega)$	-	-	Kernel function.
$\hat{y}_l$	0 to 1	V	Voltage estimate.
$i$	0 to $d_i$	-	Index of SL.
$j$	0 to $d_i$	-	Index of data point.
$m$	0 to $\infty$	-	Number of SLs.
$d_i$	0 to $\infty$	-	Number of data points for SL $i$ .
$y_{ij}$	0 to 1	V	Experimental voltage data point $j$ at SL $i$ .
$t_{ij}$	0 to $\infty$	h/cycle	Time (or cycle) corresponding to experimental voltage data point.
$t$	0 to $\infty$	h/cycle	Time (or cycle) corresponding to voltage estimate.

## Scale Factor

The scale factors can be used to interpolate between and beyond available data. Degradation data was obtained for discrete load cycles; however, real load cycles are continuous. For example, if data exists for LPLs of 0.6 and 0.7 V, but a load cycle input has a LPL of 0.65 V, the scale factor can be used to scale the 0.6 V LPL degradation data to a 0.65 V LPL, without having to first obtain a separate dataset for 0.65 V LPL.

The algorithm for obtaining the scale factors is summarized as follows:

1. Obtain  $\hat{\mu}_m$  by smoothing  $\{\bar{y}_{mk}, k = 1, \dots, d\}$  on  $\{t_{mk}, k = 1, \dots, d\}$

$$\text{where } \bar{y}_{mk} = \left( \frac{1}{n_m} \right) \sum_{j=1}^{n_m} y_{mjk}$$

2. Minimize Equation (39) for  $a \in [0,1]$  to determine a scale parameter  $a_i$  for each SL:

$$\min_{a_i} \left[ \sum_{j=1}^{n_i} \sum_{k=1}^{d_i} [y_{ijk} - \hat{\mu}_m(a_i \times t_i)]^2 \right] \quad (39)$$

3. Scale each SL time data points  $t_{ijk}$  to obtain a new dataset:

$$t'_{ijk} = \frac{a_i}{a_m} t_{ijk} ; \quad y'_{ijk} = y_{ijk}$$

4. Obtain a new  $\hat{\mu}_m$  by smoothing  $\{y'_{ik}, k, i = 1, \dots, m; k = 1, \dots, d\}$  on  $\{t'_{ik}, i = 1, \dots, m; k = 1, \dots, 3\}$ .

5. Repeat steps 2 to 4 until  $a_i$  converges.

## Model Comparison

At an earlier point in this study, the non-parametric model was compared to polynomial models. Two polynomial models, and two non-parametric models with different bandwidths were compared. Figure 47 shows all four models fitted to the same dataset. The quadratic polynomial ( $n = 2$ ), and the non-parametric model with  $\omega = 3 \times 10^3$  follow the shape of the data closely, while the other two, due to their linear nature, cannot follow the curvature of the data. This is also reflected in the model accuracies shown in Table 15.

**Table 15: Model accuracy**

	Polynomial d=1	Polynomial d=2	Non-parametric w=3e3	Non-parametric w=1e6
R <sup>2</sup>	83.6%	86.4%	87.2%	81.8%

However, even though their model accuracy is low, the linear polynomial ( $d = 1$ ) and the non-parametric model with  $\omega = 1 \times 10^6$  show better results for predicting values far past the available dataset. In fact, the other two models become un-usable, or even un-defined. This is shown in Figure 48, where the quadratic model can be seen to predict increasing voltage past the available data, and the non-parametric model with  $\omega = 3 \times 10^3$  becomes undefined. The remaining two models, however, predict linear performance loss over time. The non-parametric model predicts slightly higher voltages than the polynomial,

however, its complexity is much greater. Therefore, only the linear models are used in Chapter 5.4 to predict fuel cell voltage loss due to cathode electrode degradation due to stress cycles.

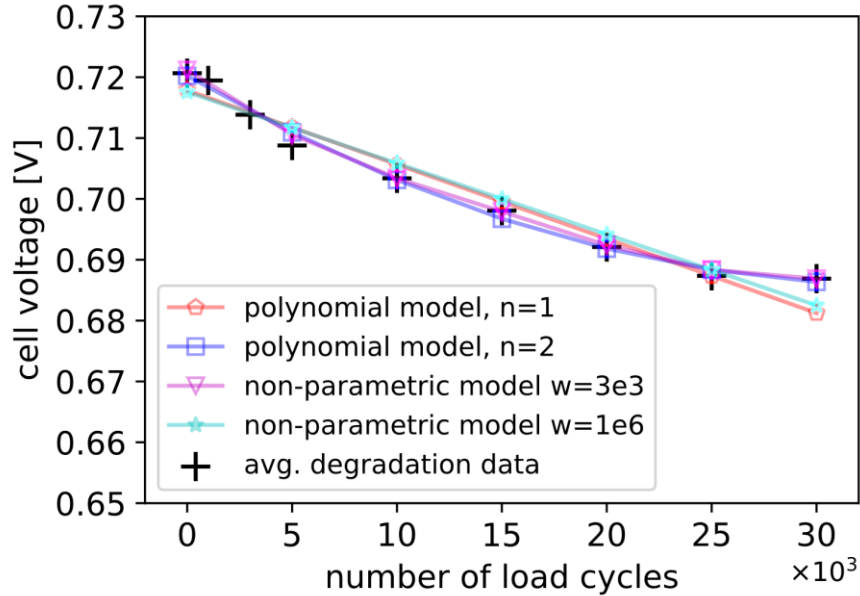


**Figure 47: Model fit comparison**

Fuel cell voltage loss is usually expressed in terms of hours to 10% loss. The fuel cell operating times stated in literature are usually less than 3000 hours [6]. The corresponding number of stress cycles depends on the drive cycle used. For example, the US urban drive cycle has 12 load cycles over 1352 seconds. The number of load cycles in 3000 hours can be found as follows:

$$\# \text{ load cycles} = \frac{3000 \text{ h} * 3600 \frac{\text{s}}{\text{h}}}{1352 \text{ s}} * 12 \text{ cycles} = 96 \times 10^3 \text{ cycles}$$

Therefore, it is useful to be able to extrapolate up to 96k cycles to compare to literature results. Furthermore, others have shown linear degradation for start/stop and load cycles [16]. However, for some models, linear degradation rates were assumed after only a few hundreds of cycles [26], [15].

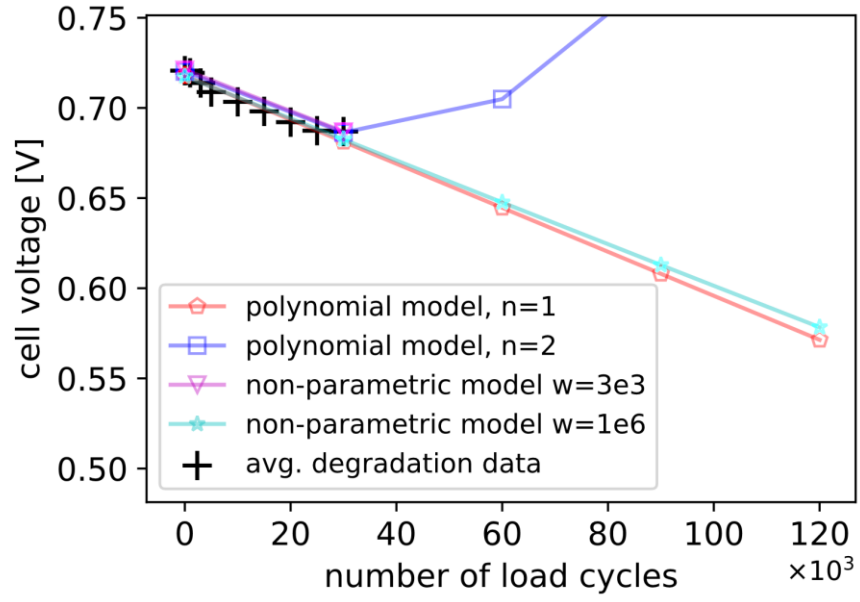


**Figure 48: Model prediction comparison**